The Dissertation Committee for Stephen Bruce Ferencz Certifies that this is the approved version of the following Dissertation:

SURFACE WATER-GROUNDWATER EXCHANGES UNDER CONDITIONS OF DAILY RIVER STAGE FLUCTUATIONS: IMPLICATIONS FOR FLUID, SOLUTE, AND HEAT DYNAMICS IN DAM REGULATED RIVER COORIDORS

Committee:

Bayani Cardenas, Supervisor

Bethany Neilson

Daniella Rempe

Philip Bennett

SURFACE WATER-GROUNDWATER EXCHANGES UNDER CONDITIONS OF DAILY RIVER STAGE FLUCTUATIONS: IMPLICATIONS FOR FLUID, SOLUTE, AND HEAT DYNAMICS IN DAM REGULATED RIVER COORIDORS

by

Stephen Bruce Ferencz

Dissertation

Presented to the Faculty of the Graduate School of

The University of Texas at Austin

in Partial Fulfillment

of the Requirements

for the Degree of

Doctor of Philosophy

The University of Texas at Austin

May 2020

Acknowledgements

While much of a dissertation is a solitary pursuit, I could not have finished it and maintained my happiness and sanity without the incredible support network of my fellow graduate students in the Jackson School and the broader Jackson School community of administrators, staff, and faculty. Many thanks to Philip Guerrero who helped me navigate the graduate school bureaucracy on numerous occasions, and also for caring about me as a person. I would like to thank my advisor Bayani Cardenas and my entire committee for their guidance and support, and granting me the freedom to pursue the research questions that interested me. Bayani has always advocated for my success, lent encouragement for my research questions, and given advice on how to improve my research. His mentorship has made me a better scientist and given me the tools and confidence to pursue my own research. I would also like to thank Bethany Neilson, a committee member and collaborator on many of my studies, for always giving such thoughtful feedback on my work. I am thankful for all of the friendships that I have formed over the past five years with many of my peers in the Jackson School. My friends made it fun to come to work every day, helped me get through the rough patches, and made life in Austin pretty fantastic. Finally, I would like to thank my parents who instilled in me from a young age a passion for learning and intellectual curiosity. Their unwavering support gave me the confidence that I could achieve success at whatever I pursued as long as I put in the work.

Abstract

SURFACE WATER-GROUNDWATER EXCHANGES UNDER CONDITIONS OF DAILY RIVER STAGE FLUCTUATIONS: IMPLICATIONS FOR FLUID, SOLUTE, AND HEAT DYNAMICS IN DAM REGULATED RIVER COORIDORS

Stephen Bruce Ferencz, PhD

The University of Texas at Austin, 2020

Supervisor: M. Bayani Cardenas

The damming of rivers has resulted in multitude of environmental impacts to river ecosystems. The focus of this dissertation is to assess how dams used for hydroelectric power generation influence surface water-groundwater exchange. The exchange of surface water with groundwater has been demonstrated to be an important mechanism regulating nutrient dynamics in rivers. Hydroelectric dams are often "hydropeaked," which is when discharge from the dam is increased/decreased in accordance with daily patterns of electricity demand. This creates high frequency river stage fluctuations that enhance the connectivity between rivers and groundwater. The central theme explored throughout this dissertation is how hydropeaking effects the movement of water, dissolved solutes, and heat between rivers and their sediments.

Much of the research presented in this dissertation uses numerical models to explore how properties of the river (stage, chemistry, temperature) and subsurface (hydraulic conductivity, groundwater levels) control exchanges of fluid, heat, and solutes, and characterizing how those fluxes alter the chemistry and temperature of sediments

near the river. Two of the studies are entirely modeling-based, focusing on the lateral exchanges of fluid and solutes between rivers and their riparian aquifers caused by hydropeaking. The results provide insight into how dam release and subsurface properties influence surface water-groundwater exchange and also the distance downstream from a dam that exchanges occur over. Other key findings relate to how hydraulic conductivity and groundwater flow conditions of the riparian aquifer control fluid and solute exchange, how far river-sourced solutes propagate into the riparian zone, and factors influencing aerobic respiration in the banks of hydropeaked rivers. In another study, field observations of riverbed temperatures from a hydropeaked river are combined with flow and heat transport modeling. The results demonstrate that hydropeaking releases can strongly influence the temperature of the riverbed near the river bank, but not over the majority of the channel. A final study uses temperature observations from hundreds of rivers across the United States to characterize the mean daily temperature and daily temperature range in different ecoregions. The results from this assessment demonstrate how the thermal regimes of rivers near dams have been altered.

Table of Contents

List of Tables

List of Figures

Chapter 1: Introduction

1.1 Background

The widespread use of dams to impound rivers for water supply, flood control, and electricity generation through hydropower has resulted in a multitude of environmental impacts. Many of these impacts are related to how dams substantially alter the natural flow conditions, temperatures, and connectivity of rivers, which have consequences for nutrient dynamics, habitat suitability, and the morphology of dammed rivers. Water managers and governments face the challenge of balancing the societal benefits that dams provide against the potential harm they pose to aquatic ecosystems.

Dams that are used for hydropower generation often modulate outflow rates from their reservoirs in response to power demand. This results in daily swings in river discharge because power demand follows a daily cycle of peaking in the daytime and subsiding at night. The practice of releasing water during high energy demand periods and then holding water back during low-demand periods is called hydropeaking. In its most extreme form, hydropeaking can create river flow regimes that oscillate between flood levels and low flows on a daily basis, as outflow from the dam is turned on and off. A comprehensive assessment of hydropower dams in the United States by McManamay et al. (2016) identified 349 dams that are regularly hydropeaked. Throughout my PhD their analysis has served as a reminder that the modeling studies I have worked on sitting behind a desk are relevant to processes happening over many thousands of river kilometers in many hundreds of rivers across the United States.

The objective of the research in this dissertation is to advance understanding about surface water-groundwater (SW-GW) exchange flows in hydropeaked river environments. Many of the research questions that I pursued were influenced by field

studies on SW-GW exchange in the nearby Lower Colorado River. The studies showed that the daily dam releases, which raise the river level by 1-2 meters on a daily basis, cause river water move into and out of the river banks in a rhythmic fashion. This temporary movement of river water into the river banks during the river stage increases and subsequent return flow of infiltrated water after the river level recedes is called bank storage exchange. Bank storage exchange is not unique to hydropeaked rivers. In fact, it is a topic that has been studied over at least the last half century by hydrologists. However, what makes bank storage exchange an interesting process to investigate in hydropeaked rivers is that it happens much more frequently than in natural rivers. The effects of daily bank storage exchanges on water, energy, and nutrient balances in dammed rivers is an emerging area of study with many unexplored research questions. Chapters 2 and 4, which form well over two thirds of this dissertation by length, use models to study bank storage exchange flows on water exchange and dissolved organic carbon dynamics under hydropeaking conditions. Chapter 3 uses field data and models assesses the effect of fluid and heat movement caused by hydropeaking on the thermal regime of riverbed sediments. The focus of Chapter 5 is also temperature. It presents a concise analysis of river temperatures in the United States. The results lend insight into the natural temperature variability of rivers depending on river size, location, and season, and how show how dam operations can influence the daily temperature variability of rivers.

1.2 Inspiration on The Lower Colorado River in Texas

The Lower Colorado River near Austin, TX has been a natural field laboratory for studying SW-GW interactions caused by hydropeaking for many of my predecessors in the Cardenas group. Doing field research on the Lower Colorado was my first experience

in planning and executing academic research. While none of the work appears in the following chapters, I collected many months of field data on the Lower Colorado River near Austin, TX during the first two years of my PhD. Despite not culminating in a cohesive study, many of the research questions pursued in this dissertation were inspired by thoughts that I had during numerous field excursions between 2015 and 2017. A few of the ideas came under the dim glow of dawn when I was heading out for a day on the river, some others came when I was sun-drunk and dehydrated after long, hot days spent in the field, and many came during the wee hours of the night staring blearily at puzzling features in time series plots of field data, trying to make sense of what the squiggles on the plots were saying about the processes I was trying to understand. The following chapters are my efforts to shed light on surface water-groundwater dynamics in hydropeaked rivers. My hope is that this work serves as a stepping stone for further studies that improve understanding of linked hydro-biogeochemical processes in dammed rivers that can inform and assist with the management of dammed river ecosystems for mutually beneficial societal and ecological outcomes.

1.3 Longitudinal Analysis of Dam-Induced SW-GW Exchange

Chapter 2 is an analysis of how floods caused by hydropeaking transfer water into riverbanks as they travel downstream from the dam. It uses computer models to create an artificial river where I could test in a systematic way how dam release properties and groundwater flow conditions in the adjacent riparian zones control bank storage exchange along a distance of 100 km downstream from the dam. The two novel aspects of this study were (1) to use a surface water routing model to simulate how dam releases manifest themselves over a 100 km length of river and (2) to then use the stage fluctuations from the surface water model to conduct groundwater flow simulations of

bank storage exchange over the entire 100 km distance. The results showed that typical hydropeaking releases can causes bank storage exchange over long distances, and that groundwater flow conditions are an important factor controlling the amount of exchange.

1.4 Effect of Hydropeaking on The Thermal Regime of Riverbed Sediment

Chapter 3 shifts from the river bank to the riverbed. It is a study on how hydropeaking affects the temperature of riverbed sediments. Riverbed temperature is important for aquatic habitat of benthic organisms and also because it controls the reaction rates of nutrients. The study combines field observations of riverbed temperature from the Lower Colorado River with a fluid flow and heat transport model based on conditions at the study site. The field data presents a novel dataset of riverbed temperature conditions across an instrumented transect that spanned the entire 70-meter channel at our study site. Instrumenting the riverbed was a tremendous undertaking that was only possible because of the incredibly dedicated work of an honors student who was using the temperature data for their thesis. The field data is the first dataset of its kind to be collected in a large hydropeaked river. The modeling was used to understand the mechanisms that were causing the observed temperatures of the riverbed during hydropeaking releases. The study showed that the riverbed near the bank can have large daily temperature swings as a result of hydropeaking releases, but that most of the channel actually has quite stable temperatures regardless of whether or not there are daily dam releases. The advantage of the modeling was that properties of the riverbank could be varied to see their effect on how riverbed temperatures are influenced by exchange flows caused by hydropeaking. These additional models showed the sensitivity of riverbed temperature to hydraulic properties of the river bank, lending insight into how

the riverbed thermal regime in other hydropeaked rivers, with differing hydrogeological conditions, may be affected.

1.5 Aerobic Respiration in the Riparian Zones of Hydropeaked Rivers

Chapter 4 returns to bank storage exchange. However, instead of looking at processes occurring over long distances of river as in Chapter 2, this chapter is focused on exploring how lateral exchange flows caused by daily hydropeaking influence biogeochemical reactions involving carbon and oxygen in the riparian zone. Reactive transport modeling is used to investigate how bank storage exchange flows caused by daily hydropeaking floods lead to the accumulation and reaction of carbon and oxygen in the riparian zone. It has been hypothesized that exchange flows of nutrients between the river and subsurface as a result of hydropeaking can influence the nutrient dynamics of dammed rivers. While highly simplified, the modeling offers first-of-its-kind estimates of aerobic carbon respiration rates under different hydraulic conductivities, groundwater flow conditions, hydropeaking release durations, and river dissolved organic carbon concentrations. Besides quantifying the amount of river-borne carbon respired during hydropeaking exchange flows, the ratio of carbon that enters the bank compared to the amount that returns to the river is calculated for all of the scenarios. This ratio is useful for comparing how bidirectional the nutrient flux of dissolved carbon is under different conditions. Low ratios represent situations where most of carbon doesn't return to the river, while high ratios represent situations where much of the carbon that flowed into the bank returns to the river. Finally, a subset of the model results are presented as time series snapshots that show the subsurface distribution of dissolved organic carbon and oxygen in the riparian zone over time. The snapshots show how river and field site properties can lead to vastly different sizes of reactive areas in the riparian zone. These results help

inform field studies whose aim is to characterize nutrient dynamics in the riparian zone. The snapshots provide insight about where in the riparian zone samples should be collected to capture the dynamic exchanges occurring during hydropeaking.

1.6 Temperature Variability of Rivers in the Conterminous United States

The last chapter of this dissertation is more tangentially related to the theme of this dissertation. This is because it sprung out of a term project I did in my first semester of graduate school, before I had settled on what the focus of my dissertation would be. It is a short research letter that characterizes the daily temperature range of rivers across the United States. The analysis used stream temperature data from all of the USGS gauging stations in the conterminous US over a 15-year period from 2000-2014. The data was grouped spatially into ecoregions (areas of similar climate) and further categorized by average annual discharge as small (<100 cubic feet per second (cfs), medium (100 cfs-1,000 cfs), or large (> 1,000 cfs) rivers. The data revealed distinct seasonal patterns in daily temperature variability for different ecoregions, and for the different river sizes. To reduce the influence of dams on the results, locations that were 15 km or closer to a dam were filtered out from the analysis and presented separately in the appendices. The results showed that dams shift both the mean temperature and the daily temperature variability of rivers. The motivation of the study was to present for the first time a comprehensive summary of how daily temperature variability in rivers exhibit regional and seasonal patterns. The results are helpful to field scientists who are interested in capturing temporal variability in temperature-dependent processes, and also to modeling-based studies who want to incorporate representative values for daily temperature variability into assessment of temperature dependent processes.

Chapter 2: Analysis of the Effects of Dam Release Properties and Ambient Groundwater Flow on surface Water-Groundwater Exchange Over a 100 km-Long Reach [1,2]

ABSTRACT

Hydroelectric dams often create highly dynamic downstream flows that promote surface water-groundwater (SW-GW) interactions including bank storage, the temporary storage of river water in the riverbank. Previous research on SW-GW exchanges in dammed rivers have been local studies conducted within the bed or the bank, limiting the understanding of these exchanges which occur over potentially hundreds of kilometers. This study evaluates how dam releases affect SW-GW exchange continuously over a 100 km distance. This is accomplished by longitudinally routing water releases through a synthetic river and modeling bed and bank fluid and solute exchange across transverse transects spaced along the reach. Peak and square dam release hydrograph shapes with three magnitudes (0.5, 1.0, and 1.5 m) were considered. The effect of four ambient groundwater flow conditions (very slightly losing, neutral, and two gaining from the perspective of the river) were evaluated for each dam release scenario. Both types of dam release shapes cause SW-GW interaction over the entire 100 km distance, and our results show square type releases cause bank storage exchange well beyond this distance. Strongly gaining conditions reduce the amount of exchange and allow flushing of river-sourced solute out of the bank after the dam pulse has passed. Both neutral and losing conditions have larger fluid and solute flux into the bank and limit the amount of solute that returns to the river. Our results support that river corridors downstream of dams have

increased river-aquifer connectivity, and that this enhanced connectivity can extend at least 100 km downstream.

[1] Ferencz, S. B., Cardenas, M. B., & Neilson, B. T. (2019). Analysis of the effects of dam release properties and ambient groundwater flow on surface water-groundwater exchange over a 100-km-long reach. *Water Resources Research*, 55, 8526 8546. https://doi.org/10.1029/2019WR025210

[2] Stephen Ferencz was the main contributor who performed the research, analyzed the data, and wrote the manuscript

2.1 INTRODUCTION

Dam releases cause river stage fluctuations with timescales varying from hourly to seasonal and with magnitudes ranging from centimeter oscillations to multiple meters. Dam-induced stage fluctuations facilitate the movement of water and solutes between rivers and their adjoining hyporheic and riparian zones and aquifers, often with important consequences for biogeochemical cycling of ecologically important compounds such as nitrate or dissolved organic carbon [*Harvey & Gooseff*, 2015]. As river stage increases, water can flow from the river into the surrounding sediments, filling the unsaturated zone and displacing ambient hyporheic water or groundwater. As the stage subsides, water can flow back towards the river.

The process of filling and emptying of the bank and near-bank riverbed sediments that occurs during stage fluctuations is called bank storage exchange (BSE). BSE facilitates "hydrologic exchange flow" defined by *Harvey and Gooseff* (2015) as the lateral and vertical exchanges of water, materials (solids and solutes), and energy between rivers and their surrounding subsurface waters. Throughout this paper we use BSE to describe the hydrostatically-driven movement of mass (fluid and solute) between rivers and their adjoining sediments, and we use the term BSE-zone to describe the area

of the bank and below the riverbed that receives river water during river fluctuations. Examples of important processes that BSE influences include: contaminant and nutrient dynamics [*Yim and Mohsen*, 1992; *Gu et al*., 2012; *Shaui et al*., 2017], sustaining flows during dry periods [*Kondolf et al*., 1987; *Rhodes et al., 2017*], and attenuating flood pulses [*Pinder and Sauer*, 1971; *Hunt*, 1990]. Interest in studying BSE has grown with the recognition of the important ecosystem services SW-GW interactions provide for nutrient cycling and the overall health and functioning of aquatic environments [*Brunke & Gonser*, 1997; *Harvey and Gooseff*, 2015].

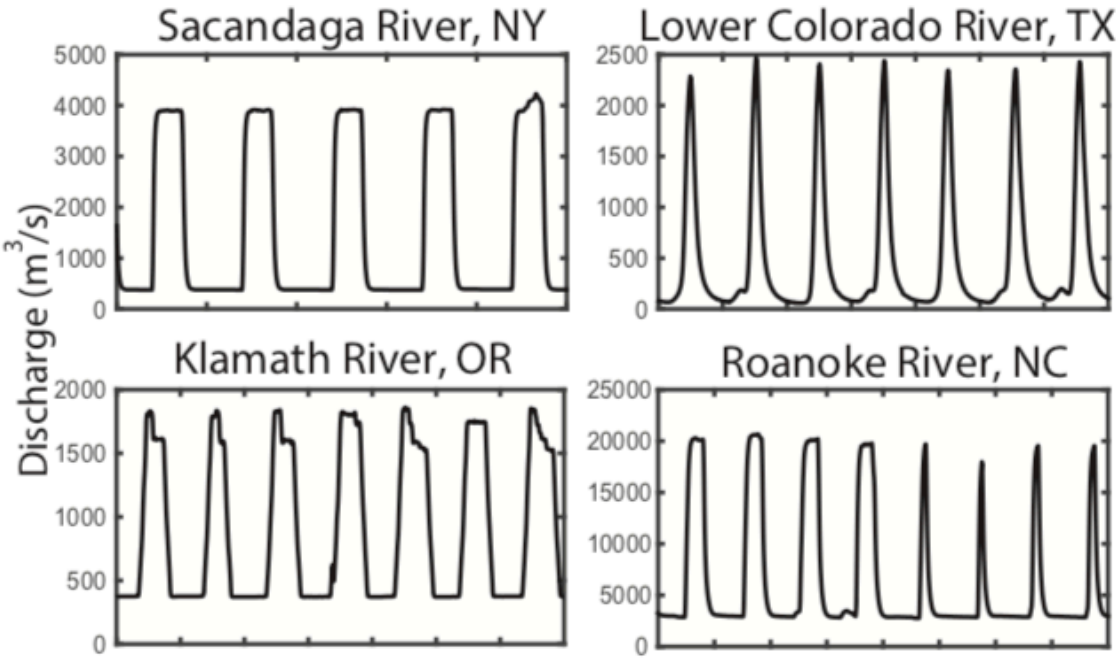

Figure 2.1: Example hydrographs in four hydropeaked rivers in the US

Examples of square and peak dam releases from four regulated rivers in the United States. Square releases typically ramp up to and hold a sustained discharge for several hours, while peak releases tend to quickly ramp up to and down from a high discharge flow regime. Stage fluctuations range from tens of centimeters up to 2 meters or more. x-axis ticks are in days.

Research on BSE processes is a long-studied topic in hydrology and many of the foundational conceptualizations were formulated before the advent of powerful computing now common in the discipline [*Newcomb and Brown*, 1961; *Rorabaugh*, 1963; *Cooper and Rorabaugh*, 1963; *Moench et al*., 1974]. Recently there has been a resurgence of interest in evaluating and understanding BSE processes. A focus of recent research on BSE is in highly dynamic dam-regulated rivers [*Sawyer et al*., 2009; *Yellen and Boutt*, 2015; *Shuai et al*., 2017; *Song et al*., 2018]. The frequency of river fluctuations that cause BSE events is often much higher in dam-regulated rivers than in natural rivers [*Bevelhimer et al*., 2015]. High frequencies of stage fluctuations are common downstream of hydropower facilities where stage fluctuations occur on daily or even sub-daily timescales to meet power demands [*McManamay et al*., 2016]. The hydroelectric management practice of abruptly switching from low flow to high flow to meet energy demands is termed "hydropeaking." Four examples of hydropeaked rivers with daily flow/stage changes controlled by dam operations are shown in Figure 2.1. Although these rivers are distributed across a wide variety of climates (New York, North Carolina, Oregon, and Texas in the USA), their hydrographs are not the result of meteorological events but of daily dam releases.

The increased regularity of BSE events in dam-regulated rivers creates unique river environments characterized by frequent stage oscillations. The regions where rivers experience high frequency dam-induced flooding events can extend over tens to even hundreds of kilometers downstream from dams [*Kennedy et al*., 2016]. In the United States there are hundreds of dams that are hydropeaked [*McManamay et al.*, 2016], and worldwide it has been estimated that over half of Earth's river systems have been altered for electricity generation [*Rosenberg et al*., 2000]. Additionally, it is likely that more hydropower plants will be brought online in the 21st century because hydropower is

viewed as a green, low-cost source of energy production that has a smaller carbon footprint than energy production via conventional hydrocarbon power plants [*Jones*, 2014]. Developing a complete understanding of the hydrology of dam-regulated rivers is essential to understanding the ecosystem and water resource implications of dam operations. One component of building a comprehensive picture of how dam operations affect river ecosystems is understanding their effect on BSE.

The vast majority of the research on BSE has been focused on understanding the mechanistic controls on BSE processes at the plot transect scale, typically a few to tens of meters. Field and modeling studies at the transect scale typically study BSE processes at an individual 2D transect oriented perpendicular to the channel [*Rorabaugh* 1963; *Squillace* 1996, *Chen & Chen* 2003; *Koussis et al*., 2006; *Doble et al*., 2012]. Few studies have looked at spatial and temporal BSE dynamics from a longitudinal perspective [*Pinder and Sauer*, 1971; *Xie et al*., 2016; *Liang et al.*, 2018]. Each of these studies evaluated the effect that a flood wave moving down a river corridor has on the spatiotemporal BSE. However, in each study, the flood waves modeled were based on natural flood hydrographs that are not representative of typical hydropeaking releases (Figure 1).

As a dam release propagates downstream, the flood wave is attenuated causing a decrease in wave height and an increase in wavelength. *Liang et al.* (2018) conducted a modeling study that examined how changes in the shape of a flood wave create changes in rates of BSE flux. Their work supports the idea that as the shape of dam-induced flood wave changes as it travels downstream, so too does the resulting rates and quantity of BSE. Therefore, to understand the cumulative importance of BSE in dam-regulated rivers, it is necessary to use a longitudinal approach that accounts for the longitudinal

changes in SW-GW exchanges via BSE that result from the attenuation of realistic dam-induced flood waves.

To systematically quantify the effects of dam operations on SW-GW exchanges with both high resolution and over large distances, we used numerical models to test the effect of flood waves from synthetic dam releases on bank storage exchange over a distance of 100 km. We modeled two dam release flood shapes that are common in hydropeaked rivers and considered three flood wave sizes, ranging from 0.5 m to 1.5 m in amplitude. Our approach couples propagating realistic dam releases along a 100-km idealized river using the US Army Corps of Engineers surface water routing model HEC-RAS, and then simulating the resulting BSE using a finite-element model of 2D variably saturated subsurface flow implemented in COMSOL Multiphysics, a commercial finite-element modeling software. Our models also consider the effect of ambient groundwater flow conditions to explore the interaction of the dam releases with losing, neutral, and gaining groundwater conditions in the river bank. In addition to testing a range of ambient groundwater flow conditions, we also varied hydraulic conductivity to test how this key parameter influences longitudinal BSE. We use both volume of fluid exchange and area of the bed and the bank that river solutes infiltrate as metrics for comparing the amount of SW-GW interaction resulting from the different model scenarios. While the models include the bed of the river, we collectively refer to the exchange as BSE since it is dominated by bank rather than bed exchange.

2.2 METHODS

2.2.1 Simulated Dam Signals and Experimental River Properties

Dam signals reflective of realistic conditions for a river downstream of a hydropeaking facility were used for this study. We considered two dam release shapes

that are present in hydropeaked rivers (Figure 2.1). The first shape looks similar to a square wave where discharge (power generation) ramps up to and is held at a sustained level for several hours. The other type is an abrupt peak shape that ramps up to a maximum height and immediately declines. The square releases were modeled with sustained maximum discharge held for 8 hours, while the peak releases only had a maximum discharge for 15 minutes. We evaluated three sizes of hydropeaking releases whose discharge resulted in stage changes immediately below the dam of 0.5, 1, and 1.5 meters. These are common amplitudes for hydropeaking releases in rivers in the United States.

We used a simple, idealized channel geometry and fixed channel properties (slope, width, roughness) for our synthetic river to constrain the number of variables under consideration. This allowed us to isolate and test the effects of (1) different dam release scenarios and (2) ambient groundwater conditions on BSE. Similar simplifying assumptions about channel dimensions and properties have been made in other longitudinal BSE studies [*Pinder and Sauer*, 1971; *Xie et al*., 2016; *Liang et al.*, 2018]. The experimental river was given a constant width of 80 m and a slope of 0.0005. The slope is representative of a higher-order, lowland river such the Brazos, Nueces, and Lower Colorado rivers in Texas; other familiar examples include the Missouri and Arkansas Rivers [*Larkin and Sharp*, 1992]. These values are almost identical to the average width and slope of the hydropeaked Lower Colorado River, Texas, USA which has been the focus of numerous dam-induced SW-GW exchange studies over the past decade [*Sawyer et al*., 2009, *Gerecht et al*., 2011; *Watson et al*., 2018].

While not the focus of this study, to demonstrate how changes in roughness and channel slope influence longitudinal patterns in BSE we ran a small number of models in which two other roughness values and one other channel slope were considered. The two

additional roughness values spanned the extremes expected for a river, ranging from a minimum value of 0.025 and maximum value of 0.05. The other channel slope we modeled was twice as steep as the one used for this study (0.001 vs. 0.0005). Because a comprehensive assessment of channel roughness and slope is outside the scope of this study, we only tested a 1 m peak release and only quantified longitudinal BSE using volumetric inflow into the bank.

2.2.2 Flow and Transport Model Description

2.2.2.1 Governing Equations

The 1D surface water routing was modeled using HEC-RAS version 4.1.0 (U.S. Army Corps of Engineers, HEC-RAS, Hydrologic Engineering Center), which solves the conservation of mass and momentum equations for a dynamic wave. The transient response of river stage to a dam release is represented by the dynamic form of the 1D Shallow Water Equations. The coupled mass (Eq. 1) and momentum (Eq. 2) equations that govern transient surface water flow were solved numerically using a four-point implicit finite difference approach with a weighting factor Θ = 1, which has been shown to be unconditionally stable [*US Army Corps of Engineers Hydraulic Engineering Center*, 2016]. The equations are as follows:

$$\frac{\partial A}{\partial t} + \frac{\partial (Au)}{\partial x} = 0 \tag{1}$$

$$\frac{\partial u}{\partial t} + u\frac{\partial u}{\partial x} + g\frac{\partial \zeta}{\partial x} = -\frac{P\tau}{A\rho} \tag{2}$$

where A is channel cross-sectional area [L^2], u is flow velocity [LT^-], x is the longitudinal downstream direction [L], g is gravitational acceleration [LT^{-2}], ζ is the free

surface elevation [L], P is the wetted perimeter of the channel [L], τ is the wall sheer stress [$MT^{-2}L^{-}$], and ρ is the fluid density [ML^{-3}].

The fluid flow and solute transport between the river and aquifer was solved by coupling flow in unsaturated porous media based on Richard's equation (Eq. 3) and solute transport based on the advection-dispersion equation (Eq. 4). The coupled subsurface flow and transport equations were solved with a segregated solver that evaluated the fluid flow and solute advection-dispersion equations sequentially.

$$\rho\left(\frac{C_m}{\rho g}+S_e S\right)\frac{\partial p}{\partial t}+\nabla\cdot\rho\left(-\frac{k_s}{\mu}k_r(\nabla p+\rho g\nabla z)\right)=Q_m \tag{3}$$

$$\frac{\partial}{\partial t}(\theta C)=-\nabla\cdot\rho(qC)+(D\nabla^2 C) \tag{4}$$

where p is pressure [$MT^{-2}L^{-}$], ρ is fluid density [ML^{-3}], C_m is specific moisture capacity [L^{-}], S_e is effective saturation [-], S is the storage coefficient [-], k_s is the saturated hydraulic permeability [L^2], k_r is the relative permeability dependent on saturation [-], μ is the dynamic viscosity of the fluid (water) [$ML^{-}T^{-}$], z is the elevation head [L], g is gravitational acceleration [LT^{-2}], and Q_m is a stress source term that accounts for changes in total stress under fluctuating river stage [$ML^{-3}T^{-}$]. C is the concentration of the conservative solute [ML^{-3}], θ is the volumetric water content [-], q is the Darcy velocity [LT^{-}], and D [L^2T^{-}] is the effective dispersion coefficient which includes the macro-dispersion tensor, defined by dispersivity and pore velocity, plus molecular diffusion.

2.2.2.2 Surface Water Model Configuration

We used a 1-D routing model to simulate the river stage response to different dam release scenarios. The geometry and boundary conditions for the 1-D surface water

model were set to a constant channel width of 80 m, slope of 0.0005, Manning's roughness of 0.035, and trapezoidal cross-sectional shape with the bank sloped at 70° (Figure 2.2a). A small number of additional simulations were conducted to test two other roughness values (0.025 and 0.05) and one other channel slope (0.001). The upstream inflow boundary condition was a transient stage specified for the desired dam release shape and magnitude. The downstream outflow boundary condition was set as a friction slope. To ensure that backwater effects at the downstream end of the model domain did not influence the upstream river stage response, we evaluated the dam release simulations over a 200 km domain of which only the first 100 km of river stage data was used.

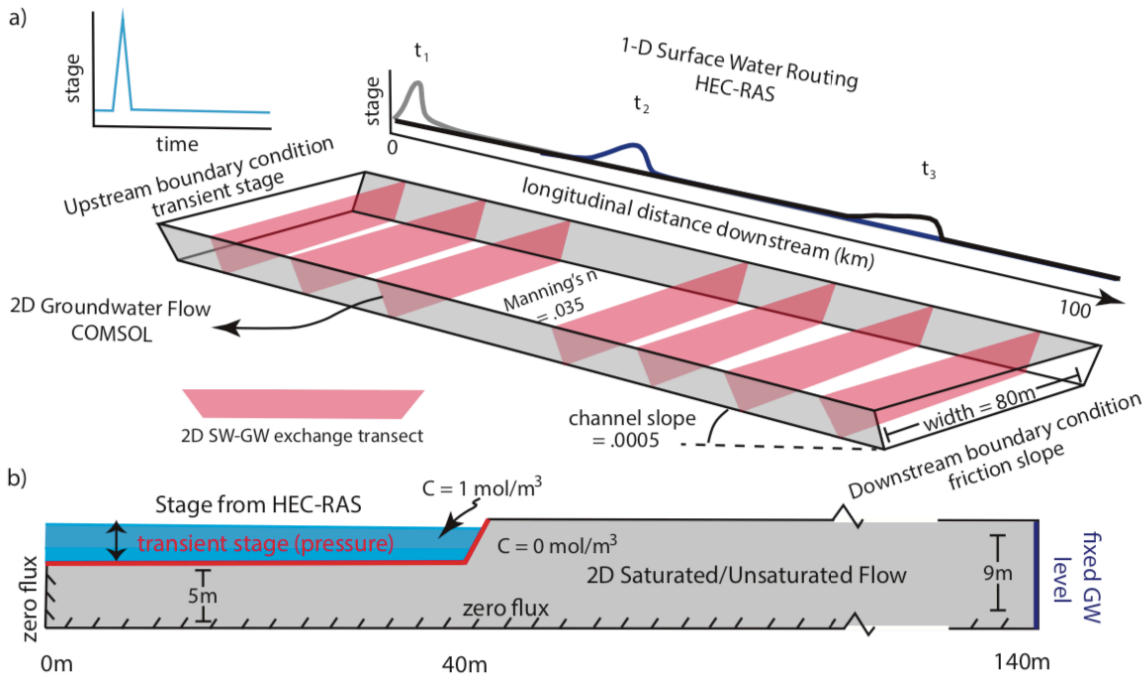

Figure 2.2: Linked longitudinal-transverse modeling schematic

Schematic of the longitudinal-transverse model design for this study. The surface water routing for the dam release was modeled as a 1-D dynamic wave following the 1-D St. Venant Equations, and was implemented in US Army Corps HEC-RAS. Time series of river stage response to dam releases were exported from HEC-RAS and used as pressure boundary conditions for 2D Richard's flow models run in COMSOL Multiphysics.

The model was evaluated with a grid spacing of 1 km and time steps of 30 seconds. Appropriate grid spacing was determined using an equation that relates bank full depth and bed slope [*US Army Corps of Engineers Hydraulic Engineering Center*, 2016]. Time series of river stage were exported at the desired transverse groundwater model locations between the dam and 100 km downstream. The hydrographs generated from the HEC-RAS models were used as the river stage boundary conditions at specific locations for the 2-D subsurface flow models (Figure 2.2).

2.2.2.3 Subsurface Flow and Transport Model Configuration

The subsurface modeling domain was 140 m in length (40 m channel and 100 m bank) and the unconfined alluvial aquifer was given a depth of 5 m beneath the riverbed and 9 m in the bank (Figure 2.2b). To reduce the size of the modeling domain, the river transect was modeled as a half-width. The aquifer hydraulic properties for the base case were homogenous and isotropic with constant saturated hydraulic conductivity K of 10 m/d (with ρ = 998 kg/m^3 and μ=1.002 mPa-s, this corresponds to k_s=1.2×10^{-11} m^2) and had a porosity of 0.3, representative values for medium sand. A small subset of models tested the effect of K on BSE flux and considered two additional K values of 1 m/d and 50 m/d. The van Genuchten parameters were 10 m^{-1} for α and 2 for n. No flow (zero flux) boundaries were assigned to the aquifer base and at the symmetry boundary at the left-hand side (i.e., the center of the channel). The top boundary of the model was set as a seepage face to realistically capture the filling and draining of the riverbank as the river stage fluctuates. The seepage face was implemented as a mixed boundary using a conditional statement that partitions elements along the top boundary into zero-pressure for elements along the seepage face and zero-flux for elements that are above the seepage face. Pressure along the top boundary of the flow model was set as a time-varying head

boundary parameterized from the river stage hydrographs generated in HEC-RAS. The right boundary (as shown in Figure 2.2) was set as constant head and was used to control the ambient groundwater gradient – defined as the difference between the right-hand boundary and the background river level divided by the 100 m width of bank. The lateral extent of the domain was chosen so the range of stage fluctuations considered would not result in water level fluctuations at the right-hand boundary.

We used a conservative solute as the tracer to track the growth of the BSE-zone under the different dam release scenarios and ambient groundwater configurations. The initial solute concentration in the subsurface transport model was set to 0 mol/m^3. The portion of the top boundary that was at or below the river stage was given an arbitrary constant solute concentration of 1 mol/m^3, representing the conservative solute tracer in the river (C_{riv}). Horizontal dispersivity was set to 1 m and vertical dispersivity was set at 0.1 m ($1/10^{th}$ of longitudinal). The molecular diffusion coefficient of the conservative solute was set at 10^{-10} m^2/s. In order to solve unsaturated flow and transport under highly transient conditions we used a small triangular element size (ranging from 0.01 m along the bank up to 0.3 m at further distances) and time step size (maximum 100 seconds) to maintain numerical stability and to minimize numerical dispersion.

2.2.3 Ambient Groundwater Condition Scenarios

In the absence of stage fluctuations, gaining and neutral groundwater conditions limit the exchange of river water with bank. The multiple dam release shapes and sizes that were evaluated and the large longitudinal scale over which we simulated dam-induced BSE limited the number of ambient groundwater conditions that could be considered. We chose to model two different gaining groundwater conditions, one "strongly" gaining with a gradient of +0.015 towards the river and the other "moderately"

gaining with a gradient of +0.0075. The neutral gradient was also included as a baseline comparison and also representative of banks that have very gently sloping water tables (either very weakly gaining or losing). We also examined the effect that transient stage fluctuations would have on the amount of fluid and solute movement from the river into the bank under losing conditions and how this would differ from the background state. Since this was not the primary focus of this study, dam release scenarios were only tested for one value (head gradient = -0.0075).

2.2.4 Hydraulic Conductivity Scenarios

Hydraulic conductivity is a key control on rates of fluid and solute transport in porous media, and thus could be important for longitudinal distribution of BSE fluxes. A priori, it is not apparent how hydraulic conductivity would affect the longitudinal distribution of BSE for a propagating dam release, and this is further complicated if one considers how variations in K interact with different ambient groundwater conditions. To explore the effect of varied hydraulic conductivity on longitudinal BSE we evaluated volumetric BSE flux for two additional aquifer K of 1 m/d and 50 m/d. For this set of scenarios, we considered 1 m peak and square dam signals with neutral and gaining (0.0075 and 0.015) ambient groundwater conditions.

2.2.5 Quantifying Volumetric Flux and Solute Area in the Riverbank

The two metrics used to quantify SW-GW exchanges under the different dam release and groundwater flow scenarios are (1) volumetric fluid flux and (2) subsurface area inundated by the river sourced solute (BSE-zone), which can also be viewed as the hyporheic zone extent.

Volumetric exchange flux is one of the most common metrics quantified in field and modeling studies of BSE. In field studies, volumetric flux is typically inferred from estimating Darcy fluxes based on gradients between water levels in monitoring wells and the height of the river [*Sawyer et al.*, 2009; *Welch et al*., 2014]. Field estimates of volumetric BSE flux are time, labor, and cost intensive, which is why volumetric flux values are more commonly reported in numerical modeling studies of BSE processes [*Chen and Chen*, 2003; *Doble et al*., 2012; *Welch et al*., 2013]. Volumetric flux is important to understanding the influence of short-term (natural or man-made) flood events on longer-term chemical composition and water balance between rivers and their alluvial aquifers [*McCallum and Shanafield*, 2016]. Volumetric flux can also serve as a proxy for the potential for biogeochemical transformations of solutes as shown in *Gu et al.* (2012).

The size of the BSE-zone was evaluated because it is a controlling factor for the ecological function of riverbanks as hot spots of biogeochemical processing. Because a conservative solute was modeled, the simulation does not capture the formation of redox zones in the bank that exert control over the types of biogeochemical reactions that occur (e.g., *Boano et al*., 2010; *Shuai et al*. 2017). However, using a conservative solute provided the computational flexibility to run hundreds of simulations to evaluate controls on BSE at the longitudinal scale of 100 km. Opinions about what percentage of river water chemically constitutes the hyporheic zone vary. A commonly used value is greater than 10% river water suggested by *Triska et al.* (1989) three decades ago. There also are much looser definitions such as *Findlay* (1995) who defined the hyporheic zone as the region of the subsurface that contains any percent river water. Both definitions are based on arbitrary values and are not determined by the effects these concentrations would have on hyporheic zone biogeochemical processes. We chose to evaluate solute area for

quartiles of river concentration, generating a time series of the area in the bank where the concentration of the pore water (C) is greater than or equal to 25%, 50%, 75%, or 95% of the river concentration (C_{riv}). The figures in the main text present the results for the > 25% river water concentrations ($C/C_{riv} > 0.25$). The results for the other three quartiles are presented in SI Figures 1-3.

Time series of boundary fluid flux and subsurface solute area were exported from the subsurface flow simulations every 1,000 seconds. These results were then used to calculate volumetric BSE flux and changes in the size of the BSE-zone. The total fluid flux was calculated by integrating the net boundary flux across the top boundary (river bed and bank), and volumetric flux was calculated by integrating the fluid flux rate through time. The solute area was obtained by integrating the area of the model domain containing solute concentrations greater the specified concentration value.

2.3 RESULTS

2.3.1 River Stage Response to Dam Release Scenarios

The two types of dam release resulted in different longitudinal patterns in river stage fluctuations (Figure 2.3). A key difference between the peak (Figure 2.3a) and square releases (Figure 2.3b) is that the flood wave created by peak releases decays much more rapidly than the square releases. The rapid decay of the peak flood wave compared to the square flood wave shows time series of river stage at locations of 10, 30, 60, and 90 km downstream from the dam for the three sizes of dam release (0.5, 1.0, and 1.5 m). Comparing the flood waves of the 1.5 m peak and square releases at 30 km downstream illustrates the more rapid attenuation of the peak releases: at this location the peak release has a height of 0.7 m (46% of initial size) while the square release has a height of 1.45 m (96% of initial size). Large decay in wave height for the peak releases and small amounts

for square releases is consistent for all three sizes of dam releases. The wavelengths of the flood waves created by both types of dam release increase as they travel downstream. The attenuation of the peak releases increased the wavelength from 5 to 17 hours while the wavelength of the square releases increased from 11 to 23.5 hours. Differences in the hydrographs created by the peak and square releases resulted in characteristic longitudinal distributions of BSE for the two release shapes.

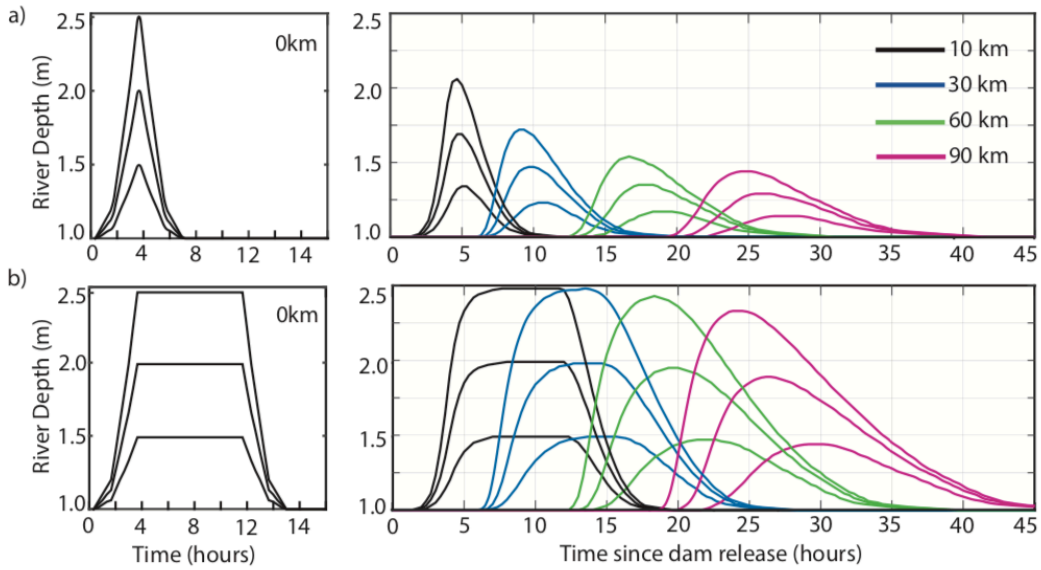

Figure 2.3: Simulated dam release hydrographs at 10, 30, 60, and 90 km downstream Idealized peak (a) and square (b) dam release signals used for bank storage exchange models, and resulting river depth changes are shown at 10 km, 30 km, 60 km, and 90 km downstream from the dam. Stage hydrographs were used as time-varying head boundary conditions for the bank storage exchange models.

2.3.2 Snapshots of Flow Field and Solute Distribution Under Different Dam Release Signals and Ambient Groundwater Flow Conditions

The 2D lateral exchange models show that the spatiotemporal response of the flow field and solute distribution in the riverbank to be highly dependent on the dam release type (peak versus square) and ambient groundwater flow conditions (Figure 2.4).

These snapshots from 1 m peak and square releases at a transect 90 km downstream of the dam illustrate infiltration during river stage rise and exfiltration as the river stage returns to its original level. The last snapshot is at 24 hours because under repeating daily hydropeaking conditions a dam release would be arriving and initiating another BSE event. Therefore, the snapshots at 24 hours show the maximum recovery to ambient, pre-dam release conditions.

Similar to the findings of *Welch et al*. (2013) and *Shuai et al*. (2017), gaining river conditions limit infiltration of river water and accompanying solute during stage the increases (Figure 2.4 c & f). Clear differences in the size of the BSE-zone during infiltration are apparent depending on the ambient groundwater head gradient. The ambient groundwater head gradient also controls the exfiltration or return flow of solute

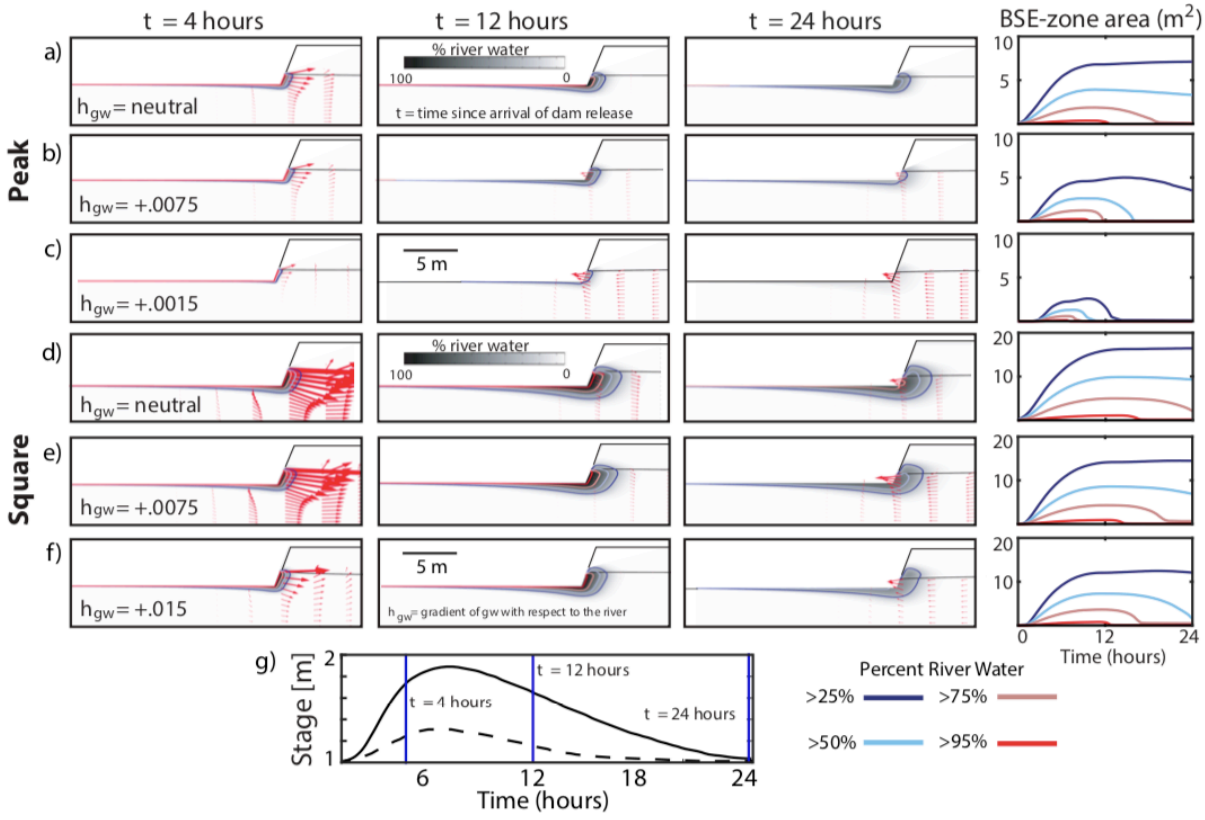

Figure 2.4: Snapshots of flow field and solute distribution in riverbank at 90 km

Snapshots of flow field and river-sourced solute concentration in the bank over a 24-hour period at 90 km downstream resulting from 1 m peak (a-c) and square (d-f) releases. The effect of three different ambient groundwater head ranging from neutral (a and d), +0.0075 (b & e), and +0.015 (c and f). The peak and square hydrographs annotated with each snapshot time are shown in (g) - peak is dashed and square is solid. The size of the area in the bank that has pore fluid concentrations defined as a percentage of river concentration (>25%, >50%, >75%, and >95% river water) are shown in the right-most column.

back into the river. The effect of ambient groundwater gradients on the capacity to flush solute out of the bank can be seen by comparing the extent of river-borne solute in the riverbank at t = 24 hours for the three ambient head gradients (Figure 2.4 a-f). The snapshots show that larger groundwater head gradients, and thus more flow towards the river, result in BSE-zone areas with smaller extent and lower solute concentration.

A common feature of all of scenarios is that lateral flow into the bank, not vertical flow into the riverbed, is the primary mechanism of SW-GW exchange during stage fluctuations. This can be seen both in the size of the flow vectors (red arrows), which are scaled to reflect magnitude of fluid velocity, and in the distribution of river-sourced solute (shown in greyscale) in the subsurface (Figure 2.4). Another important feature shared by all six scenarios is that some amount of solute remains in the bank after 24 hours. Under conditions of repeating dam releases this would result in an accumulation of solute in both the saturated and unsaturated zone of the bank.

Comparing the peak and square snapshots, one can see that the square release results in the transport of considerably more river-sourced solute into the river bank than the peak release. This difference is attributed to the larger amplitude and longer duration of the square flood wave compared to the peak (Figure 2.4g). In addition to transporting more solute into the bank, the longer wavelength of the square release permits a shorter period for exfiltration (i.e., less time to return to background, pre-flood wave conditions). This can be seen by comparing the solute distribution at t = 24 hours for the peak and the square scenarios. This suggests that under repeating stage fluctuations, square releases

would develop a laterally extensive zone of GW-SW mixing in the riverbank more rapidly than peak releases.

2.3.3 Longitudinal Results: Neutral and Gaining Groundwater Flow Conditions

2.3.3.1 BSE Volume Under Neutral and Gaining Groundwater Flow Conditions

We quantified net volumetric BSE flux at each model transect, expressed as m^3 per meter of bank, to illustrate the longitudinal distribution resulting from a dam release moving downstream. For each dam release scenario, the effect of ambient groundwater gradient on volumetric flux is shown for three ambient groundwater conditions (see different colored curves in Figure 2.5). Each point represents a result from a 2D transect groundwater flow model simulation and shows that the volumetric fluxes results are dependent on dam release type and size, distance from dam, and ambient groundwater head gradient. Net volumetric flux volumes range from as large as 3 m^3/m of bank for the largest square release to no net exchange in the case of the smallest peak release under the strongest gaining conditions. Because of the smaller wave height attenuation and longer duration of elevated river stage, square releases cause a much larger volumetric flux than the same size peak release. In fact, the largest volumetric flux for a peak pulse of ~2 m^3/m bank was approximately equal to the amount for the smallest square release under neutral conditions.

The ambient groundwater head gradient is an important factor for all dam release scenarios. More strongly gaining groundwater flow conditions resulted in sizeable reductions in volumetric flux. The groundwater head gradient also had a larger effect on reducing volumetric flux with increased longitudinal distance from the dam. To quantify the effect of head gradient, we compared the reduction in volumetric flux under the strongest gaining conditions compared to neutral conditions. The percentage reductions

of the volumetric flux for the peak releases were 29%, 39%, and 51% at the dam (0 km) and 75%, 87%, and 100% at 100 km downstream, for 1.5, 1.0, and 0.5 m release sizes, respectively. For the square releases, the percentage reductions were 18%, 27%, and 53% near the dam (0 km) and 26%, 37%, and 69% at 100 km downstream for 1.5, 1.0, and 0.5 m release sizes.

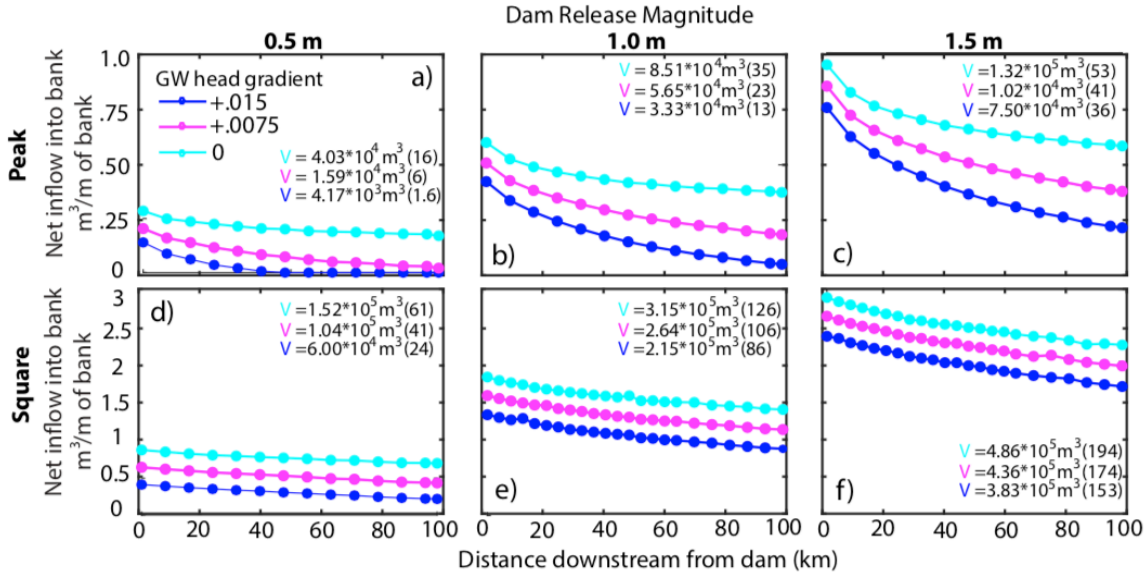

Figure 2.5: Bank storage exchange volume under varied dam scenarios and groundwater flow conditions

BSE volumes along the 100-km river distance for the different dam release scenarios and groundwater gradients. The three different ambient groundwater gradients were modeled for each scenario - shown in cyan (neutral), magenta (+0.0075), and blue (+0.015). The cumulative volumetric inflow of river water into the banks along the entire 100 km length downstream from the dam is provided in both cubic meters and in parentheses the equivalent number of Olympic swimming pools.

Another way to evaluate the effects of different dam release scenarios and ambient groundwater conditions is to quantify the cumulative volumetric exchange over the entire river length (100 km) during the entire flood period (24 hours). Cumulative

exchange values, *V,* are provided in cubic meters and, for a familiar physical reference, as the equivalent number of Olympic-size swimming pools (Figure 2.5). The cumulative exchange volumes highlight the effects of shape, size, and ambient groundwater head gradient on the amount of bank storage resulting from these different scenarios. The exchange volume was as small as 4.17×10^3 m^3 (0.5 m peak, head gradient = 0.015) or as large as 4.86×10^5 m^3 (1.5 m square, neutral head gradient). Dam release properties and ambient groundwater head gradient conditions can result in a two order of magnitude range in cumulative BSE volume over the 100-km segment downstream from the dam (Figure 2.5).

2.3.3.2 Solute Area Under Neutral and Gaining Groundwater Flow Conditions

To test how dam release properties and ambient head gradients control the size of the BSE-zone, we quantified the area in the bank that was infiltrated by the conservative solute tracer from the river defined as $C/C_{riv} > 0.25$. Because the duration that the river water resides in the river sediments is also a potentially important factor for biogeochemical reactions involving river-borne solutes, the BSE-zone area is presented as a time series (Figure 2.6). The dam release properties (shape and size), ambient groundwater head gradient, and proximity from the dam are important factors for both the maximum size and persistence of the BSE-zone area (Figure 2.6). The usefulness of this simple metric is demonstrated by comparing the BSE-zone area for square and peak releases. It is readily apparent that peak releases not only result in much smaller BSE-zones, but that the BSE-zones are much less persistent, particularly for smaller peak releases under gaining groundwater head gradients (Figure 2.6).

As stage increases during the rising limb of the dam release flood pulse, the BSE-zone area increases as river water is advected into the bank. For neutral conditions, there

is no opposing groundwater head gradient towards the river to limit the advection of solute into the bank so the size of the BSE zone grows most rapidly and reaches the largest extents under these conditions (Figure 2.6). The effect of gaining river conditions (Figure 2.6) show that the presence of positive ambient groundwater head gradients results in a smaller BSE zone area. The modeling results provide insight into the relative influence of ambient groundwater flow conditions on size of the BSE-zone created by the different dam release scenarios. It can be seen that the effect of groundwater head gradient is much more limiting for the peak releases than for the square.

As stage recedes the solute area shrinks as solute that was transported into the bank is advected back into the river. For neutral conditions, the area decreases only a small amount because head gradients that favor return flow are short-lived (Figure 2.6). As the river stage recedes, the groundwater in the bank returns closer to its background state of zero gradient with no ambient groundwater flow to flush solutes back to the river. In contrast, ambient gaining groundwater flow conditions allow for long-term, sustained flushing of the solute from the BSE-zone back into the river, which can be seen in the solute area declining (Figure 2.6). When considering the solute area over a 24-hour period, it can be seen that with the exception of the 0.5 m peak pulse under the strongly gaining conditions (0.015), both peak and square releases result in an expansion of the BSE zone in the bank that does not recover to pre-release conditions (Figure 2.6).

The maximum solute area at each transect along the 100-km longitudinal distance was integrated to obtain a cumulative BSE zone volume that resulted from the dam release scenarios and groundwater conditions. Under neutral or gaining conditions there would be no lateral movement of solute between the river and its banks without the transient BSE caused by the stage fluctuations.

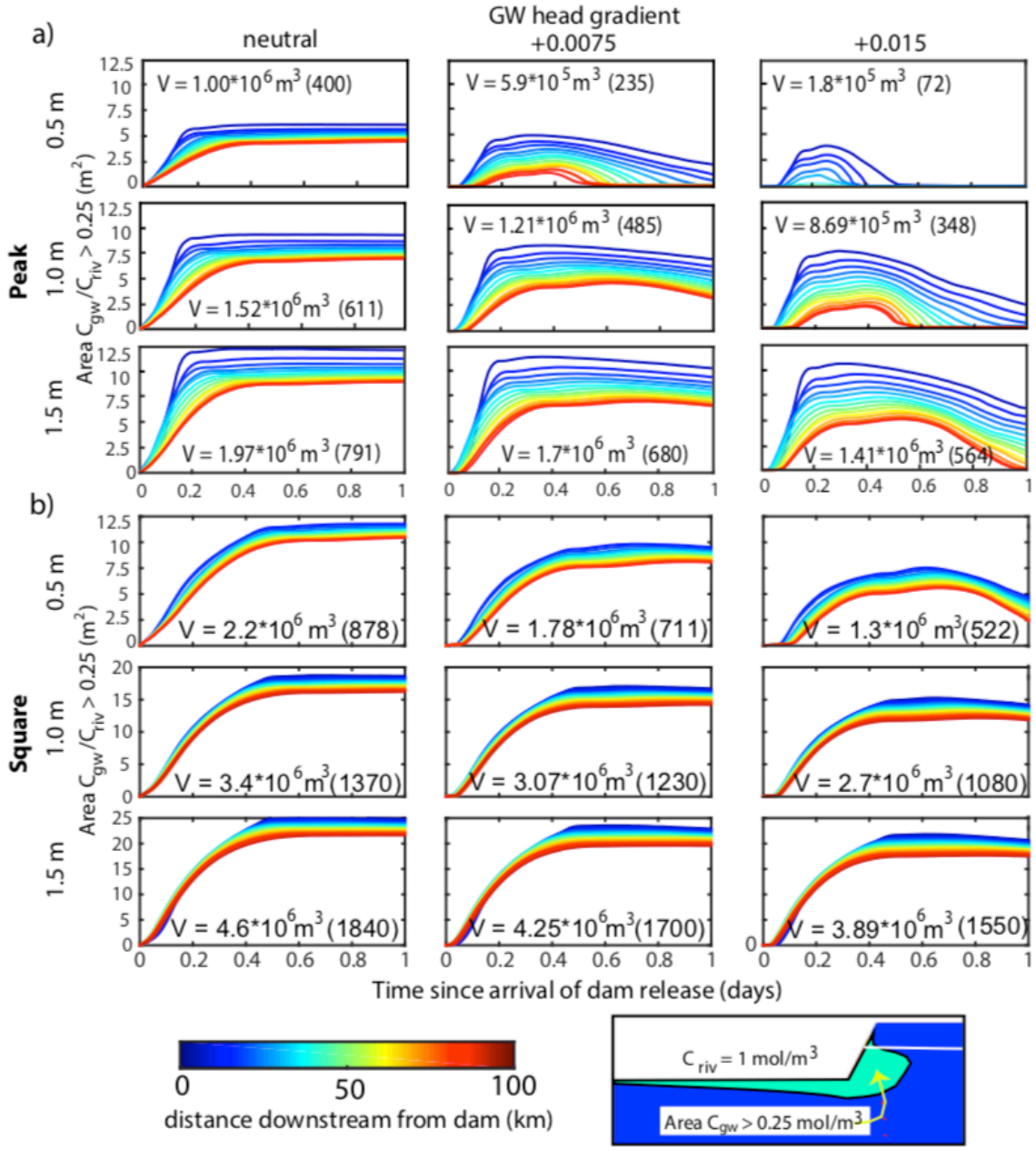

Figure 2.6: Time series of BSE-zone size under neutral and gaining groundwater flow conditions

Time series of BSE-zone size during dam releases show area in bank inundated by solute transported from the river into the riverbank. Attenuation of dam release signals as they travel downstream causes differences in timing and size of solute area in the bank with longitudinal distance (colorbar). The cross-sectional areas were used to calculate a total volume of BSE-zone (V) created along the 100 km river length for each scenario. Parenthetical values indicate the volume in equivalent number of Olympic swimming pools. The volume can be thought of as the size of hyporheic zone created by the dam releases.

The cumulative volumes show how much the size of the BSE zone was expanded due to the dam releases (Figure 2.6). Instead of representing a total amount of fluid exchange (Figure 2.5), the volumes indicate the total size of BSE-zones ($C/C_{riv} > 0.25$) created along the 100-km distance. The BSE-zone volumes are larger than the fluid flux volumes because the fluid only occupies a fraction of the subsurface area (recall porosity n=0.3), and additionally the volume accounts for pore fluid concentrations that are $C/C_{riv} > 0.25$. The cumulative BSE-zone volumes range from 1.8×10^5 m^3 to 4.6×10^6 m^3 and are also presented as an equivalent volume of Olympic swimming pools. A notable difference is that the BSE zone volumes span a smaller range than volumetric BSE fluxes. For comparison, the largest and smallest cumulative BSE-zone volumes differ by a factor of 25, while the largest and smallest fluid flux volumes differ by a factor of 100.

2.3.4 Longitudinal Results: Negative Groundwater Head Gradient

2.3.4.1 BSE Volume Under Negative Groundwater Head Gradient

We modeled the full suite of dam scenarios under a losing head gradient of -0.0075 to test how the dam release interact with losing groundwater conditions. For comparison to losses under steady-state conditions, the volumetric flow into the bank under steady losing conditions is shown as a gray line, while the three sizes of dam releases are show as blue (0.5 m), black (1 m), and green (1.5 m). Not surprisingly, the dam releases cause more flow into the bank over 24 hours than steady state losing conditions. The amount of additional volumetric flux into the bank ranges from as small as a 40% increase for the 0.5 m peak release to as large as a 600-700% increase for the 1.5 m square release. Another important feature is the slow decay rate of the volumetric flux. Volumetric fluxes at 100 km downstream from the dam are still 80-100% of the value immediately downstream from the dam.

Time series of instantaneous flux across the river-bank interface (Figure 2.7 c-d) and cumulative flux into the bank (Figure 2.7 e-f) offer additional insight about how the dam releases interact with a bank that has negative head gradients. To show spatial changes in BSE with longitudinal distance from the dam we present the fluid flux (Figure 2.7 c-d) and cumulative flux (Figure 2.7 e-f) into the bank at 8 km, 48 km, and 100 km downstream. Fluid flux rate and the cumulative flux into the bank, or the integral of the flux rate, show the temporal response of the inflow of river water into the bank. The sign convention for the flux rate is negative values are flow into the bank while positive values are flow into the river. The fluid flux rates and cumulative flux into the bank show that the dam releases temporarily cause large increases in losses from the river into the bank. This can be seen where the flux rate has large negative values and where the cumulative inflow plots increase much more rapidly than the constant slope of the steady losing condition. A difference between peak and square releases is that the magnitude of losing flux rate decreases much more for peak than square releases. While there is a large reduction in losing flux rate for the peak releases, there is not a large change in the cumulative amount of flow into the bank with distance downstream – seen by the near horizontal shape of the cumulative flux vs distance plots (Figure 2.7a). The other important difference between the peak and square dam releases is that the square dam releases result in prolonged periods of return flow where some of the water that flowed into the bank during the rising limb of the dam releases flows back into the river during the stage recession.

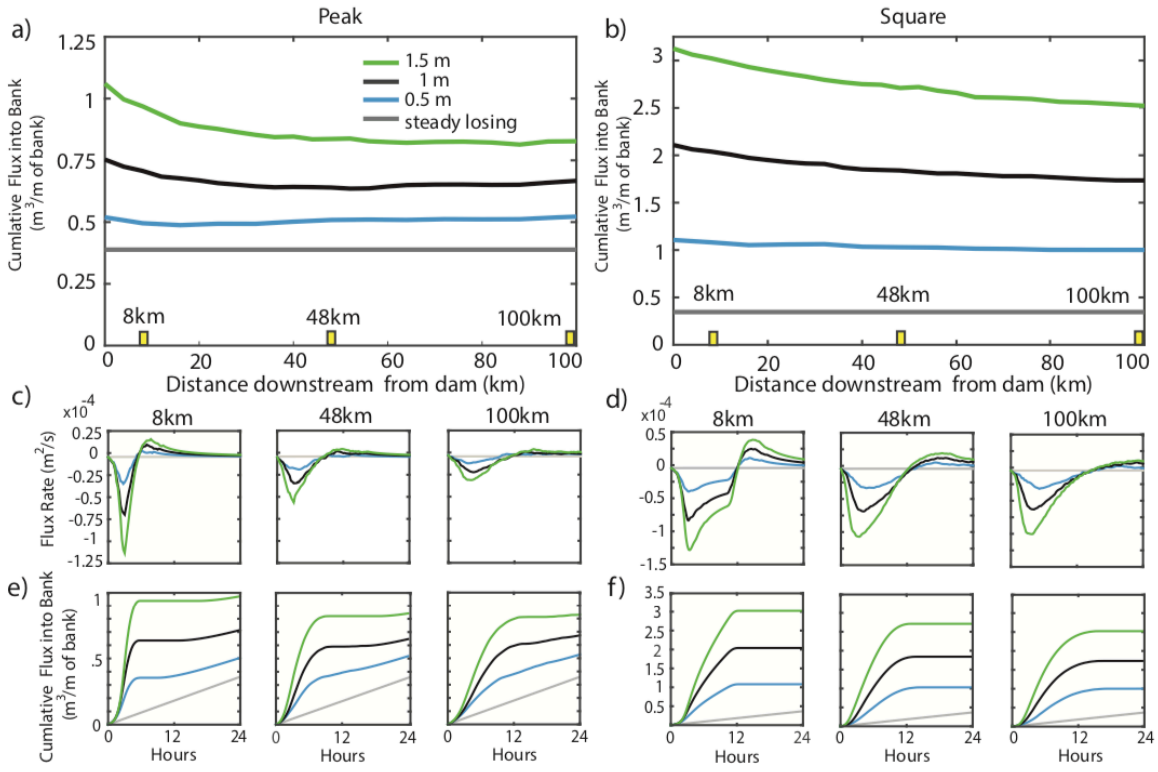

Figure 2.7: BSE flux under losing groundwater flow

Cumulative volumetric BSE-flux under losing conditions (ambient groundwater gradient = -0.0075) for peak (a) and square (b) dam releases. The amount of water lost from the river into the banks if there were no dam releases is shown for comparison (grey). The smaller subplots (c and d) show time series of both cumulative volumetric flow into the bank and also instantaneous flowrate at 8, 48, and 100 km downstream from the dam. As in 7a and 7b, the cumulative volumetric flow and instantaneous flow rate for the losing condition with no dam releases is shown in grey.

Square releases (Figure 2.7d) create temporary gaining conditions in what would otherwise be a losing river. The periods of return flow can be seen where the flux rates have positive values and the cumulative flux volumes have a horizontal slope. Our results show that for all sizes of square releases, losing conditions have not resumed after 24 hours since the arrival of the dam release – evidenced by the flat cumulative fluxes for the square scenarios. In contrast, all but the largest (1.5 m) peak release show a return to losing conditions after 24 hours.

2.3.4.2 Solute Area Under Losing Groundwater Flow Conditions

Time series of solute area in the bank were calculated for the different dam release scenarios under losing groundwater flow conditions. The baseline comparison for these cases is the area of solute that would have formed under steady state losing conditions with a constant ambient head gradient of -0.0075. Figure 2.8 shows the growth in the size of the solute area for each dam release scenario and the steady-state size for comparison in light gray. For all cases, the hydropeaking dam releases create larger BSE-zone areas than the baseline steady losing conditions. Areas for the peak pulses ranged from 1.15-1.6 times larger than under no dam releases and 1.74-3.33 times larger for square releases. The difference in cumulative BSE-zone areas between losing and neutral groundwater conditions was largest for the smallest 0.5 m magnitude releases, became smaller as the dam release magnitude increased, and was more significant for peak than for square releases. For comparison, cumulative BSE zone areas for losing conditions compared to neutral conditions were 70%, 30%, and 18% larger for peak releases and 17%, 10%, and 7% larger for square releases for the release magnitudes of 0.5 m, 1 m, and 1.5 m.

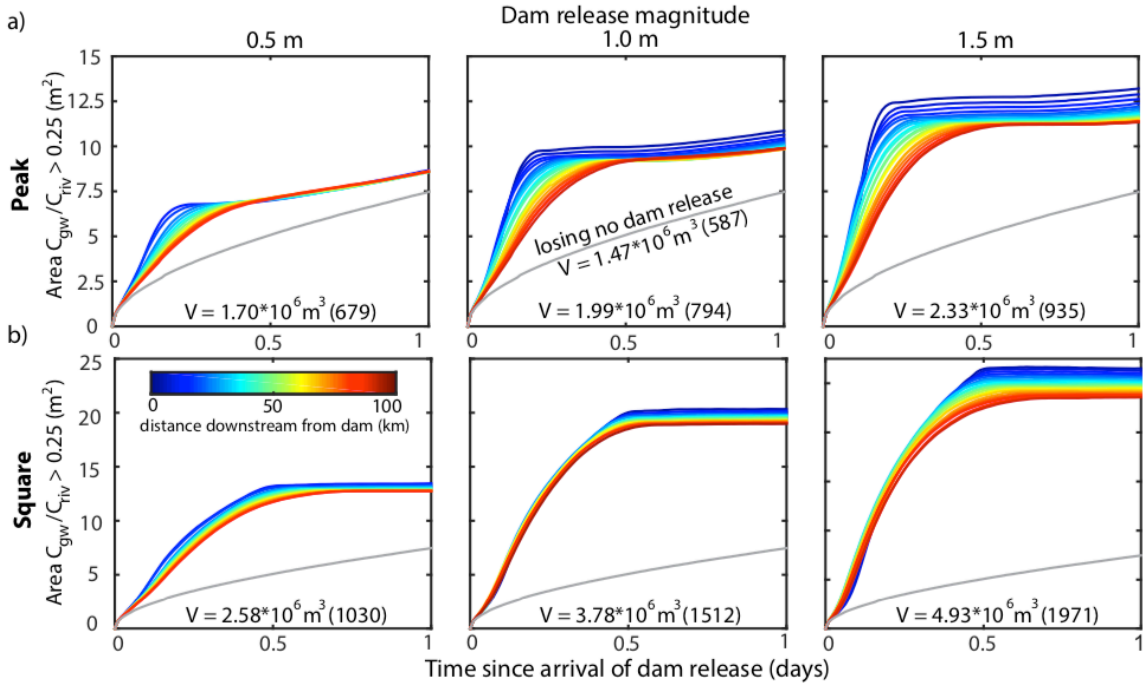

Figure 2.8: Time series of BSE-zone area under losing groundwater flow conditions

Summary of solute transport from the river into the riverbank for three magnitudes of peak (a) and square (b) dam release types under a losing groundwater gradient (-0.0075). The area that would result from steady losing conditions is shown in gray. The volume bank zone that had C > 0.25 for the 100-km length of river is listed in cubic meters and Olympic swimming pools.

2.3.5 Longitudinal Results: Varied Channel Roughness and Slope

Two channel properties that control the propagation of a flood pulse downstream are channel slope and roughness. To test the effects of these two parameters we routed a 1 m peak release for a channel twice as steep as the one used for this study (Figure 2.9) and for two different roughness values (Figure 2.10). A neutral ambient groundwater condition was used for these scenarios.

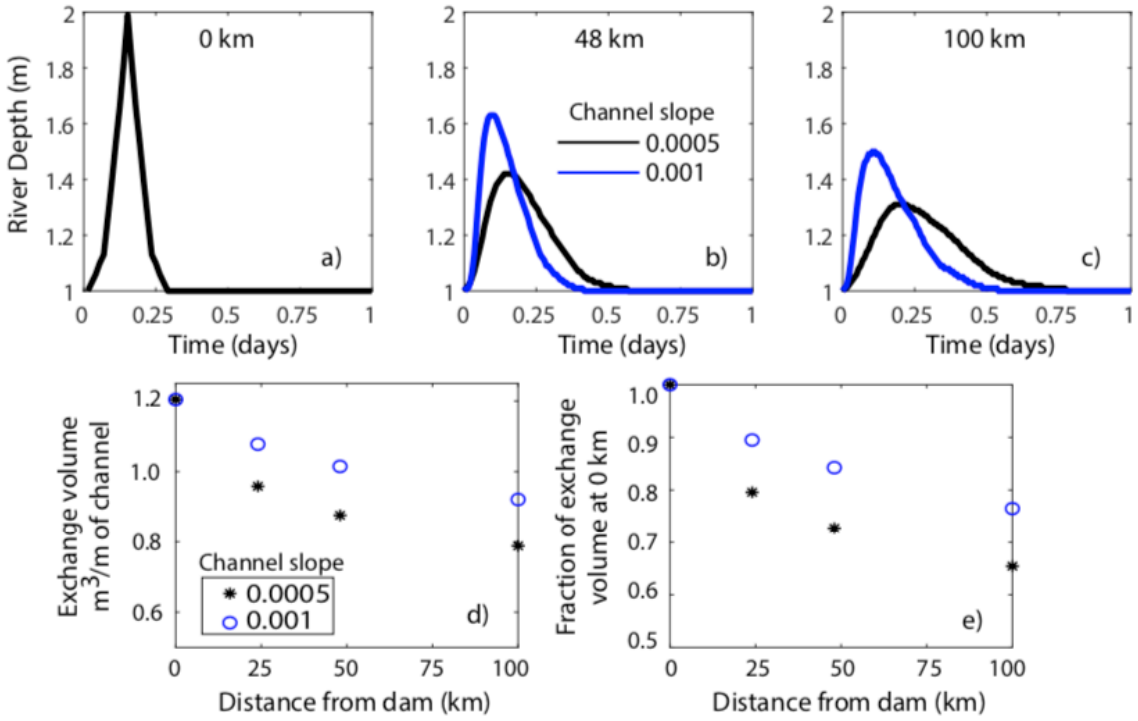

Figure 2.9: Effect of channel slope on longitudinal attenuation of dam release and volumetric exchange at 25, 50, and 100 km.

River stage response at 48 km (b) and 100 km (c) downstream due to a 1 m peak release for channel slopes of 0.0005 (blue) and 0.001 (black). Inflow volume per meter of channel (d) and fraction of initial exchange volume (i.e. decay in exchange volume with longitudinal distance) shown in (e).

Steepening the channel slope reduced the amount of attenuation of the flood pulse. The flood pulse height for the 2x-steeper channel was 50% (0.21 m) larger at 48 km downstream and 61% (0.19 m) larger at 100 km downstream. Less attenuation also resulted in the flood pulses having shorter wavelengths. The larger, less attenuated flood pulses due to the steeper channel resulted in larger volumetric inflow into the bank along the 100 km river segment (Figure 2.9d). In addition to having larger quantities of bank storage inflow, there was less decay in the amount of inflow for the steeper channel (Figure 2.9e). The decay in exchange volume is shown as the fraction of volumetric

exchange at a given longitudinal distance compared to the initial amount at the dam (0 km). At 100 km from the dam, the exchange volume for the steeper channel is 76% of the initial amount, while for the original channel slope of 0.0005 the exchange volume is 65% of the initial amount.

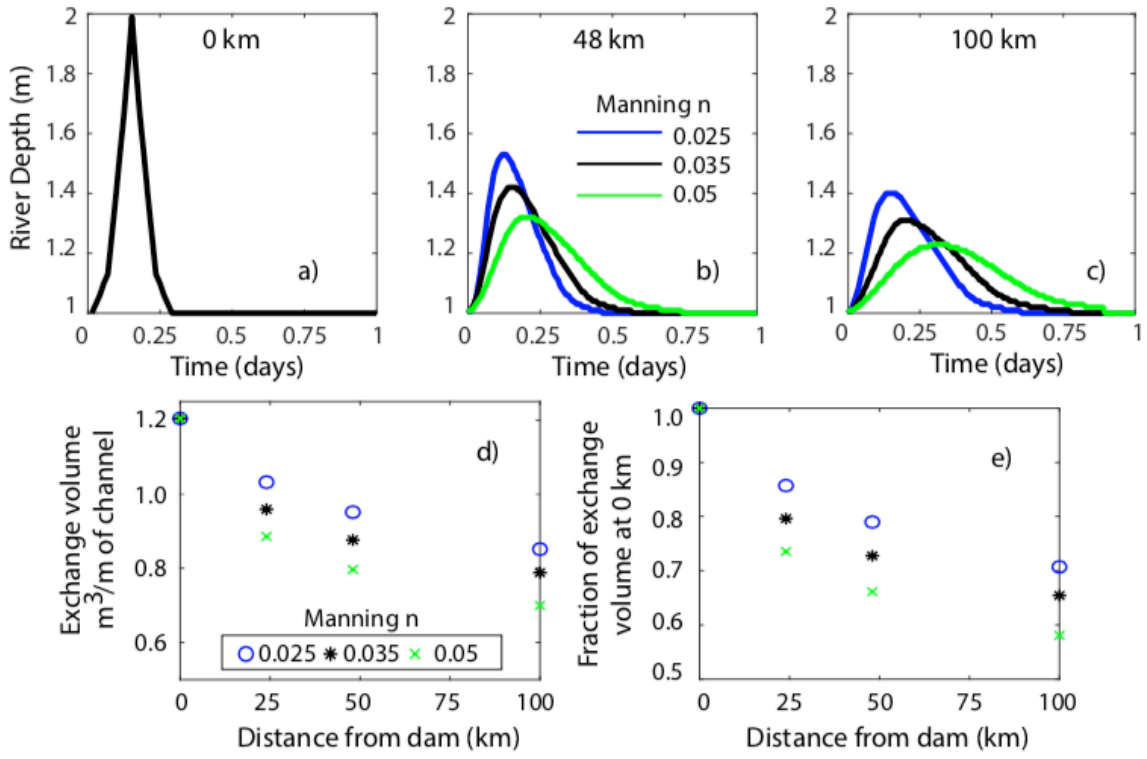

Figure 2.10: Effect of channel roughness on longitudinal attenuation of dam release and volumetric exchange at 25, 50, and 100 km.

River stage response at 48 km (b) and 100 km(c) downstream due to a 1 m peak release for three roughness values: 0.025, 0.035, and 0.05. Inflow volume per meter of channel shown in (d) and fraction of initial exchange volume (i.e. decay in exchange volume with longitudinal distance) shown in (e).

Increasing the roughness caused greater attenuation of the dam release signal. The resulting flood pulse hydrographs at longitudinal distances of 48 km and 100 km for channel roughness values of 0.025, 0.035, and 0.05 at are shown in Figure 2.10. At 48 km

downstream, an increase in roughness from 0.025 to 0.035 caused the flood pulse to be reduced from 0.5 m to 0.42 m (16% decrease), and for the highest roughness value of 0.05 the height is 0.32 m (36% decrease). The same approximate differences in flood pulse height for the three roughness values are present at 100 km. As was found in the channel slope comparison, the more attenuated flood pulses cause both less total volumetric exchange (Figure 2.10d) and a more rapid decay of exchange with distance (Figure 2.10e).

2.3.6 Longitudinal Results: Varied Hydraulic Conductivity

To test the effect of hydraulic conductivity on longitudinal BSE exchange, we compared longitudinal volumetric BSE for three *K* values: 1 m/day, 10 m/day (rest of this study), and 50 m/day. As expected, the results of the varied K simulations for 1 m peak and square releases and three ambient groundwater flow conditions (neutral, 0.0075, 0.015) showed increases in K resulted in larger volumetric exchange (Figure 2.11). The exception was beyond ~40 km for the peak release with the 0.015 gradient.

The first set of comparisons that can be made are to examine the effect of different hydraulic conductivities and ambient groundwater head gradients at a fixed location. For this comparison exchange volume at the dam (0 km) are used. At this location the volumetric exchange per meter of channel for K = 1 m/day ranged from 0.21-0.25 m^3 for peak and 0.74-0.86 m^3 for square, for K = 10 m/day the range was 0.84-1.2 m^3 for peak and 2.74-3.76 m^3 for square, and for K = 50 m/day the range was 1.78-3.2 m^3 for peak and 4.6-9.3 m^3 for square (Figure 2.11 a-b). From these values, it can be seen

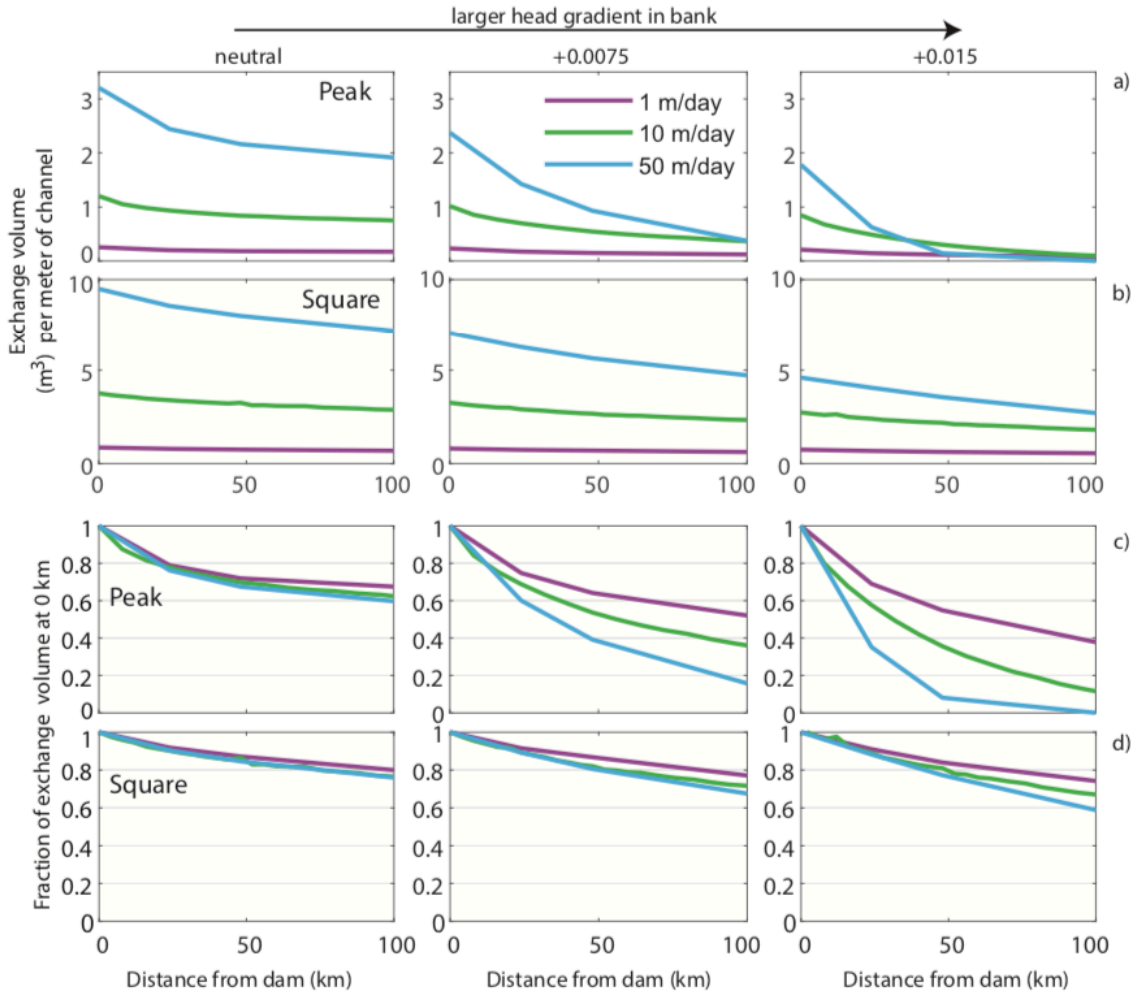

Figure 2.11: Effect of hydraulic conductivity on longitudinal volumetric exchange for 1 meter peak and square dam signals

Effect of hydraulic conductivity (K) on longitudinal volumetric exchange flux for 1 m peak (a) and square (b) releases. Three K values were modeled: 1 (purple), 10 (green), and 50 m/day (blue). Besides absolute volumetric exchange (m^3), the fraction of exchange volume at 0 km (largest exchange) with longitudinal distance is shown in subplots c and d. The BSE flux as a fraction of exchange shows how K affects the longitudinal distribution of exchange flux.

that higher hydraulic conductivity results in larger volumes of exchange and a larger range in exchange volume depending on groundwater conditions. The high values are for neutral conditions and the low values are for the strongly gaining (0.015) ambient head

gradient. The percent reductions in inflow due to strongly gaining conditions for K values of 1 m/day, 10 m/day, and 50 m/day are respectively 16%/30%/44% for peak and 14%/27%/50% for square. These results show that higher K increases the limiting effect of gaining groundwater conditions.

The other set of comparisons that can be made are how hydraulic conductivity and ambient groundwater head gradients affect the longitudinal distribution of volumetric BSE. For all three K values the amount of exchange decreases with distance from the dam (Figure 2.11 a-b). The effect of K and groundwater conditions is more easily visualized by plotting as fraction of initial exchange volume (Figure 2.11 c-d) rather than the absolute volume (Figure 2.11 a-b). From Figures 2.11 c-d it can be seen that for all K values volumetric exchange for the peak release decays more rapidly than the square release. Interestingly, under neutral groundwater conditions, K does not appreciably change the decline in exchange volume with distance. Under gaining conditions K does have a significant effect on the amount of decline in exchange volume with distance from the dam. The peak type release appears much more sensitive to changes in hydraulic conductivity than the square release. For example, for the gaining ambient groundwater gradient of 0.0075 the peak release at 100 km is 52% of the initial amount for K = 1 m/day compared to only 16% for K = 50 m/day, while the square release at 100 km is 77% of the initial amount when K = 1 m/day and 67% of the initial amount when K = 50 m/day. These results support that as the ambient groundwater gradient becomes more strongly gaining, increases in K will result in more rapid longitudinal decline in inflow volume with distance downstream, and peak release are more strongly affected by changes in K than square releases.

2.4 DISCUSSION

2.4.1 Spatial Patterns of BSE in Dammed Rivers

The objective of this study was to evaluate how dam release properties and ambient groundwater head gradient, and to a lesser degree aquifer hydraulic conductivity, affect longitudinal patterns of volumetric flux and solute exchange continuously over an extensive river segment during a flood pulse cycle. We found decreasing volumes of fluid exchange and smaller spatial extent of solute infiltration into the bank with increasing distance from the dam. While this finding is not surprising, our results show that even 100 km downstream and under groundwater conditions that limit flow from the river into the bank (neutral and gaining), there can be volumetric exchanges that are still 52-79% of the amount near the dam for square releases and from 0-61% for peak releases. This same comparison can be made for solute area for neutral and gaining conditions (BSE zone size), which had BSE-zone areas at 100 km downstream ranging from 74-85% of the upstream area for square releases and 0.04-73% for peak releases. The subset of simulations where K values of 1 m day and 50 m/day also had large percentages of the initial exchange volume existing over the 100 km distance, suggesting that for at least this range of K values the same general patterns seen in our full set of analyses is present. However, these simulations did suggest that at large K values the limiting effect of ambient gaining groundwater gradients can reduce or eliminate exchange. This idea is supported by *Welch et al*. (2015) who showed that banks composed of high K sediment with steep water tables can completely limit bank storage exchange.

The study results show that larger volumetric exchange leads to the formation of larger BSE zones – i.e., hyporheic zones in the bank. Modeling by *Gu et al*. (2008) and *Gu et al*. (2012) showed that BSE induced by flood events increases biogeochemical

processing in riverbanks because they create a larger area over which reactions can take place and also increase the residence time of infiltrated river water. *Gu et al*. (2012) used a multicomponent reactive transport model to explore controls on riparian denitrification. They found that the net hyporheic processing of nitrate following river stage fluctuations was best predicted by the volume of BSE, and that bank storage volume alone could explain 65% of the nitrate removal following a BSE event.

The time series of solute area (Figure 2.6) show that ambient groundwater head gradient is an important control on how rapidly solutes are flushed back toward the river from the bank. Our finding that more strongly gaining conditions lead to more rapid flushing and a corresponding reduction of BSE-zone size agrees with *Gomez-Velez et al*. (2017) who performed a non-dimensionalized analysis of the effect of water table gradient, aquifer K, and flood pulse signal on residence time distributions in a meander bend. Their study showed that low gradient water tables lead to little flushing of river sourced solute, longer residence times, and banks that contain much older water. These results agree with our finding that the BSE- zone area for neutral conditions has little reduction in size following a flood pulse. Conversely, their study showed that more strongly gaining conditions lead to more rapid flushing and shorter residence times, which also agrees with our findings.

Field estimates of BSE volumes under hydropeaking conditions are scant because it requires considerable time and resources to install monitoring wells, perform aquifer characterization, and collect the field data to make reliable BSE volume estimates. There is one hydropeaked river that such work was undertaken. At a location 13 km downstream from a hydropeaking dam that generates daily peak releases of 1.5 m, *Sawyer et al.* (2009) estimated fluid flux of 1 m^3/m of bank. This value has been noted numerous times as an example of volumetric flux that can be caused by hydropeaking

operations, but at a single location this value lacked longitudinal context. Despite the bank in our model having an order of magnitude lower K than the field location in *Sawyer et al.* (2009), our results show BSE volumes greater than or equal to their estimate over the entire 100 km river distance for all of the 1.5 m square scenarios and the 1 m square scenario for all but the strongest gaining conditions. The peak scenarios all had much smaller BSE volumes. However, we found that only for the smallest peak release (0.5 m) was BSE severely limited by gaining groundwater conditions, and all but the 0.5 m peak scenarios exhibited BSE over the entire 100 km distance. We also found that under strongly gaining conditions (ambient head gradient = +0.015), which is known to limit BSE, hydropeaking can still cause large amounts of BSE well beyond 100 km downstream – especially for 1 and 1.5 m square type releases which had BSE volumes of 0.9 to 2.23 m^3/m at the 100 km transects. These findings demonstrate the utility of a numerical modeling approach to estimate BSE fluxes compared to the labor and time intensive field estimates that can only be collected at one or a handful of locations.

A way to interpret the results of volumetric flux under the different ambient groundwater gradients (Figure 2.5) is to consider their implication for a river that experiences seasonal changes in water table configuration. Consider an alluvial aquifer that shifts from strongly gaining to less strongly gaining or even neutral conditions during a dry period. Our results show that the volume of BSE under the same dam release scenario could increase anywhere from between 5-200% for square and from 25% to greater than 600% for peak releases. Conversely, during wet periods when there is increased recharge to the aquifer, there could be comparably sizeable reductions in BSE. Thus, the importance of BSE in dammed systems could fluctuate seasonally depending on prevailing water table configuration. A similar type of interpretation can be made for a river that has spatially variable water table gradients. Our results show that a reach

significantly further downstream, but with a more gradual ambient water table gradient, could have considerably more fluid and solute exchange and larger BSE-zone than an upstream reach.

There are also likely dam-regulated rivers where losing conditions are prevalent seasonally, inter-annually during periods of drought, or spatially within a reach of a river that is locally losing but has neutral or gaining conditions at other locations along the river length. Losing conditions in dammed rivers could be natural or due groundwater pumping [*Constantz and Essaid*, 2007; *Risley et al*., 2010]. Our results support that enhanced losses from the river into a bank with losing groundwater conditions extend well beyond 100 km downstream. Unlike neutral or gaining conditions where the ambient groundwater head gradient limits the movement of surface water into the bank, in a losing river the bank constantly receives water and solutes from the river even in the absence of stage changes. We found that all sizes of square release result in much larger inputs of water into the bank compared to peak releases, and that all sizes of square releases and the largest peak release cause prolonged periods of return flow (gaining conditions) during the falling limb of the dam release. The balance between volumetric inflow during the rising limb and return flow during the falling limb controls the rate at which water will accumulate in the bank and the potential for the water table to be modified over time. Under sustained hydropeaking conditions the enhanced flow into the bank, particularly for the square type release, could cause localized replenishment of groundwater near the channel and over time, a raising of the water table towards more neutral conditions. We expect the timescales over which this would occur to vary widely depending on the dam release shape and size and aquifer hydraulic properties, with peak releases taking much longer than square releases to build up the water table near the river-aquifer boundary.

2.4.2 Lessons for Field Studies of BSE and SW-GW Interaction in Dammed Rivers and Dynamic River Environments

Most of the research on BSE, and more generally all types of SW-GW interactions, in hydropeaked rivers have been located close to the dams where stage fluctuations are largest [e.g., *Arntzen et al,* 2006, *Sawyer et al*., 2009; *Casas-Mulet et al*., 2015; *Stegen et al*., 2016; *Watson et al*., 2018; *Liu et al*., 2018]. Our findings suggest the need to extend the downstream distance over which SW-GW exchanges are evaluated in hydropeaked rivers, particularly when the type of hydropeaking operation is the square wave type, which results in large volumes of fluid flux and creates large areas of solute exchange with riverbanks well beyond 100 km downstream from the dam. Our results also support the value of monitoring water table and chemical conditions over extended time periods. This would enable field studies to capture changes in dam release properties (size and shape of dam releases) or seasonal changes in water table gradient that we have shown to have important controls on the amount of fluid and solute exchange in hydropeaked rivers.

An area of active and growing research is understanding how dynamic hydrological environments, such as a hydropeaked river, affect the functioning and types of microbial communities that inhabit river sediments [*Stegen et al*., 2016; *Graham et al*., 2017]. In its current early stages, this research is aimed at developing processes-based understanding of microbial respiration in river sediments that are subjected to frequent changes in water chemistry due to infiltration/exfiltration caused by river stage fluctuations. *Stegen et al*. (2016) performed detailed sampling of hyporheic water during daily stage fluctuations created by an upstream hydropeaking dam. They found evidence of elevated microbial metabolism in response to surface water flux into the hyporheic zone. Based on these observations, *Stegen et al.* (2016) proposed a conceptual model

hypothesizing that highly transient hyporheic exchange fluxes (daily timescales) preferentially select microbial communities with traits that are adapted to frequent changes in water chemistry and temperature. A question that our modeling begs is whether downstream changes in BSE result in a longitudinal organization of hyporheic zone microbial community sizes, diversities, and functioning. By applying the modeling approach described here, researchers can estimate how far downstream dam releases could influence fluid and solute exchange by parameterizing their model with representative river properties (width, slope, roughness, cross-section shape), aquifer properties (ambient groundwater conditions and hydraulic conductivity), and dam release hydrographs (ideally from a gauge near the dam).

2.4.3 Limitations of This Study and Recommendations for Future Work

To our knowledge this study is one of the few to integrate longitudinal and transverse analysis of flow and transport processes along a dam-impacted river corridor to analyze BSE. Necessarily, various assumptions in the modeling brought limitations. One limitation was the simplification of the channel morphology to a constant width, slope, and cross-sectional shape. Natural rivers have spatially variable slopes, widths, and depths that influence the discharge-stage relationship. Besides variations in width, depth, and slope, a natural river will have variations in bank morphology, i.e., slope. *Doble et al*. (2012) performed a sensitivity analysis of BSE fluid flux to bank slope. Their results showed that bank slope can result in up to 40% difference in volumetric exchange for a given stage fluctuation depending on whether the bank slope is gradual (more exchange) or steep (less exchange). In our modeling framework all of these parameters are held uniform, and as a result there is a monotonic decrease in exchange flux and solute area with distance from the dam. Despite these simplifications, the general trend of decreasing

BSE due to the attenuation of the dam-induced flood wave would be expected as the flood wave from the dam attenuates as it travels downstream. When interpreting our results and when selecting field locations, it should be appreciated that local channel characteristics (slope, width, depth, bank slope) can affect stage fluctuation and resulting fluid and solute exchange. Finally, advances in computing capabilities now enable sophisticated representations of river-aquifer systems such as done by *Zhou et al.* (2018) and *Shuai et al*. (2019) who both modeled hyporheic exchange over a 7 km reach of the Columbia River that experiences daily stage fluctuations from upstream hydropeaking operations. If an investigation is focused on a single river, a tailored approach similar to *Zhou et al.* (2018) and *Shuai et al*. (2019) can be taken that incorporates complex river geometry and spatial heterogeneity of hydraulic conductivity.

Another limitation of our modeling framework is the one-way coupling between the river model in HEC-RAS and the subsurface flow modeling. This approach placed an upper limit on the hydraulic conductivity value that we could use for the alluvial aquifer because we could not use a K value that would result in BSE fluxes that would appreciably modify the shape of the flood wave (i.e. Pinder and Sauer, 1971; Hunt, 1990). BSE volumes and subsurface solute area would be much larger in coarse sand and gravel alluvial aquifers – as demonstrated by comparing the volumetric exchange from the models with K = 50 m/day compared to the K = 10 m/day results. However, our modeling of three different K values ranging from K = 1 m/day up to 50 m/day show that the resulting longitudinal spatial patterns for the two release types hold across this one-and-a half order of magnitude range in K. In the absence of repeating hydropeaking conditions, the duration of return flow from the emptying of the river bank would increase as K is reduced [*Whiting and Pomeranets*, 1997].

Because of the large number of simulations and data generated by our longitudinal approach, this study was limited in the variety of water table configurations that could be considered. Further work could be done expanding the range of water table slopes, particularly assessing BSE dynamics associated with negative (losing) conditions and how dammed rivers in arid and semiarid regions, where losing or even disconnected conditions (e.g. *Shanafield et al*., 2012) are common, interact with their banks and recharge groundwater. A potential avenue for further research for losing rivers in arid environments would be to test whether BSE can buffer river low flows during dry months, how this buffering behaves longitudinally, and the combined effect of changing climate and presence of dam regulation (e.g. *Constantz*, 2003; *Constantz and Essaid*, 2007; *Risley et al*., 2010).

Other interesting directions for future work would be to incorporate heat (e.g., *Song et al*., 2018) or reactive solute (e.g., *Gu et al*., 2012, *Shuai et al*., 2017) modeling into the transverse subsurface flow models. This would be another step towards more realistically representing the complex spatiotemporal processes in the riverbanks of hydropeaked rivers. Another important step would be to study the effects of bank storage return flows carrying heat, solute, and fluid back into the river following a dam-induced BSE event and how these return flows influence river conditions. This is an unexplored question that would help determine the ecological importance of BSE in dammed river corridors. These research directions could aid in the management of hydropeaking operations to balance power generation needs with desired ecological outcomes for rivers downstream from hydroelectric dams.

2.5 SUMMARY AND CONCLUSIONS

This study analyzes the linkage between stage fluctuations caused by hydropeaking dam releases and resulting SW-GW exchanges. We used an integrated longitudinal-transverse framework in which we (1) modeled the transient river stage response over a 100-km distance caused by different types and sizes of dam release and (2) used the resulting river stage data to parameterize a time-varying head boundary condition in 2D fluid and solute transport models that were used to simulate the resulting SW-GW interaction at various distances from the dam. We quantified both the amount of fluid exchange and the area of the bank that received solute from the river for a suite of different dam release sizes (0.5, 1.0, and 1.5 m), shapes (peak and square), and ambient groundwater conditions (head gradients of -0.0075, 0.0, 0.0075, and 0.015). Additionally, to explore the influence of K on longitudinal exchange we modeled 1 m peak and square releases for K values of 1, 10, and 50 m/day.

Our results showed that two common types of dam releases can create BSE-zones well beyond 100 km downstream of hydroelectric dams. Of the two dam release shapes that we modeled, the square type resulted in substantially larger amounts of BSE fluid and solute flux. However, we found that peak releases that are 1 m or larger can also result in sizeable quantities of BSE, especially if the groundwater flow is not strongly gaining towards the river. Gaining ambient groundwater gradients reduces volumetric exchange for both types of dam release, has a more limiting effect on smaller amplitude releases, and limits BSE for peak releases more than square releases. Hydraulic conductivity was found to amplify the limiting effect of gaining groundwater conditions. Higher K values cause more rapid decay of exchange volume with longitudinal distance under gaining conditions, and the effect of K is more substantial for peak releases.

Tracking river-sourced solute in the subsurface enabled quantifying how different dam release scenarios (shape and size) and ambient groundwater flow conditions interact to control both the size (area) of the subsurface area that receives solute from the river as a result of a dam release, and also how that area persists after the stage returns to pre-dam release condition. For the simulations with neutral and gaining ambient groundwater flow conditions, we found cumulative (over the 100-km distance) volumetric exchange flux with the bank to range from 4×10^3 - 4.9×10^5 m^3 and the size of the BSE-zone volumes created along the 100-km river length ranged from of 1.8×10^5 - 4.6×10^6 m^3 depending on the dam signal shape and size. All dam releases scenarios under losing river conditions caused larger volumetric flux into the bank than steady losing conditions and created a larger subsurface area of river-sourced solute than steady state losing conditions. Time series of fluid flux rates under losing conditions revealed that square releases cause strong and prolonged periods of return flow to the river during river stage recession while peak releases, because of their much smaller exchange volumes, exhibit much shorter and less intense return flow. Our results support that both types of hydropeaking will enhance recharge in losing rivers over long (>100 km) distances and increase the BSE-zone size compared to steady losing conditions.

If information about the dam release properties, ambient groundwater flow conditions, and hydraulic conductivity are available, the findings here can help predict where hydropower operations will result in relatively active or inactive surface water-groundwater exchanges via BSE. Finally, this study highlights the importance of an integrated longitudinal-transverse flow and transport analysis framework for more fully understanding coupled surface water-groundwater processes in dammed river corridors.

Chapter 3: Riverbed Temperature and Heat Transport in a Hydropeaked River

ABSTRACT

Hydropeaking, the alternating storage and release of water from reservoirs for hydropower generation, perturbs the thermal regime of many large rivers. While the effects of hydropeaking on river temperature have been long studied, impacts on the thermal regime of riverbeds remain mostly unknown. Riverbed temperature is an important control on rates of nutrient cycling and habitat suitability for benthic organisms. We used detailed observations combined with numerical flow and heat transport modeling to investigate hydropeaking's impact on the riverbed bed thermal regime in a large regulated river. The field observations were collected 12 km downstream from a dam that induces large daily flow variations. Vertical thermistor arrays were used to collected high-resolution data of riverbed temperatures across the entire channel. Near the bank, the riverbed was highly dynamic thermally, transitioning between river and groundwater temperatures over daily flood cycles. In contrast, the rest of the riverbed was similar in temperature to the river and had relatively stable temperatures. Numerical models showed that the temperatures near the bank are explained by advective heat transport driven by the hydrostatic changes in river level, while the temperatures in the rest of the channel can be explained by hyporheic exchange typical in river bedforms. Gaining groundwater conditions and high sediment hydraulic conductivity favor thermally dynamic zones near river banks, while low hydraulic conductivity and/or less gaining groundwater conditions result in muted temperature

fluctuations. These patterns help predict thermally sensitive processes in the riverbeds of hydropeaked or flooding rivers.

3.1 INTRODUCTION

Dam regulation has altered the thermal regimes of many rivers (Steel and Lange, 2007; Ling et al., 2017). It is well understood and documented that dam operations influence downstream river temperatures over a range of spatial and temporal scales. Factors such as dam size (thermal mass of reservoir) (Johnson et al., 2004), type of release (hypolimnetic vs. epilimnetic) (Olden and Naiman, 2010), discharge management practices (Wright et al., 2009), and the size and timing of releases (Carron and Rajaram, 2001) control how downstream temperatures are altered. Studies such as those listed above are often motivated by the desire to better predict ecological consequences of dam regulation on river ecosystems. The recognition of the strong linkage between temperature and ecological health in aquatic ecosystems (Olden and Naiman, 2010) has influenced regulation and management practices such as thermal maximum daily loads from dams into receiving waters (Hester and Doyle, 2011).

Much less studied, but potentially of significant ecological importance, is how dam operations alter the thermal regime not of the river but of the underlying river sediments. Dam operations have been shown to increase the connectivity between rivers and their adjoining sediments (Sawyer et al., 2009), which enhances the exchange of heat between rivers and their underlying sediments (Gerecht et al., 2011). River sediments teem with both macroscopic (Covich et al., 1999) and microscopic life (Zeglin, 2015) and are also an important habitat for fish nests and larvae. Most aquatic organisms are sensitive to temperature, with temperature affecting biological processes ranging from

growth rate (Reynolds and Benke, 2005) to reproduction (Secor and Houde, 1995). In addition to potentially altering the habitability of riverbed sediments, changes to riverbed temperature may affect the energy balance of rivers in a substantive way because of the thermal coupling between the river and riverbed (Neilson et al., 2010).

Temperature is a key environmental control on the distribution and abundance of species spanning from microbial communities (Zeglin, 2015) to fish and to invertebrates (Ward et al., 1998) because most aquatic organisms are ectotherms, meaning that their body temperatures vary directly with ambient water temperature (Giller and Malmqvist, 1998). Ectotherms cannot regulate their body temperature and are adapted to live within the specific temperature ranges of their native environments. An organism's sensitivity to temperature is represented quantitatively by thermal performance curves, which describe how temperature influences rates of growth, development, and reproduction (Hester and Doyle, 2011). Many species can survive outside of their optimal range but their growth rates and reproduction will be diminished and their susceptibility to predation increased (Carveth et al., 2007). Therefore, alterations to the river or riverbed thermal regime could affect a multitude of aquatic species that comprise the complex food-webs of river ecosystems.

The temperature of aquatic environments also influences nutrient cycling and productivity (Poole and Berman, 2001). It has been shown that there is a general monotonic relationship between temperature and metabolic rate, with higher temperatures typically leading to higher metabolic activity (Clarke, 2006). Changes in temperature are likely to influence the metabolic rates of aquatic organisms and the net ecosystem respiration of a river environment (Young et al., 2008). Additionally, many ecologically important biogeochemical reactions such as carbon (Comer-Warner et al., 2018), nitrogen (Zheng et al., 2016), and phosphorous (Vervier et al., 2009) cycling are sensitive to

temperature. Given the relationship between gas solubility and temperature, temperature variability also affects chemical speciation and redox processes and their associated metabolic processes.

3.2 Background and Objectives

3.2.1 Previous Work on the Effect of Hydropower Operations on Riverbed Temperature

Hydropower dams are a specific subset of dams that create flow conditions that enhance the connectivity between rivers and their sediments. In the United States alone there are hundreds of hydropower dams that are hydropeaked, where outflow rates are increased and decreased on a daily basis in response to power demand (Bevelhimer et al., 2015). A common pattern in hydropeaked rivers is increased flows during high use periods such as afternoon and early evening periods during the summertime. Hydropeaking creates temporarily deeper and faster conditions than the background low flow state, often more than doubling and sometimes even increasing discharge by over an order of magnitude (Jones, 2014). The regular oscillation between low flow and high flow states in hydropeaked rivers creates favorable conditions for the exchange of both fluid and heat between the river and the shallow sediment in the bed and banks.

There have been few investigations related to hydropeaking's effects on the thermal regimes of riverbeds. Previous work on dams and their effects on surface-groundwater exchanges and thermal regimes of hyporheic zones in large rivers include Arntzen et al. (2006), Sawyer et al. (2009), and Gerecht et al. (2011), and Song et al. (2018). These studies have primarily been observational in nature, with Song et al. (2018) being the only one that incorporated a modeling component to enhance interpretation of

the field observations. All found that the stage changes induced by hydropeaking drive heat from the river into the riverbed. However, the spatial extent of these studies has been limited to the near-bank area of the riverbed due to the complexity and logistical difficulty of installing instrumentation further into the stream channel. Thus, there is no complete picture of how hydropeaking affects the thermal regime of riverbed hyporheic zones in the channels of large rivers.

More specifically, this study follows several studies focused on hydropeaking's effects on surface water-groundwater interactions in the Lower Colorado River near Austin, TX (i.e. Gerecht et al., 2011; Cardenas and Markowski, 2011; Watson et al., 2018). These previous studies showed that stage changes induced by hydropeaking dam operations resulted in the temporary reversal of head gradients, driving water and accompanying heat from the river into and out of the bed and bank on daily timescales. Gerecht et al. (2011) and Watson et al. (2018) both conducted temperature monitoring over multiple flooding events (both natural and dam-induced). Watson et al. (2018) focused on the riparian zone within the banks, a different region of the river corridor entirely, and primarily investigated large natural floods that were not due to dam releases. The study by Gerecht et al. (2011) is very similar to this one in field methods and objectives, but it was more limited in scope. As in this study, riverbed temperatures were monitored over multiple hydropeaking-induced floods. The study showed that the stage fluctuations from hydropeaking caused the riverbed near the bank to experience much larger diel temperature fluctuations than would otherwise occur at the background low-flow state. This study extends the scope of the research significantly as Gerecht et al. focused on only the first 12 m of one riverbank. In fact, it was the findings from that study motivated this one; specifically, whether the dramatic temperature dynamics observed near the bank extend across the remaining 56 m of the channel.

3.2.2 Objectives

The goal of this study is to determine how hydropeaking operations affect the riverbed thermal regime in a large dam-regulated river that is subjected to frequent stage fluctuations from dam releases. The two related questions we seek to address are:

(1) How do daily stage fluctuations influence the spatial and temporal patterns in riverbed temperature?

(2) What mechanisms and physical properties are responsible for the observed riverbed temperature behavior?

To answer these questions, we gathered high-resolution riverbed temperature data using vertical 1-D profilers deployed in the shallow 50 cm of sediment across a ~70 m wide channel. We then used a 2-D fluid flow and heat transport numerical model to simulate transient fluid flow and heat transport between the river the riverbed hyporheic zone. This work led to three distinct but connected sets of results: detailed riverbed temperature data during an 8-day period in July 2017 during which the river was hydropeaked continuously, a set of model scenarios that test what mechanisms and properties control the riverbed temperature dynamics seen in the field data, and a sensitivity analysis of how sediment hydraulic conductivity and ambient groundwater flow conditions, both of which are factors known to influence the amount of surface water-groundwater exchange, control riverbed temperature dynamics.

3.3 THE STUDY SITE

The Lower Colorado River (LCR) near the City of Austin, Texas, USA, is a dam-regulated 4th order river that is managed by the Lower Colorado River Authority (LCRA). Regional studies have shown that it is a naturally gaining river with a water table configuration that favors the flow of groundwater into the river (Larkin and Sharp,

1992). The study site is situated 14 km downstream of Longhorn Dam (Figure 3.1). Longhorn Dam is the last in a series of six dams that regulate discharge along the LCR. This network of dams is used for flood prevention, power generation (295-megawatt capacity), and to provide water for over 1 million people in central Texas (LCRA Website). There is a U.S. Geological Survey (USGS) gauge 12 km upstream of the study site (2 km downstream from Longhorn Dam) that records discharge and stage every 15 minutes. The USGS National Water Information System web interface reports a watershed area of 71,500 km^2 upstream of the gauge (ID - 08158000). The gauge data shows that the river stage had daily fluctuations ranging from 1.5-2.0 m during much of the summer in 2017 when this study took place.

Longhorn Dam has an epilimnetic spillover design that empties the small, shallow Lady Bird Lake in Austin, TX. Because of this design, the water released from the dam is warm, typically ranging from 25-30 °C during the summer. Technically, the LCR downstream of Longhorn Dam is not hydropeaked since the operation of Longhorn Dam is not for hydropower generation, but rather to keep up and respond to hydropower releases from the series of upstream reservoirs and dams. Therefore, while the flood pulses that originate from Longhorn Dam are not strictly by definition hydropeaking releases, they are analogous to a hydropeaking dam with epilimnetic releases. During the summer, there is typically a 5-10 °C difference between the surface water and regional groundwater temperatures. This combination of a large temperature contrast between surface and groundwater, proximity to a dam with daily storage-release cycles, and a large catchment drainage area size makes the LCR an ideal natural laboratory for investigating the effects of hydropeaking on surface and groundwater interactions in a large river

3.4 METHODS

3.4.1 Field Instrumentation

River temperature and stage at the study site was recorded every 15 minutes by an In-Situ Aqua Troll 200 pressure and temperature logger. The temperature accuracy is ±0.1° C with a resolution of 0.01° C and the depth accuracy is ±0.175 cm (In-Situ User Manual). In-stream temperature was redundantly monitored by an Onset HOBO Water Temp Pro v2 with an accuracy of ±0.2°C installed in the center of the channel logging at 5-minute intervals. These temperature and pressure data were used for both field data analysis and as boundary conditions for numerical modeling of streambed temperature dynamics.

The temperature data for this study was collected using custom-built vertical temperature profilers. The thermal profile sensors consisted of four thermistors spaced over 50 cm, connected to a data logger (Hobo U12-008 four-channel data logger) that recorded temperature every 5 minutes. Hobo (Onset) TMC-HD6 air/water/soil thermistors were utilized, which have been used in other related studies (Gerecht et al., 2011; Watson et al., 2018) because they are reliable and cost-effective. Each of the four thermistors were attached with electrical tape to a 0.635 cm-diameter and ~60 cm length aluminum rod with thermistor tips at fixed intervals of 10, 20, 30 and 50 cm from a designated 0 cm datum. A total of twenty-four vertical profilers were used in this study. TMC-HD6 temperature sensors have a measurement range of -40 to 50 °C in water with an accuracy of ±0.25°C from 0° to 50°C, a resolution of 0.03° at 20°C (0.05° at 68°F), and drift of <0.1°C/year. The response time of the temperature sensors is 30 seconds in stirred water (Onset TMC6-HD Sensor datasheet).

3.4.2 Study Transect Design and Installation

The large size of the channel (68 m in width) and rapid daily changes in flow (and stage) due to hydropeaking made data collection technically and logistically challenging. Two significant challenges included installing the temperature profilers and their cables securely enough that they would not be damaged during high flow periods, and the small time-windows when daylight and flow conditions allowed for safe working conditions in the river. Deploying instrumentation across the entire channel width required low-profile design to ensure there was no obstruction of navigability or loss of instruments and data due to debris moving downstream during hydropeaking releases. The time limitations on deployment required us to pre-fabricate temperature array groups that could be efficiently fixed to the bottom of the river before the steep daily stage increases around 12 pm. We grouped twenty-four vertical profilers into six temperature arrays. A two-person team using snorkels and diving weights deployed the temperature profilers. Once installed, the data loggers for each group were bundled together and held in place on T-posts driven into the streambed. The T-posts and the loggers were kept as close as possible to the bed. The wires that connected the sensors to the loggers were taped together and placed on the bed or pushed slightly into the bed and were fixed to the riverbed with tent stakes.

The vertical profiles (Figure 3.1) were spaced 2.75 m apart. Three of the profiles (shown at approximately 49 m, 56 m, and 58 m) could not be driven to the desired depth due the presence of a hard clay layer; the sensor tips at these locations were instead at 0, 10, and 30 cm depths. The precise locations of each profile were surveyed using a Sokkia Set 610 with an accuracy of 1 mm (*SOKKIA Series 10 Operator's Manual*, 2001).

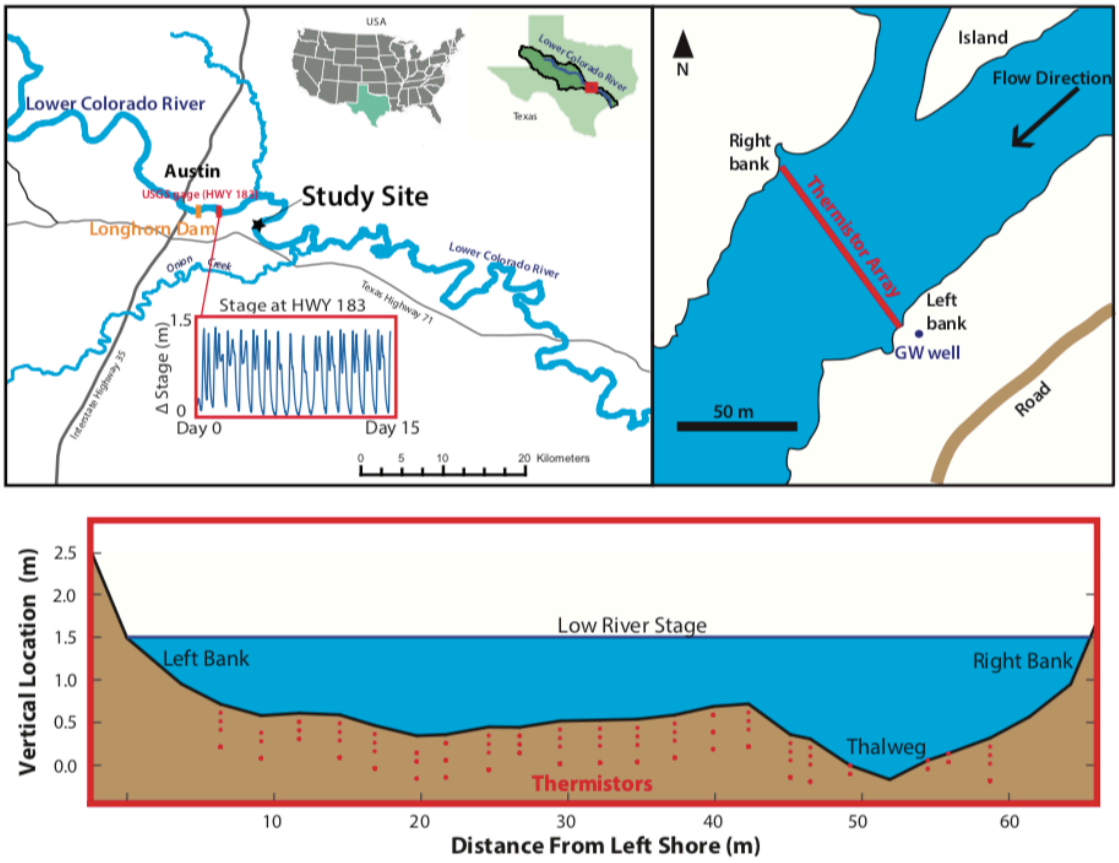

Figure 3.1: Study site location and field instrumentation

Regional map (left) with location of the study site and close up diagram of the study cross-channel (red) and along-bank (blue) sections (right). The top left figure shows an inset of the stage hydrograph from a gaging station upstream of the study site. The figure is modified after Watson et al. (2018). The lower diagram shows the field instrumentation setup with locations of thermistors (red dots) for the cross-channel transect. The vertical scale is at 27 times exaggeration.

3.4.3 Data Processing

Minimal data processing was required for the temperature data. A small number of the temperature sensors recorded inaccurate data, which were caused from damage to the sensors or cables during the installation. The data from these sensors were omitted. There were also a few instances where sensors that recorded accurate data had brief

spikes in the temperature data. These erroneous measurements were uncommon, easy to identify, and filtered out manually. The temperature data were visualized and analyzed using MathWorks Matlab to grid, interpolate, and plot the data. For visualization purposes, a median filter was utilized (Matlab function *medfilt1*) to smooth out noise. A linear interpolation was utilized to interpolate temperatures between measured points.

3.4.4 Numerical Fluid Flow and Heat Transport Modeling

3.4.4.1 Modeling Approach

A series of modeling scenarios was developed to test controls on streambed temperature to develop a mechanistic, process-based interpretation of the temperature dynamics observed at the study site. The three controls tested by our modeling scenarios included: (1) the enhanced movement of heat into the riverbed due to bedform-driven hyporheic exchange, (2) the effect of sediment hydraulic conductivity, and (3) the role of ambient groundwater head gradient in the bank. We used the finite element modeling software COMSOL Multiphysics to simulate subsurface fluid flow and heat transport.

By necessity, our model was a two-dimensional simplification of the geometry and physical properties at the study site. The first simplification was using a trapezoidal shape for the channel (Figure 3.2b). While at first this appears to be very different from the channel profile shown in Figure 3.2, the morphology of the channel at the study site would be nearly imperceptible if the aspect ratio were plotted at a 1:1 scale; the width of the channel is 68 m and the channel surface relief is less than 1.5 m. Another simplification was treating the river channel as a half width in our model domain. This was done to reduce the computational demand, as the half-width model alone had ~80,000 elements. The river stage and temperature boundary conditions used were representative of the repeated daily hydropeaking at the study site and were taken from

the stage and temperature conditions at the study site on 7/26/2017 (Figure 3.2a). Under these boundary conditions, the river stage fluctuates daily by 1.15 m and its temperature ranges from 27.2 to 30.1 °C.

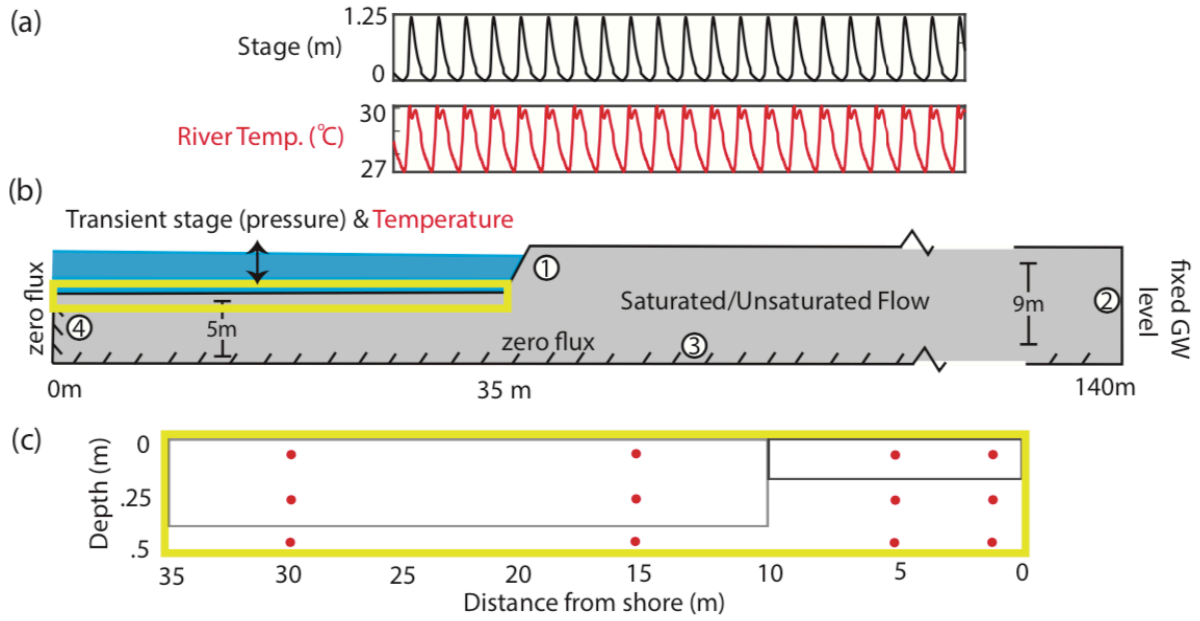

Figure 3.2: Numerical fluid flow and heat transport model design

Model domain for the fluid flow and heat transport model (b). River stage and temperature fluctuations representative of a typical day during the field data collection period were imposed along the channel boundary. The model extent is much larger than the shallow 50 cm of the riverbed where the field observations are from. This region is depicted by the yellow rectangle in (b) and a zoomed in schematic of the model parameterization for this area is shown in (c). The modeling accounted for the enhanced heat transport due to bedform-driven hyporheic exchange by assigning enhanced thermal conductivity to the upper portion of the shallow riverbed sediment.

While this study focuses only on riverbed temperatures, the model domain also included 100 m of the riverbank to allow for the lateral movement of water/heat into and out of the bank during stage fluctuations. The hydraulic connection between the bank and the riverbed controls the spatial distribution of groundwater upwelling velocities in the riverbed (Boano et al., 2009). Near-bank groundwater upwelling has been observed to be

an important factor controlling near-bank riverbed temperatures under steady state conditions (Briggs et al., 2013) and during stage fluctuations (Gerecht et al., 2011). The alluvial aquifer in our model was given a thickness of 5 m, a reasonable approximation of the aquifer thickness at the study site, which is underlain by low permeability clay at a depth of a few meters (Sawyer et al., 2009).

The domain geometry and river boundary conditions outlined above were used for all of the model scenarios. Only the physical properties of the domain (hydraulic conductivity, thermal properties, and groundwater level in the bank) were varied.

3.4.4.2 Subsurface Flow Model

Subsurface groundwater flow in our model was solved as transient variably-saturated flow. While the riverbed remains fully saturated throughout the flood pulse cycles, the emptying and filling of the bank is inherently an unsaturated flow problem, and thus we wanted to accurately represent the physics of that process. The governing equation describing unsaturated flow in porous media is:

$$\rho\left(\frac{C_m}{\rho g}+S_e S\right)\frac{\partial p}{\partial t}+\nabla\cdot\rho\left(-\frac{k_s}{\mu}k_r(\nabla p+\rho g\nabla z)\right)=Q_m \qquad (1)$$

where p is pressure [$MT^{-2}L^{-}$], ρ is fluid density [ML^{-3}], C_m is specific moisture capacity [L^{-}], S_e is effective saturation [-], S is the storage coefficient [-], k_s is the saturated hydraulic permeability [L^2], k_r is the relative permeability dependent on saturation [-], μ is the dynamic viscosity of the fluid (water) [$ML^{-}T^{-}$], z is the elevation head [L], g is gravitational acceleration [LT^{-2}], and Q_m is a stress source term that accounts for changes in total stress in the bed underneath a fluctuating river [$ML^{-3}T^{-}$].

The same boundary condition design was used for all of the modeling scenarios. No-flow boundary conditions were assigned to the aquifer base (see Boundary 1 in

Figure 3.2), which is known to be comprised of low permeability clay, and at the center of the channel which is a symmetry boundary (Boundary 2). A constant head boundary was assigned to the right-hand side of the domain (Boundary 3). The constant head boundary was used to control the ambient groundwater head gradient in the riverbank, which is the head difference between the low stage of the river and the water table elevation at the right-hand boundary divided by the 100 m distance between the right-hand boundary and edge of the channel. In all of our models the bank head gradient was positive, indicating flow towards the river. The top boundary (Boundary 4) was set as a time-varying head boundary where, at each time step, the river hydraulic head was assigned to cells at a lower elevation than the river stage. In addition to being a time-varying head boundary, the upper boundary was also set as a seepage face where cells are pervious when pressure is greater than atmospheric and no flow when pressure in less than atmospheric. Finally, the effect of rapid loading/unloading on the total stress acting on the riverbed sediment matrix was incorporated using a stress term (Q_m), as outlined in Reeves et al. (2000) and implemented in similar studies (Gardner and Wilson, 2006; Cardenas et al., 2015; Shuai et al., 2017). This effect has been shown to be important for controlling the rates and distribution of infiltration and exfiltration during rapid water surface fluctuations along the boundaries between surface water and porous media.

Hydraulic conductivity of the subsurface was specified as homogeneous for all but two of the model scenarios (outlined below), which had a lower hydraulic conductivity clogging layer in the first three meters of the streambed nearest to the bank (Figure 3.2c). A hydraulic conductivity of 100 m/day was used for the riverbed and the aquifer based on previous aquifer characterization at the study site (Sawyer et al., 2009) and grain size analysis of riverbed sediment across the temperature transect collected during the summer of 2017. The inclusion of the clogging layer was based on field

observations of a finer-grained clogging layer near the riverbank. Clogging layers have been observed in the riverbeds of other dam-regulated rivers (Siergieiev et al., 2014) and have been shown to be an important control on fluid flow across surface-water and groundwater interfaces (Doble et al., 2012). A hydraulic conductivity of 10 m/day for the clogging layer was obtained using the Hazen method based on grain size of river sediment collected at the study site. For all scenarios, K was isotropic. Porosity was assigned a constant value of 0.3, a reasonable value for sand.

3.4.4.3 Heat transport model

The riverbed temperature response to fluctuating river stage and water temperature was modeled as transient heat transport in porous media (Equation 2). The thermal properties of the subsurface are a function of the thermal properties of the fluid and solid fractions. The overall heat capacity per unit volume, ρc_m, is represented by Equation 3 and the overall thermal conductivity, κ_m, is defined by Equation 4.

$$(\rho c)_m \frac{\partial T}{\partial t} + (\rho c)_f v \cdot \nabla T = \nabla \cdot (\kappa_m \nabla T) \tag{2}$$

$$(\rho c)_m = (1-\phi)(\rho c)_s + \phi(\rho c)_f \tag{3}$$

$$\kappa_m = (1-\phi)\kappa_s + \phi\kappa_f \tag{4}$$

where ρ is density [kg/m^3], c is specific heat [J/kgK], v is fluid velocity [m/s], κ is thermal conductivity [W/mK], ϕ is porosity [-], and the subscripts m, f, s denote if a term corresponds to the porous medium (m), fluid (f), or the solid (s). The convective component v is derived from the subsurface flow model described above.

The initial condition for the heat transport model was a uniform subsurface temperature of 20 °C, which is the temperature of the groundwater end member at the study site measured from the wells in the riverbank. The river temperature was the

boundary conditions for Boundary 4 (Figure 3.2), with a condition that applied the temperature to cells below the stage of the river. While it did not affect the results of the riverbed temperature, the remaining portion of the bank surface was assigned the air temperature from a nearby weather station. Boundaries 1 and 2 were set as insulation boundaries (no heat flux). This assignment is appropriate for Boundary 1 as it is a symmetry boundary. The assignment of no heat flux to Boundary 4 is suitable for this study because the duration of our modeling scenarios only causes temperature propagation into the riverbed of less than a meter, while the lower boundary is 5 m deep. If the scenarios were longer (months), it might be necessary to extend the domain to include the underlying regional clay unit to allow the movement of heat between the alluvium of the river and the clay layer. Boundary 3 was assigned the groundwater endmember temperature as this is the source of cold, regional groundwater.

The thermal properties of the solid fraction of the domain $(1-\phi)$ were set at values for quartz with a thermal conductivity (κ_s) of 1.4 W/m-K (Yamane et al., 2002), a specific heat (c) of 700 J/kg-K, and a density (ρ) of 2,600 kg/m^3. Water was assigned a thermal conductivity (κ_f) of 0.6 W/m-K, a specific heat (c) of 4,200 J/kg-K, and a density (ρ) of 980 kg/m^3. The thermal conductivity and specific heat for a domain element was calculated as a weighted mean of the solid and fluid fraction.

An important mechanism of heat transport that we wanted to incorporate into our model was the enhancement of heat flow in the shallow riverbed sediments due to bedform-driven (hydrodynamic) hyporheic exchange. The physics in our 2-D model only accounts for hydrostatically driven fluid exchange. In order to artificially represent the enhanced movement of heat into the upper riverbed sediments by bedform-driven exchange due to hydrodynamic pressure gradients along the bed (e.g., Cardenas and Wilson, 2007a), the thermal diffusivity (α) in the shallow 10-40 cm of riverbed of the

model domain was artificially increased (Figure 3.2c). Thermal diffusivity α (m^2/s) describes rate transfer of heat through a material and is defined as the thermal conductivity κ_m divided by the volumetric heat capacity $(\rho c)_m$ (Eq. 5).

$$\alpha = \frac{\kappa_m}{(\rho c)_m} \tag{5}$$

To mimic the enhanced heat exchange caused by bedforms we increased the thermal conductivities of the liquid and solid fractions in the shallow riverbed (Figure 3.2c). From Eq. 5, it can be seen that an increase in the thermal conductivity results in an increase in the thermal diffusivity. The physical process that is represented by increasing the thermal conductivity is increasing the hyporheic heat flux – the rate that river water travels through and convects heat into the riverbed via shallow subsurface hyporheic flow paths. A similar approach was implemented by Bhaskar et al. (2012) who increased the thermal diffusivity in the upper portion of their vertical 1-D heat transport model to represent the contribution of bedform exchange to streambed temperature dynamics.

One challenge of comparing model results to our field observations is that our field observations are for a system that is inherently never at equilibrium. The streambed temperature profiles we collected in July 2017 are a composite of long-term seasonal warming of the subsurface (weeks to months) overprinted by short-term daily and sub-daily conduction and convection of heat into and out of the streambed. Model results for two different locations across the channel (1.5 and 15 m) and at three depths (10, 30, and 50 cm) illustrate these two timescales (Figure 3.3). Looking at Figure 3.3, it can be seen that the riverbed temperature increases as the much warmer river water (27-30 °C) transfers heat into the riverbed via both conduction and convection. After ~10 days the riverbed reaches a quasi-equilibrium where the magnitude of daily variability has

stabilized. After 10 days it can be seen that while the 50 cm depth is still warming slightly, the daily variability at all of the depths has stabilized. The location further into the channel (warm colors) takes considerably longer to reach equilibrium than the location near the bank (cool colors). Because we were interested in only exploring controls on temperature variability (daily range), spin up periods of 10 days were sufficient for our field-modeling comparison.

3.4.4.4 Model scenarios

The first set of model scenarios was designed to test the influence of enhanced transport of heat in the shallow riverbed sediment from bedform exchange and the control of K on shallow streambed temperature response. For all of the scenarios, the ambient groundwater head gradient in the bank was assigned a value of 0.015; a positive value indicates a gradient towards the river – i.e., gaining/upwelling groundwater conditions in the riverbed. This value is based on measured water levels from a well transect in the riverbank at the study site. We modeled eight scenarios that simulated 10 days of continuous river stage and temperature fluctuations.

Eight scenarios were run and fall into two groups (Table 3.1). Scenarios 1-5 are designed to test controls on the riverbed temperature response under conditions of daily stage fluctuations, while Scenarios 6-8 were designed to address the separate, important question of how much heat exchange between the and the hyporheic zone in the riverbed would occur in the absence of stage fluctuations. That is, how much of the observed thermal patterns are due to dam-induced stage fluctuations? To answer this question, we ran Scenarios 6-8 that had diel temperature variation but without stage fluctuations. In these scenarios we tested two different enhanced thermal diffusivities and also a case where there was no enhanced diffusivity, representing the situation where there is no

	Fluid Flow Properties		Hyporheic Zone Depth	Hyporheic Zone Thermal Properties		
Scenario	Aquifer and Sediment K [m/d]	Clogging Layer	Depth of Enhanced κ [cm]	κ_{water} [W/mK]	$\kappa_{sediment}$ [W/mK]	
1	100	N	None	N/A	N/A	dark green
2	100	N	40/20	0.9 (1.5x)	2.1 (1.5x)	teal
3	100	N	40/20	1.2 (2x)	2.8 (2x)	dark blue
4	100	Y (10 m/d)	40/20	1.2 (2x)	2.8 (2x)	light green
5	100	Y (10 m/d)	20/10	1.2 (2x)	2.8 (2x)	magenta
6	100	N	None	N/A	N/A	light green
7	100	N	40/20	0.9 (1.5x)	2.1 (1.5x)	teal
8	100	N	40/20	1.2 (2x)	2.8 (2x)	dark blue

Table 3.1: Hyporheic zone specifications for heat transport model scenarios

Parameter specifications for the eight modeling scenarios. In the hyporheic zone depth column the two numbers provided correspond to hyporheic zone depth in middle of channel followed by depth near bank. For the thermal properties, the thermal conductivity is listed and in parentheses is the number of times the value was enhanced to mimic bedform-driven hyporheic heat transport

effect of bedform-driven hyporheic exchange enhancing heat transport. The last two scenarios in the first set (4 and 5) consider the effects of a lower hydraulic conductivity clogging layer at and near the bank.

To compare the temperature responses under each scenario to the field data, we selected vertical profiles at four distances from the bank as comparison locations. The locations were chosen based on the field data, which revealed warm and stable temperatures in the majority of the channel and highly variable temperatures near the bank. Thus, two locations were in the warm and stable region (15 m and 30 m from the bank) and two were in the dynamic area near the bank (1.5 m and 5 m from the bank). At each of the model comparison locations, temperature results were extracted from three depths (10 cm, 30 cm, and 50 cm) in the streambed, which were selected to be at the same depths as field thermistor sensors.

The second set of model scenarios tested the control of bank groundwater head gradient and aquifer K on the temperature dynamics during stage fluctuations. The scenarios covered three different ranges of K that spanned one order of magnitude (100

m/d, 50 m/d, and 10 m/d) and three different water table gradients in the bank that dictated the strength of groundwater upwelling in the riverbed (0.015, 0.0075, and 0.0015). All combinations of K and water table gradient were modeled for a total of nine scenarios. We used a modeling duration of 10 days for the second set of scenarios, sufficient for capturing both longer-term warming and daily temperature fluctuations in the shallow 50 cm of the streambed (Figure 3.3).

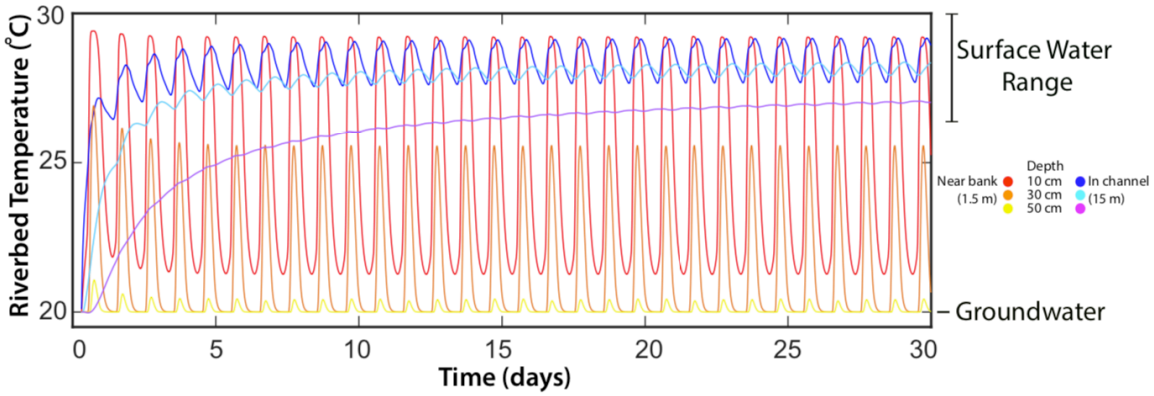

Figure 3.3: Modeled riverbed temperatures for a 30 day simulation

Example 30-day time series of simulated riverbed temperatures extracted from vertical profiles at two distances into the channel. The three depths are the same as for the field data (10 cm, 30 cm, and 50 cm). The warm-colored lines are for the near-bank area (1.5 m into the channel), while the cool-colored lines are for 15 meters from the channel. While the longer-term conductive warming takes 15-20 days to equilibrate for the 50 cm depth at the 15 m location, the daily temperature range or variability stabilizes within ~5 days.

3.5. RESULTS

3.5.1 Observed Streambed Temperature Dynamics at the Study Site

Streambed temperature data was collected over an 8-day period from 7/20-7/28 2017. During this period the river was hydropeaked continuously with daily stage fluctuations of 1-1.25 m and a temperature range of 26.9°C to 30.7 °C (Figure 3.4). Daily

water temperature highs roughly coincided with peak river stage that occurred in the late afternoon and the coldest temperatures were observed during low flow conditions that occurred in the morning.

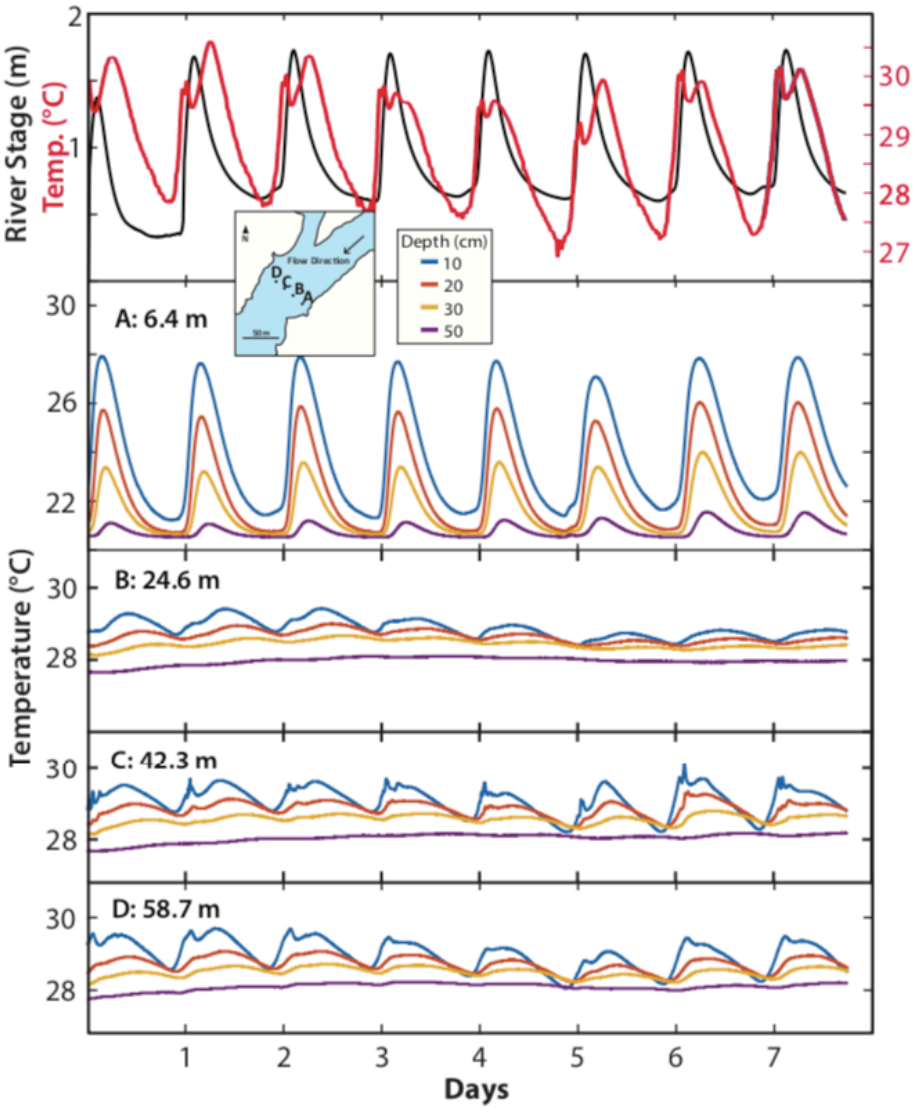

Figure 3.4: Streambed temperature data from vertical thermistor arrays

Temperature traces of select thermistor profiles from the cross-channel transect. The locations are denoted by the letter labels of each panel which correspond to the letter-labeled dots in the inset map; distances are from the left shore. The different colors correspond to different thermistor depths. The top panel shows the river stage.

The streambed temperatures appear to co-vary with changes in river temperature and stage throughout the course of the study, and showed consistent responses from day-to-day (Figure 3.4). The time series of temperature profile data at the four locations spanning the channel clearly show stage-induced daily temperature fluctuations. The streambed temperatures were all cooler than the river temperature and their fluctuations were damped with depth and distance away from the shore. At location A, nearest the bank, the thermal variability is seen at all depths, while at B, C and D a daily temperature signal was present only in the upper 30 cm of the streambed.

To concisely summarize the time series temperature data, we present daily ranges for all four sensor depths at each of the twenty-one vertical profile locations (Figure 3.5). Eight days of daily range data (difference between the maximum and minimum temperature over 24 hours) for each sensor is presented in Figure 5a. Within 12 m from the left shore, the fluctuations at all depths were higher. At locations closer than 12 m, the 10 cm depth average fluctuation is 4.10 °C with a standard deviation of 1.84 °C and at 50 cm depth the temperature fluctuates an average of 0.72 °C with a standard deviation of 0.13°C. Beyond 12 m from the left shore, the subsurface temperature ranges for all depths are similar to one another. The daily ranges at the shallow 10 cm depth were typically less than 1 °C, and deeper than 30 cm the daily ranges were typically less than 0.5 °C. The day-to-day standard deviations beyond 12 m from the left shore are less than 0.27 °C.

During low stage, in between flood peaks, colder water near the end member temperature of groundwater is pushed to the surface of the streambed at locations within 12 m of the left shore (Figures 3.5 and 3.6). The fact that the daily ranges near the shore span both the groundwater and surface water temperature ranges suggests groundwater-surface water mixing in these areas. Between 12 m and 17.5 m from the shore, there are

some intermediate temperatures, while further than 17.5 m the streambed temperatures remain consistently warm, reflecting the surface water temperature range (27-30 °C) with no temperatures in the groundwater or transitional range.

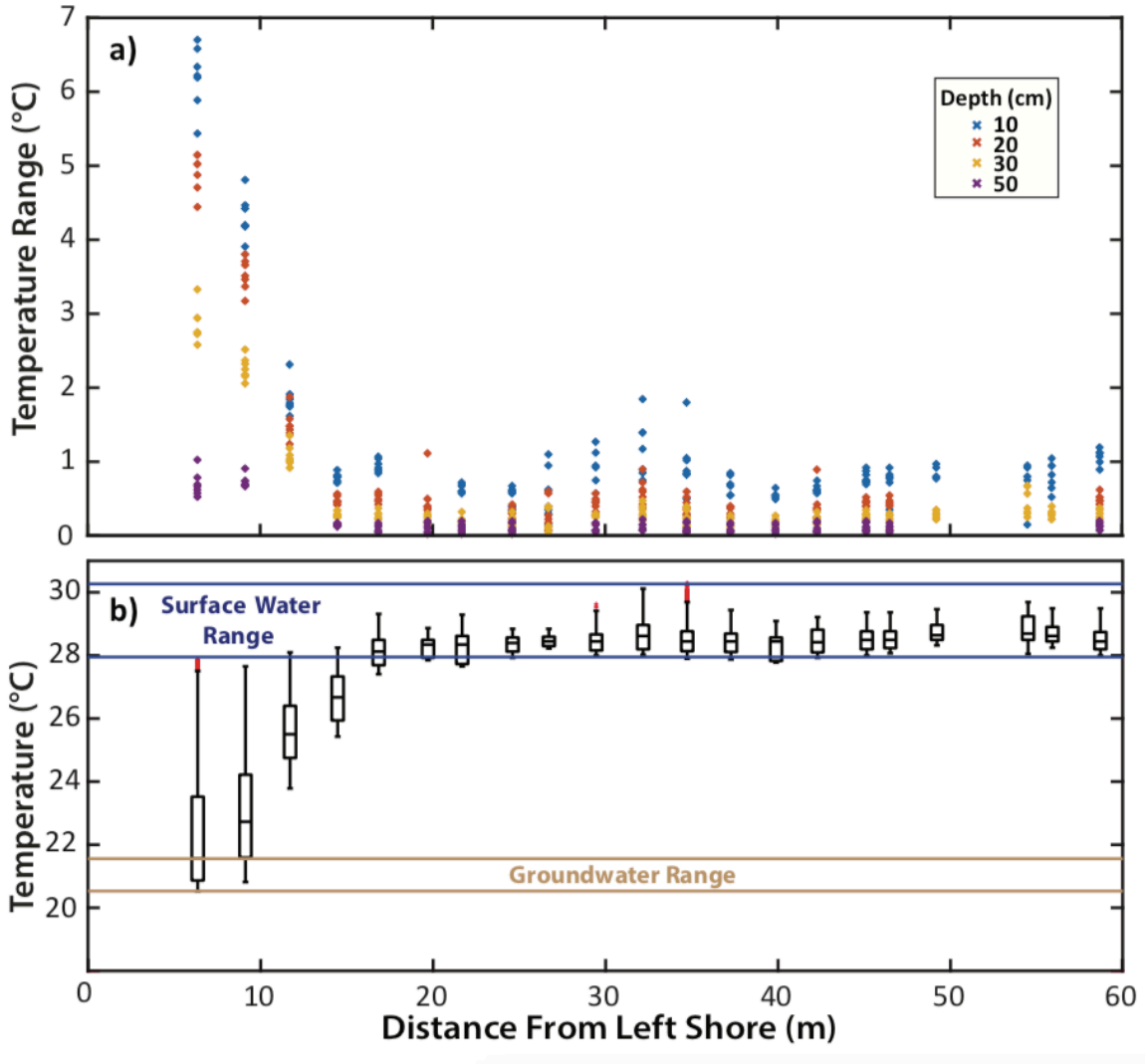

Figure 3.5: Summary plot of thermistor temperature data

Range of temperatures observed by the thermistors along the cross-channel transect. The top panel (a) shows the range (maximum-minimum) over a day at each depth (different colors). The different dots with the same colors and same distance from shore are from the same thermistor, but with the range taken over a different day (in total 5 consecutive days are shown). The bottom panel shows the box and whisker plots for all the

temperature readings put together at each distance. The midline represents the median, the edge of the box corresponds to the 25th and 75th quartiles, and the whiskers show the data extent excluding outliers which are marked by red crosses. The blue lines and brown lines in (b) denote the temperature range observed in the river and from a groundwater well in the bank.

During hydropeaking cycles, defined as low stage to high stage back to low stage, locations within 17.5 m of the left bank show subsurface temperatures respond to and experience varying proportions of the endmember temperatures (Figure 3.6). At the initiation of a flood pulse, the subsurface temperatures are similar to the background distribution of temperatures. As the flood progresses there is a rapid increase in temperatures near the bank, and soon after the flood peak, the temperatures in the monitored 50 cm-deep sediment profiles near the left bank all exhibit some influence from surface water. As the flood pulse recedes, the cooler groundwater temperatures return at the locations near the left bank. The rapid disappearance of the warm temperature signal near the bank indicates a resumption of groundwater upwelling. In contrast, the riverbed temperatures in the rest of the channel remain consistently warm throughout the entire flood pulse cycle and there are only subtle changes in sediment temperatures throughout the course of a flood pulse. Notably, the upwelling, cool signal of groundwater was absent at the right bank near the thalweg, which showed consistently warm temperatures similar to that of the channel (Figures 3.5 and 3.6). The riverbed near the right bank remained above 28 °C during the entire study period and its range never exceeded 1.3 °C/day. A physical explanation for the disparate temperature behaviors between the left and right banks is addressed by our modeling results.

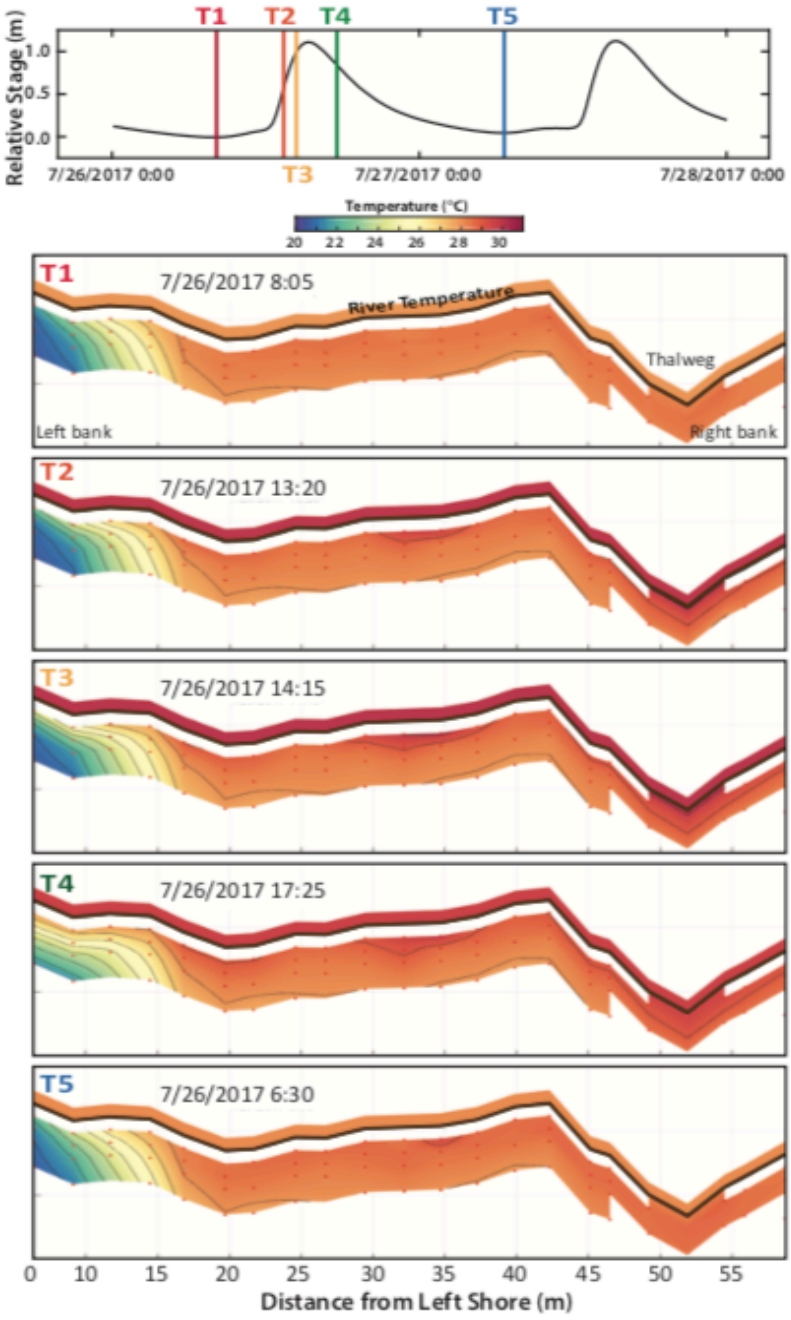

Figure 3.6: Snapshots of riverbed temperature conditions at the study site

Snapshots of temperature distribution within the cross-channel transect. The top panel shows the relative river stage with the timeline (T#) of snapshots denoted. The brown lines in the temperature fields denote the sediment-water interface with the temperature above it corresponding to the river temperature. The axis scales are not equal. The thermistors (red dots) are located at 10, 20, 30, and 50 cm below the sediment-water interface and the sediment area between 0 and 10 cm depth is blanked out.

3.5.2. Heat Transport Modeling Results

3.5.2.1 Modeling Riverbed Temperature Dynamics at the Study Site

The modeled riverbed temperatures exhibited the same general pattern as the field data, with relatively stable temperatures over most of the channel and highly dynamic temperatures near the bank. This can be seen by comparing the temperature range at the model comparison locations near the bank, located at 1.5 m and 5 m, to those of the two locations at 15 m and 30 m from the bank (Figure 3.7). Note that the goal of our modeling was not to perfectly replicate the field data by fitting parameter values (e.g., hydraulic conductivity, thermal diffusivity), but rather to elucidate the key controlling factors responsible for the riverbed temperature response observed in the field data.

The enhanced transport of heat, presumably due to bedform-driven hyporheic exchange, was a key control on reproducing temperature behavior at the locations 15 m and 30 m from the bank. This is illustrated by comparing the model scenario with no enhanced conductivity (Figure 3.7, Scenario 1) to those where thermal conductivity was enhanced to mimic the presence of bedforms (Figure 3.7, Scenarios 2-5). Without enhanced thermal conductivity, it can be seen that the thermal signal at 15 m and 30 m is both highly lagged and is of considerably smaller magnitude than the field observations (dark green vs. all other colors). The temperature response at 10 cm (Figure 3.7c and d) was almost insensitive to either the amount of increase in thermal conductivity (cyan 1.5x and dark blue 2x conductivity) or the depth of the zone of enhanced conductivity (magenta 20 cm and light green 40 cm). Changes in the thermal conductivity and depth of enhanced conduction influenced the response at the 30 cm depth (Figure 3.7g and h).

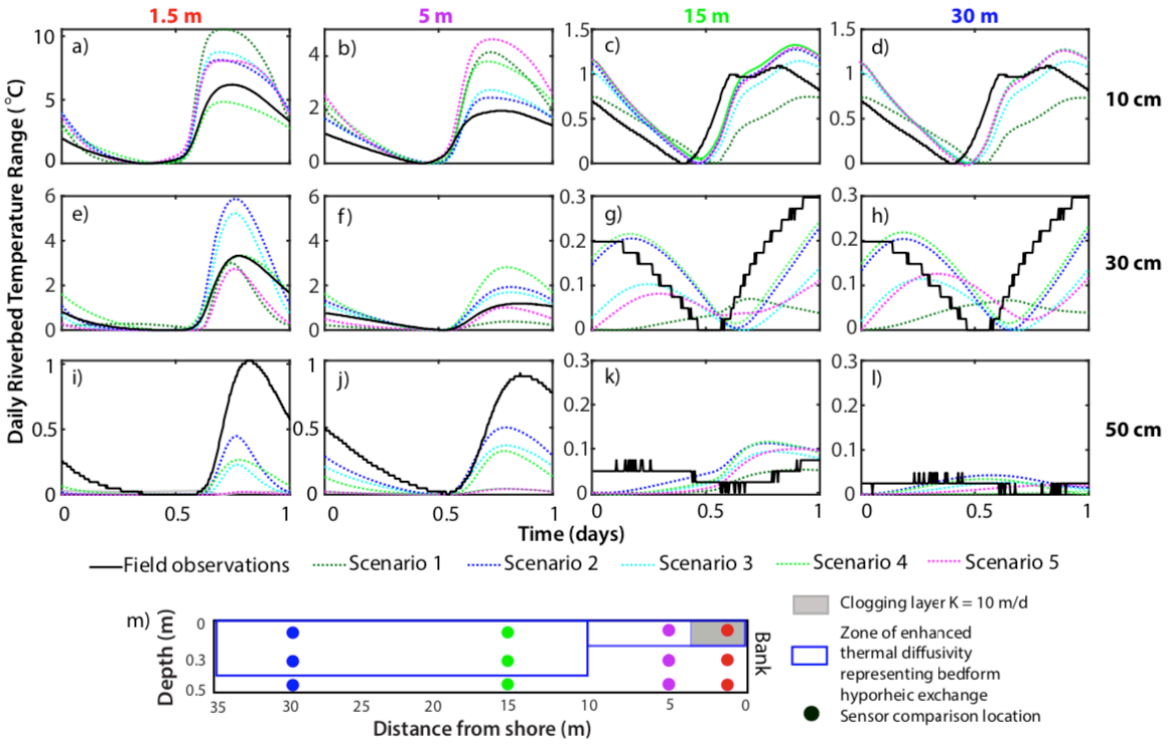

Figure 3.7: Model comparison results for scenarios 1-5

Model comparison results for Scenarios 1-5 (see Table 1 for details). The field data for each sensor is shown in black and the different model scenarios are plotted in color. The locations of each sensor in the riverbed are shown in the inset below the data, and the blue boxes in the inset show the extent of the region assigned enhanced thermal diffusivity to mimic bedform-driven exchange.

The smaller 1.5x conductivity and shallower 20 cm depth of enhanced conductivity resulted in only ~0.1 °C fluctuation compared with the ~0.23 °C for the scenarios with 2x thermal conductivity and a 40 cm enhanced conduction zone depth. The 0.23 °C daily range at 30 cm depth for Scenarios 2 and 4 were quite close to the field data, which had a range of ~ 0.3 °C. For the 50 cm depths, the temperature fluctuations were all ~0.1 °C or smaller regardless of scenario and matched the stable temperatures seen in the field data.

The two locations nearer to the bank, at 1.5 m and 5 m, were much more sensitive to the different modeling scenarios. As with the locations further from the bank, the

scenario that had no enhanced thermal conductivity (Scenario 1) least resembled the field data. Interestingly, the absence of enhanced conductivity resulted in a doubling of the temperature range at 10 cm depth compared to the field data. It had the opposite effect at the 30 cm and 50 cm depths where it resulted in much smaller temperature variability than the field data. At the 1.5 m location, Scenario 4 that included the clogging layer with lower hydraulic conductivity, closely matched the field data at 10 cm and 30 cm depth (Figures 3.7a and e). While the clogging layer was important at 1.5 m, its presence actually resulted in poorer fits at the 5 m location. The location at 5 m was best represented by Scenarios 2 and 3, which are the scenarios with a deeper zone of enhanced thermal conductivity (20 cm as opposed to 10 cm) and no clogging layer. Scenario 5, where there is a shallower zone of enhanced thermal conductivity (10 cm), produced the worst overall match with the data at the 5 m location (Figures 3.7 b, f and j). Overall, these results indicate some enhanced transport of heat from bedform exchange is occurring at these locations, and that the finer sediment near the riverbank is a key control on the temperature variability at this location.

Scenarios 6-8 show riverbed temperature response to simulations without stage fluctuations (Figure 3.8). Results from these scenarios are presented for two distances from the bank: at 1.5 m representing the region of dynamic temperatures seen in the field data and at 15 m representing the region of warm and relatively stable temperatures. The first of these scenarios, Scenario 6, has no enhanced thermal conductivity, representing a situation where heat transport into the riverbed is from conduction only. The riverbed temperatures for Scenario 6 are much more attenuated and lagged compared to the field data, and are a poor match (Figure 3.8). Scenarios 7 and 8 show that enhanced thermal diffusivity alone (bedform-driven exchange) creates a temperature response at the 15 m location comparable to that seen in the field data. Interestingly, the temperature response

at 15 m for Scenarios 7 and 8 are almost identical to those in Scenarios 2 and 3 (Figure 3.7), which have the same model settings but with 1.25 m stage fluctuations. In contrast, without stage fluctuations, the temperatures near the bank at the 1.5 m location showed almost no variability in these scenarios without stage fluctuation. For these scenarios, temperature variability for the 10 cm depth was < 0.95 °C as opposed to 6.2 °C in the field data and the temperature variability at 30 cm was < 0.15 °C compared to 3.3 °C in the field data.

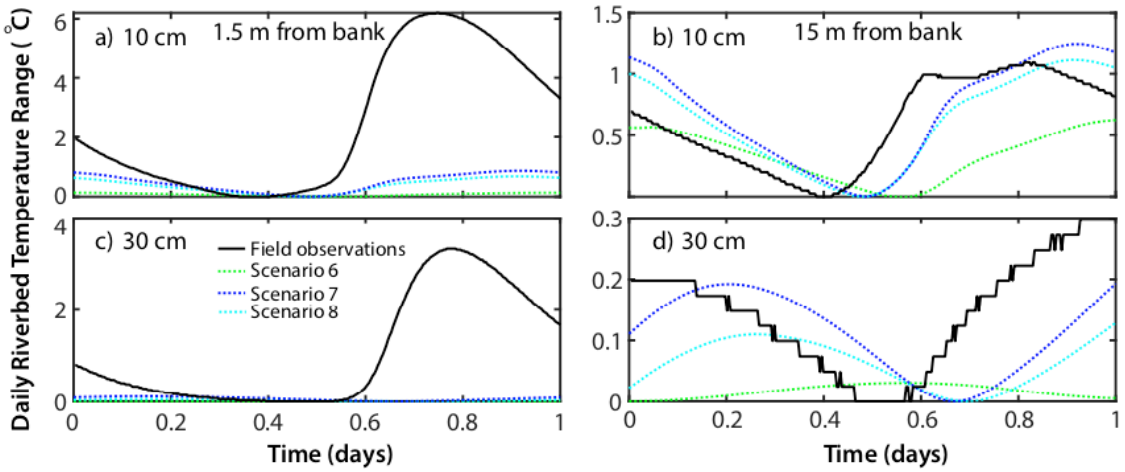

Figure 3.8: Model comparison results for scenarios 6-8

Model comparison results for Scenarios 6-8 (see Table 1 for details) where riverbed temperature dynamics were simulated without stage fluctuations. Results from two depths (10 cm and 30 cm) at two locations in the channel are shown: 1.5 meters from the bank (a & c) and 15 meters from the bank (b & d). As in Figure 7, the field data is plotted in black. These results show that the riverbed temperature near the bank is almost entirely due to stage fluctuations, while the temperatures further into the channel do not depend on the stage fluctuations at all.

3.5.2.2 Sensitivity of Riverbed Temperature to Ambient Groundwater Flow and Sediment Hydraulic Conductivity

Larger bank groundwater head gradients and higher hydraulic conductivities both favor a larger area in the riverbed where the groundwater end-member temperature is present (Figure 3.9). The control of bank head gradient and hydraulic conductivity can be seen by comparing the size of the cool groundwater endmember temperature (~20 °C) zone near the bank under the three different values of hydraulic conductivity and bank groundwater gradients (Figure 3.9). The effect of these two parameters is most apparent when comparing riverbed temperature for the high and low scenarios of hydraulic conductivity and bank groundwater gradient – i.e. where the K is 100 m/d (Figure 3.9a) and 10 m/d (Figure 3.9b) and bank head gradient is 0.015 and 0.0015. In all cases, the majority of the riverbed resembled the river temperature (27-30 °C) with the bank head gradient and hydraulic conductivity only influencing the riverbed temperatures near the bank.

In addition to controlling riverbed temperature, bank head gradient and hydraulic conductivity control the variability of riverbed temperatures during stage fluctuations. As observed in the field data, the models consistently show that the region of largest temperature variability is located near the riverbank (Figure 3.9). The variability is larger for higher hydraulic conductivities and for larger bank head gradients. For the highest hydraulic conductivity scenario of 100 m/d and highest bank head gradient of 0.015, the daily range in temperature was as large as 10 °C, representing daily fluctuation between the temperatures of the groundwater and surface water end-members. The effect of decreasing the head gradient in the bank can be seen by comparing the temperature range under the same hydraulic conductivity condition (100 m/d), but an order of magnitude

lower bank gradient (0.0015). Reducing the bank gradient by an order of magnitude halves the maximum daily temperature range to ~5 °C. Varying hydraulic conductivity

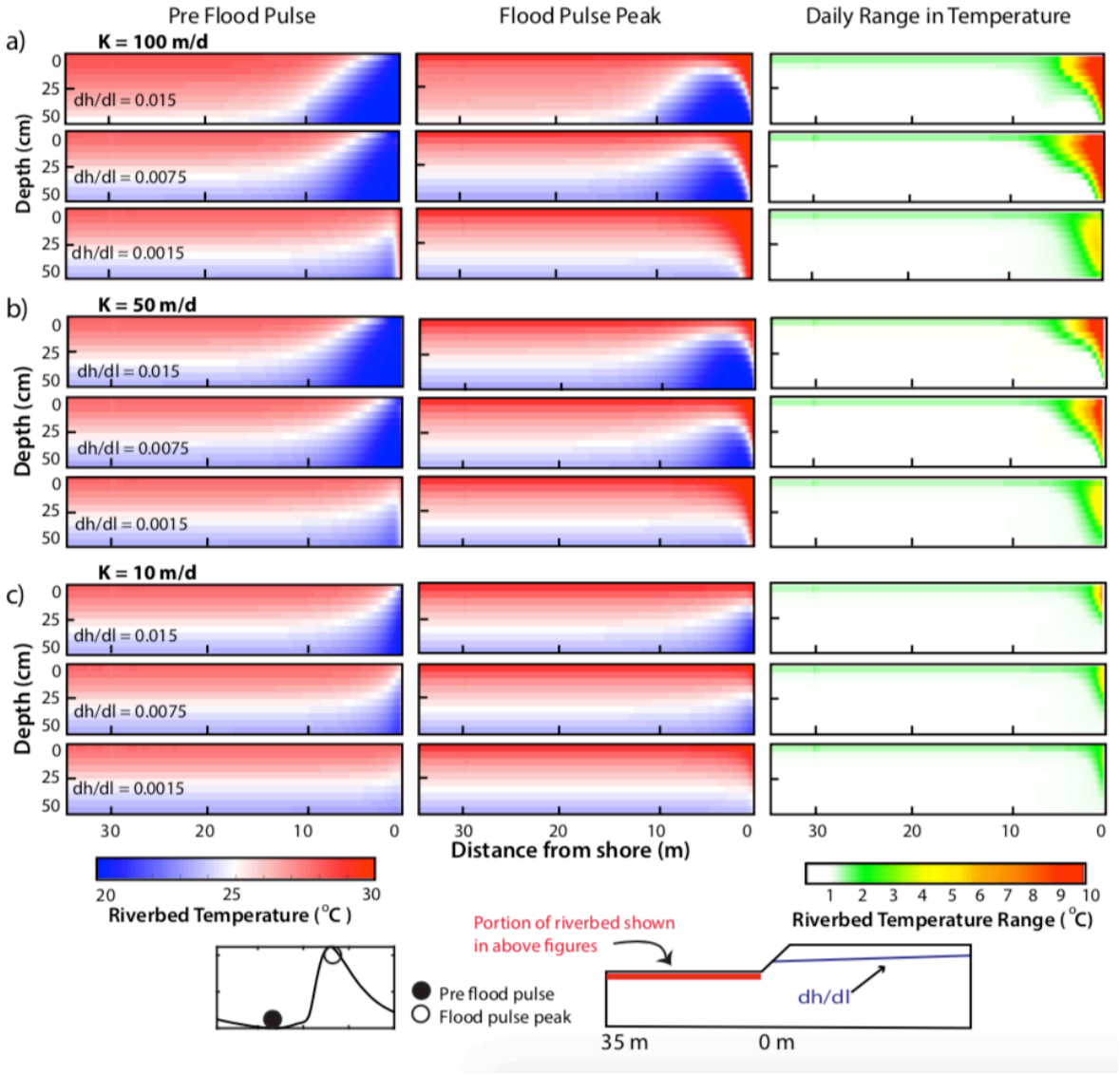

Figure 3.9: Sensitivity analysis of K and groundwater gradient on riverbed temperature

Sensitivity analysis of how hydraulic conductivity and water table configuration in riverbank control the temperature conditions in the riverbed under conditions of fluctuating stage and river temperature (same forcings as used in the rest of this study – shown in Figure 3a). The first two columns show the riverbed temperature conditions at low vs. high river stage and the third shows the 24-hour (diel) temperature range.

has the same effect; reducing the hydraulic conductivity by an order of magnitude from 100 m/d to 10 m/d causes the range in daily variability to decrease from ~5-10 °C (Figure 3.9a) to ~2-6 °C (Figure 3.9c). For all scenarios, the temperature variability in the riverbed beyond 10 m from the bank was less than 2 °C and restricted to the shallow 10-20 cm of the streambed.

Lastly, the sensitivity analysis showed that both groundwater head gradient and hydraulic conductivity control the size of the zone of dynamic temperature fluctuation near the riverbank. The size of the zone of high variability, both in lateral extent from the bank and depth into the riverbed, appears to be much more dependent on hydraulic conductivity. Higher hydraulic conductivity results in a deeper and more laterally extensive zone of temperature variability, as seen by comparing the results from the K of 100 m/day (Figure 3.9a) versus 10 m/day (Figure 3.9c). While clearly less significant, the bank head gradient influences the depth, and to a much lesser degree the lateral extent of the zone of high temperature variability. This is evident by comparing the daily temperature ranges for a given hydraulic conductivity across the three bank groundwater head gradients (Figure 3.9).

3.6 DISCUSSION

3.6.1 Mechanisms Controlling the Observed Riverbed Temperature Dynamics

The location of cooler temperatures near the bank and warmer temperatures towards the center of the channel mirrors the expected distribution of groundwater upwelling velocities in the riverbed. A water table sloping towards the river, as is the case at the study site, creates groundwater upwelling in the riverbed that declines exponentially with distance from the bank (Pfannkuch et al., 1984; Winter and Pfannkuch, 1984; Boano et al., 2008). Thus, cooling (or warming, depending on timing)

by groundwater is expected to be concentrated near the bank but not the rest of the channel, which is precisely what we observed at the study site and what our modeling results showed.

During the summer, when the field data were collected, riverbed temperatures are controlled by the competing forces of warming from the overlying water in the channel and cooling from the upwelling of groundwater. Near the bank, the upwelling velocities at low stage are rapid enough to limit warming of the riverbed sediment from the much warmer river water. As seen in the field data (Figure 3.4) and modeling (Figure 3.9), the riverbed in this region only warms during stage fluctuations that temporarily cause infiltration of warm river water. From numerous simulation and monitoring studies of flooding shores (Robinson et al., 2007; Shuai et al., 2017), the temperature observations of dynamic temperatures near the bank are not surprising. These studies show strong bi-directional or reversing flow near the interface between the channel and the bank, but little beyond the near-bank zone towards the middle of the channel. This concentration of fluid exchange near the bank creates the daily oscillations between the river and groundwater end-member temperatures in this region. In contrast, the riverbed further from the bank is consistently warm (Figure 3.6) because the rate of groundwater upwelling is not rapid enough to counter warming due to the combined forces of shallow hyporheic flow from bedform-exchange and downward conduction of heat from the warm river water. The temperatures in this region therefore reflect that of the river (Figure 3.5).

The temperature observations indicate enhanced thermal coupling between the river and streambed throughout most of the channel. This is consistent with heat transport by hyporheic flow due to bedforms (Cardenas and Wilson, 2007a; Cardenas and Wilson, 2007b; Norman and Cardenas, 2014). River discharge causes dynamic pressure gradients

along the sediment-water interface (Cardenas and Wilson, 2007b) that drive advective hyporheic heat transport (Cardenas and Wilson, 2007a; Norman and Cardenas, 2014). This is evident in the minimal lag and damping of river temperatures at the 10 cm-deep thermistors (Figure 3.4) in the central portion of the channel; in fact, the signal propagation is so efficient to this depth that the dual thermal peaks are preserved. However our observations indicate the depth of the circulating hyporheic flux is likely quite shallow, as most of the thermal signal from the river is significantly damped out by 30 to 50 cm depth for profiles beyond 10 m from the bank (Figures 3.4 and 3.5). Our modeling scenarios that evaluated different depths of enhanced hyporheic heat transport provided valuable insight about the depth of the hyporheic circulation at the study site. At the locations 15 m and 30 m into the channel, there was much greater temperature variability at 30 cm depth in the field data than for the model scenario where only the upper 20 cm of riverbed had enhanced thermal diffusivity. This suggests that hyporheic flow paths are at least 30 cm deep at these locations, which is also supported by the 40 cm-deep model scenario exhibiting better matches with the field data. Another notable feature at the locations further into the channel is that the riverbed temperatures at 30 cm and 50 cm respond to the river temperature, despite the sub-daily variations being heavily damped (Figure 3.4). This indicates that the streambed in the mid-channel area displays a longer-term conductive signal from the river. That is, over weekly to seasonal timescales, this portion of the riverbed is likely reflecting the river's mean temperature.

The sensitivity analysis of hydraulic conductivity and bank water table gradient demonstrated the effect that groundwater upwelling has on the size of the region near the bank that exhibits cool groundwater temperatures. Scenarios with lower hydraulic conductivities and bank groundwater gradients, both of which reduce groundwater upwelling rates in the riverbed, limited the amount of riverbed having groundwater-

endmember temperatures closer to the bank (Figure 3.9). The sensitivity modeling also provided possible explanations for the stark differences in the temperature dynamics near the two banks of the study site. The two likely factors contributing to the absence of any groundwater temperature signal near the right bank are lower hydraulic conductivity and lower hydraulic gradient in the right bank, both of which would result in lower pore fluid velocities and overall a more long-term conductive warming of the shallow sediments. The riverbed temperatures in the right bank (Figure 3.6) closely resemble the sensitivity modeling results from the lowest hydraulic conductivity and lowest groundwater gradient (Figure 3.9), where riverbed temperatures near the bank are consistently within the river temperature range and show no intermediate or groundwater endmember temperatures (Figure 3.5).

3.6.2 Ecological, Biogeochemical, and Physical Implications

The presence of cool groundwater upwelling in the near-bank area suggests that even in hydropeaked rivers a cool thermal benthic refugia might be present in between hydropeaking floods. Groundwater upwelling during periods between dam releases keeps near-bank portions of the riverbed cooler than the rest of the channel (Figure 3.6). It is well documented that cool patches of water near discharge points serve as thermal refugia for fish and benthic organisms (Poole and Berman, 2001; Ebersole et al., 2003; Burkholder et al., 2008; Briggs et al., 2013). This supports the idea that hydrologic connectivity with areas adjacent to but outside of the river channel can be an important control on riverbed thermal dynamics, and is why we included the riverbank in our numerical model. The relatively coarse-grained sediment at the field site (K = 100 m/day) enables a high degree of connectivity between the river and the alluvial aquifer. The connectivity near the bank is reduced by the clogging layer, whose lower hydraulic

conductivity causes less vigorous groundwater upwelling near the bank than if it were composed of coarse sand like the rest of the riverbed. The connectivity is also interrupted by the hydropeaking flood pulses, which temporarily stops cool groundwater upwelling near the bank – as seen in our field observations (Figure 3.6) and modeling results (Figure 3.9).

Biogeochemical reactions, such as respiration and denitrification, are temperature-sensitive via the Arrhenius equation. The zone of strong reversing subsurface flows has been shown to be a hotspot for reactions (Gu et al., 2012; Shuai et al., 2017). This is because reactants present in river water are delivered into the reactive subsurface during the flow reversals. This infiltration of river water also delivers heat; thus any temperature-sensitive reactions are expected to be impacted. Our finding that dam releases created streambed temperature fluctuations of up to ~6 ºC is significant. Previous modeling studies have shown that under isothermal conditions (temperature is the same everywhere and steady), a uniform change from 25 to 30 ºC results in hyporheic nitrogen removal efficiency decreases from 48.5% to 40.5%, and this is further reduced to 10.7% if temperature is imposed at 35 ºC (Zheng and Cardenas, 2016). Thus, knowledge of the spatiotemporal riverbed thermal conditions is key to accurately representing nutrient processing in hyporheic zones. This suggests that the outcomes of complex numerical flow and multi-species reactive transport models, e.g., Shuai et al. (2017), might significantly differ if dynamic heat transport in the simulated river channel is correctly included. The short-term temperature fluctuations monitored here, which are very similar in magnitude and duration to diel variations, are sufficient to induce instantaneous variations in reaction rates of several percent (Zheng and Cardenas, 2018). Thus, the temperature ranges in the banks are expected to have consequences on the rates of biogeochemical nutrient consumption.

The complex streambed-river thermal coupling and exchange patterns observed suggests time varying thermal contributions from groundwater and losses/gains of heat from bed conduction and advection. These processes may be important in the overall temperature and water quality of hydropeaked rivers. The relative influences at varied locations downstream are expected to be dependent on several factors such as: dam release timing, magnitude, and duration as well as the morphology of the river corridor (i.e. Ferencz et al., 2019). There is a clear need to determine whether highly managed rivers such as the Lower Colorado River are impaired thermally or are not meeting in stream water quality standards and if different management strategies can be developed to minimize these impairments.

3.7 Summary and Conclusions

This study uses a novel field dataset combined with numerical modeling to investigate hydropeaking's impact on the streambed thermal regime in a large regulated river. The field data revealed two thermally distinct regions in the channel. The region near the left bank (within 10 m) was characterized by cooler temperatures resembling the groundwater endmember temperature, while the riverbed in the other 60 m of the channel had temperatures similar to that of the river and were 3-6 °C warmer than the riverbed near the left bank. In addition to having distinctly different temperatures, the flood pulses from hydropeaking caused pronounced variation in the riverbed temperature within 10 m of the left bank but not the rest of the channel.

The numerical modeling provided insight into the mechanisms responsible for the observed riverbed temperature behavior. It showed that changes in hydrostatic pressure during hydropeaking releases are the cause for the temperature fluctuation in the region near the riverbank. But that the riverbed temperature over the majority of the channel can

be explained by the enhanced transport of heat from bedform-driven hyporheic exchange and the effect of stage fluctuations appears to be negligible. The sensitivity analysis demonstrated that more strongly gaining groundwater conditions and higher hydraulic conductivity create larger regions of riverbed extending outward from the bank whose temperature reflects that of groundwater in the riverbank. These conditions also favor the development of thermally dynamic zones near the bank, while lower hydraulic conductivity and less gaining groundwater conditions result in more muted temperature fluctuations.

In summary, both the field data and the numerical models support that daily stage fluctuations due to hydropeaking can substantially alter the temperature conditions in the riverbed near the bank, but that this effect does not extend across the entire channel. Our findings suggest that in large hydropeaked rivers whose width is on the order of tens to hundreds of meters, much of the riverbed would not be expected to have large daily fluctuations in temperature that span surface water and regional groundwater temperatures. Rather, much of the riverbed temperature would have temperatures that track the mean river temperature over weekly and monthly timescales and experience temperature fluctuations that are less than the daily range of the river water. This suggests that hydropeaking has the greatest potential to alter the thermal regime of aquatic organisms that reside near the riverbank, where it can interrupt groundwater upwelling and cause large temperature fluctuations. The spatial patterns we identified and their controls can help predict where hydropeaking will alter thermally sensitive processes in the riverbeds of hydropeaked or flooding rivers.

Chapter 4: Factors Influencing the Size of Aerobic Respiration Hot Spots and Net Respiration Rates in the Riparian Zones of Fluctuating Rivers

ABSTRACT

River stage fluctuations promote surface water-groundwater exchange between rivers and adjacent riparian groundwater which are part of the river corridor. Because of stage fluctuations, dissolved organic carbon (DOC), dissolved oxygen (DO), and other constituents are transported from rivers into riparian sediment where they can be consumed by microbial communities. This study evaluates how repeated daily stage fluctuations influence aerobic respiration of river-sourced DOC and DO in the riparian exchange zone using a multi-step reactive flow and transport simulation framework. Over 50 model scenarios were performed to evaluate how factors such as the duration of the daily flood signal, river DOC concentration, sediment hydraulic conductivity (K), and ambient groundwater flow condition (gaining, losing, and neutral) affects the fate and transport of DOC and DO in the riparian aquifer. Time series subsurface snapshots highlight how K, ambient groundwater flow, and river DOC influence the subsurface distribution of DOC and DO. For all scenarios, the 24-hr mass of DOC respired and the ratio of DOC that returns to the river compared to the amount that flowed in was quantified. The mass of DOC respired per unit river length had a wide range depending on the parameters, spanning from 1.4-71 g per 24-hours, with high K and losing ambient groundwater flow conditions favoring the largest amount of DOC respired. The ratio of DOC mass entering and leaving the riparian zone showed that as little as 5% to as much as 76% of the DOC that enters the bank during stage fluctuations returns to the river, and is dependent on river DOC concentration, K, and ambient groundwater flow. These

results provide insight into how key physical and chemical properties control the function of riparian zones as respiration in dynamic river environments.

4.1 INTRODUCTION:

4.1.1 Riparian Zones are Biogeochemical Buffers Between Rivers and Groundwater

Riparian zones form the dynamic interface between rivers and groundwater, and as such, are the loci of mass and energy exchange between aquatic and terrestrial ecosystems. As the transitional region between surface water and groundwater, riparian zones often exhibit steep gradients in physical and chemical properties, causing them to be hot spots for biogeochemical processes [McClain et al., 2003; Naimen and Decamps, 1997; Yarrow and Marin, 2007]. The coupling of hydrology (flow) and biogeochemistry (reactions) acting on water moving within riparian zones causes them to act as natural "filters" for carbon and other essential macronutrients (nitrogen and phosphorous) [Bouwman et al., 2013; Brugger et al., 2001; Sharma et al., 2012; Vidon et al., 2010]. Riparian zones are regions of rich biogeochemical activity [Devito et al., 2000; Hedin et al., 1998; Moser et al., 2003] that contribute to nutrient dynamics in river ecosystems and influence river biogeochemistry [Boulton et al., 2010; Covino, 2017; Dent et al., 2001; Harvey et al., 2019].

Field studies provide insight into the spatial organization and gradients of organic matter, oxygen, microbial organisms, and other important constituents (ex. nitrogen & phosphorous) within riparian zones. Typical field studies involve sampling/measuring concentrations of dissolved species in riparian groundwater along perpendicular transects that are positioned along lateral subsurface flowpaths in riparian groundwater flowing towards or away from the river [Dahm et al., 1998; Devito et al., 2000]. Sampling captures the spatial and temporal distribution of chemistry through repeated

measurements to construct time series at sub-daily [Barnes et al., 2019; Briody et al., 2016] or seasonal [Baker et al., 2000; Duval and Hill, 2006; Gu et al., 2008; Hoppe-Jones et al., 2010; Wroblicky et al., 1998] scales. Field data highlights biogeochemical processing of nutrients in riparian sediments, evidenced by the consumption of dissolved organic carbon (DOC) and dissolved oxygen (DO) with distance away from the river channel [Bourg and Bertin, 1993; Brugger et al., 2001; Hoppe-Jones et al., 2010]. Many studies have also focused on nitrate dynamics in riparian zones because of its role as a limiting nutrient in aquatic environments, with excess nitrogen loads causing eutrophication of inland and coastal waters. Studies have shown that riparian zones can act as effective buffers to the movement of nitrogen between rivers and adjacent groundwater [Hill, 1996; Roley et al., 2012].

The DOC and DO conditions in the riparian zone determine nitrogen dynamics. The extent of oxygenated water dictates where in the riparian zone the groundwater conditions favor net nitrification versus net denitrification [Zarnetske 2012]. In aerobic regions, dissolved organic nitrogen can be mineralized into ammonium (NH_4^+), which can subsequently undergo reductive transformation into nitrate (NO_3^{2-}). Whereas under anaerobic conditions, DOC and NO_3^{2-} are consumed by denitrification producing N_20 and N_2 gasses, which can be evaded to the atmosphere. Thus, understanding the DO and DOC conditions in riparian zones not only provides direct insight on aerobic carbon cycling, but determine the sequence of redox reactions all the way to anoxic conditions.

4.1.2 Stage Fluctuations as Drivers of Biogeochemical "Hot Spots" in Riparian Zones

Stage fluctuations facilitate lateral surface water-groundwater (SW-GW) "exchange flows" of mass and energy between the river channel and the adjacent riparian

zones that enhance the hydrologic connectivity between the rivers and their surrounding sediments; meaning they behave less like pipes that convey water downstream, and more as dynamically coupled environments that are interacting with, and being modified by reactions occurring in hydraulically connected sediments of their riverbeds and riparian zones [Dahm et al., 1998; Harvey and Gooseff, 2015]. Exchange flows occur over a wide range of time scales ranging from as short as hours to as long as months [Helton et al., 2012; Zarnetske et al, 2011; Stegen et al., 2018]. In rivers that have frequent stage fluctuations, such as in tidal zones [Barnes et al., 2019; Musial et al., 2016; Wallace et al., 2019] or dammed rivers [Boutt and Flemming, 2009; Sawyer et al., 2009], lateral exchanges are much more frequent. Aside from the frequency, the intensity and duration of exchange flows are key factors controlling the availability of nutrients and oxygen within the riparian zone [Findlay, 1995]. Regions that receive inputs from surface waters can form "hot spots" where the presence of oxygen and nutrients imported from exchange flows stimulate "hot moments" of elevated biogeochemical activity [Pusch et al., 1998; McClain et al., 2003].

Virtual experiments with numerical flow and transport models are useful tools for exploring factors that control exchange flows and for assessing their effect on biogeochemical reactions under simplified and idealized conditions. Early models simply assessed fluid exchange between the river and riparian aquifer [Pinder and Sauer, 1971; Squillace, 1996, Whiting and Pomeranets, 1996]. Even many recent studies focus only on conservative (non-reactive) solute exchange between the river and riparian zone [Liu et al., 2019; McCallum et al., 2010; Welch et al., 2013]. A small number of modeling studies have used modeling to study factors influencing nutrient dynamics in riparian zones during exchange flows [Gomez-Velez et al. 2017; Gu et al., 2012; Shuai et al., 2017; Song et. al, 2018]. These studies varied parameters that affect the movement of

fluid and solutes, such as hydraulic conductivity [Gomez-Velez et al., 2017; Gu et al., 2012; Shuai et al., 2017], water table configuration in the riparian zone [Gomez-Velez et al., 2017; Shuai et al., 2017], dispersivity [Shuai et al., 2017], temperature [Song et al., 2018], and river fluctuation amplitude [Gomez-Velez et al., 2017; Gu et al., 2012; Shuai et al., 2017]. However, with the exception of Song et al. [2018], aerobic respiration was not the focus of most of these studies. There has not been a comprehensive assessment of how hydraulic conductivity, ambient groundwater flow conditions, and river DOC combine to influence aerobic respiration in the riparian zones of fluctuating rivers. Since aerobic respiration is the foremost reaction which determines the biogeochemical function of exchange zones, it is important to develop predictive understanding. Numerical models can help with this.

4.1.3 Assessing Respiration Under Conditions of Repeated Stage Fluctuations

Recently, there has been an increase in research directed towards understanding biogeochemical processes in rivers that have frequent and periodic stage changes. The hypothesis is that SW-GW exchanges in dynamic rivers, such as dammed or tidal environments, may play a heightened role in regulating nutrient fluxes in these environments [Graham et al., 2019]. Because dammed rivers are already impaired in many ways that alter their ecological functioning and health [Wohl, 2019], there is particular interest in determining how SW-GW exchange and attendant biogeochemical processes are perturbed by regulation of the natural flow regimes. However, there is a lack of observational field data and theoretical modeling results to support even a basic understanding of how common physical parameters such as sediment hydraulic conductivity, groundwater flow conditions in the riparian zone, and river chemistry control aerobic respiration in the riparian zones of dynamic rivers. In part, this is because

limited field data has been collected on SW-GW exchange dynamics in dammed rivers [Sawyer et al., 2009; Siergieiev et al., 2014; Yellen and Boutt, 2015; Zachara et al., 2020]. The field studies are also constrained by the field conditions at the study sites, which is why modeling is a useful tool for testing the sensitivities to a range of parameters. Modeling studies to date have also been limited in scope, either because only a conservative solute was considered [Boutt and Flemming, 2009; Ferencz et al., 2019; McCallum et al., 2010] or the reactive transport modeling was limited in the variety and range of parameters considered [Shuai et al., 2017; Song et al., 2018].

This study ultimately utilizes reactive transport modeling to investigate how daily floods representative of dam releases stimulate subsurface aerobic respiration. The objective of this study is to advance understanding of how repeated daily artificial flood events, representative of dammed hydropeaking operations, affect the formation of respiration hot spots in the riparian zones of dammed rivers. The experimental approach uses artificial dam release signals to drive exchange flows with the riparian zone to assess the sensitivity of respiration hot spots in a river with daily stage fluctuations to variations in (1) hydraulic conductivity, (2) groundwater flow conditions in the riparian aquifer, and (3) river DOC concentration. The simulations measure the distribution of DOC and DO in the riparian zone and quantify the amount of DOC that is respired over a representative 24-hour period. The parameters investigated span three different durations of hydropeaking releases, three values of K, and five different groundwater flow conditions, and three different concentrations of river DOC.

4.2 METHODS:

4.2.1 Numerical Modeling Framework

4.2.1.1 Linked Surface Longitudinal-Subsurface Transverse Models

This study utilizes the two-step longitudinal-transverse modeling scheme employed in Ferencz et al. (2019). The first step is downstream river routing of a dam-release signal by solving the 1D form of the shallow water equations using HEC-RAS, which is the U.S. Army of Corps of Engineers' river hydraulics modeling code. The output time series of the river stage from HEC-RAS is then used as an input to a numerical model of lateral SW-GW exchange between the river and adjacent riparian zone. The numerical groundwater flow and reactive transport model is a 2D vertical cross-sectional model oriented perpendicular to the channel. Specifications of the groundwater flow model are provided in Section 2.2 below. In Ferencz et al. (2019), SW-GW exchanges were evaluated at multiple longitudinal distances from the dam. Here, due to the computational demand of reactive transport modeling, exchange at the single distance of 10 km downstream is considered. At this location, we assess the sensitivity of riparian zone respiration to four properties: dam signal length, hydraulic conductivity of the riverbed and riparian zone sediment, ambient groundwater flow conditions in the riparian zone, and concentration of DOC in the river.

4.2.1.2 Dam Signals used for the Reactive Transport Model

A square-type dam release was used as it is a common hydrograph shape generated by hydropeaking operations (see Ferencz et al., 2019 for example hydrographs). Three square-type dam signals were modeled, all with an amplitude of 1m, but with three durations 2, 4, and 8-hours. The specifications for the river were a width of 100 m, a slope of 0.001 m/km, Manning's n of 0.4 – representative of a large, higher

order river, which is typical for rivers that have large hydroelectric operations. The background depth of the river was 1 m and the floods temporarily increased the stage by a meter. Time series of river stages resulting from the HEC-RAS surface water model outputs at the study transect location (10 km downstream) were used as boundary conditions for the 2-D subsurface flow models (Figure 4.1a). This is a feature of our modeling approach that is an advancement from earlier studies of dam-driven SW-GW exchange, which approximated the river stage boundary condition using a sinusoidal signal [Shuai et al., 2017; Siergieiev et al., 2015].

4.2.2 Flow and Transport Model Details

Although the study included flood river routing modeling, it is focused on subsurface processes. Details of the surface model (HEC-RAS) can be found elsewhere, e.g., the HEC-RAS documentation (https://www.hec.usace.army.mil/software/hec-ras/). Here, we present only the details of the subsurface model.

4.2.2.1 Governing Equations for Subsurface Flow and Reactive Transport

The subsurface fluid flow and reactive transport processes were modeled using COMSOL Multiphysics, a generic finite-element modeling software. The model solves unsaturated flow in porous media based on Richards equation (Eq. 1) and solute transport based on the advection-dispersion-reaction equation (Eq. 2).

$$\rho\left(\frac{C_m}{\rho g}+S_e S\right)\frac{\partial p}{\partial t}+\nabla\cdot\rho\left(-\frac{k_s}{\mu}k_r(\nabla p+\rho g\nabla z)\right)=Q_m \tag{1}$$

$$\frac{\partial}{\partial t}(\theta C_i)=-\nabla\cdot\rho(qC_i)+(D\nabla^2 C_i)+R_i \tag{2}$$

where p is pressure [$MT^{-2}L^{-}$], ρ is fluid density [ML^{-3}], C_m is specific moisture capacity [L^{-}], S_e is effective saturation [-], S is the storage coefficient [-], k_s is the saturated hydraulic permeability [L^2], k_r is the relative permeability dependent on saturation [-], μ is the dynamic viscosity of the fluid (water) [$ML^{-}T^{-}$], z is the elevation head [L], g is gravitational acceleration [LT^{-2}], and Q_m is a stress source term that accounts for changes in total stress under fluctuating river stage [$ML^{-3}T^{-}$]. C_i is the concentration of solute species i [ML^{-3}], θ is the volumetric water content [-], q is the Darcy velocity [LT^{-}], D [L^2T^{-}] is the effective dispersion coefficient which includes the macro-dispersion tensor, defined by dispersivity and pore velocity, plus molecular diffusion, and R_i is the reaction rate for species i. All physical and chemical properties controlling flow and transport within the model domain were homogenous, and are summarized in Table 1.

A Monod kinetics framework was used to model the reactive transport of DOC and DO. Aerobic respiration in our model uses formaldehyde for DOC. The balanced chemical reaction for aerobic respiration used in this model is described by Eq. 3.

$$CH_2O+0_2 \rightarrow H_2O+CO_2 \quad (3)$$

The formulation of the reaction rates for DO (R_{DO}) and DOC (R_{DOC}) consumed during aerobic respiration follows that used in preceding studies by Zarnetske et al. (2011a), Gu et al., (2007), and Shuai et al. (2017)

$$R_{DOC} = R_{DO} = -\theta X_{AR} V_{AR} \left(\frac{C_{DOC}}{K_{DOC}+C_{DOC}}\right)\left(\frac{C_{DO}}{K_{DO}+C_{DO}}\right) \quad (4)$$

where R_{DOC} is the reaction rate for DOC, R_{DO} is the reaction rate for DO, V_{AR} is the maximum uptake rate, X_{AR} is the biomass of the microbial group performing aerobic

respiration and is similar to the values used in reactive transport modeling studies of respiration in river and riparian sediments [Barnes et al., 2019; Gu et al., 2007; Shuai et al., 2017; Xian et al., 2019], C_{DOC} and C_{DO} are the concentrations of DOC and DO, K_{DOC} and K_{DO} are the half-saturation constants for the two species. The reaction rates of DO and DOC are equal to one another as mol/time because they are consumed at the same rate on a mole-by-mole basis as shown in Eq. 3. The values for the reaction parameters are summarized in Table 1.

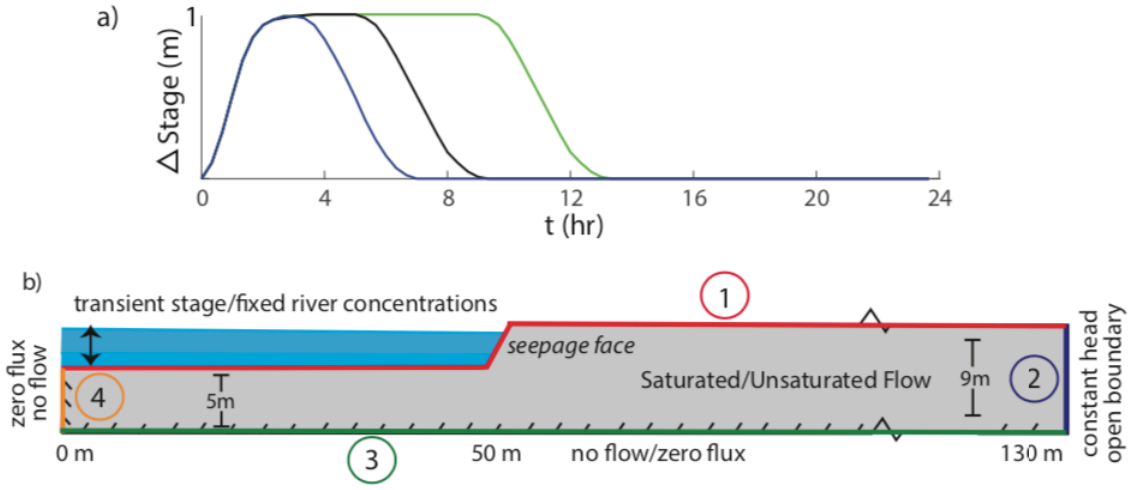

Figure 4.1: Numerical model design schematic

River stage boundary conditions (a) for the three flood durations modeled. Reactive transport domain (b) with boundary conditions.

4.2.2.2 Model Domain and Boundary Conditions

The 2-D flow and transport model is based on a simplified physical representation of a river and the adjoining riparian zone (Figure 1b). The model is 130 m in width, 50 in river and 80 in riparian zone. The model consists of 20,000 triangular elements that range in size from 0.05 m to 0.4 m, with finer mesh in the vicinity of the top boundary, where

the solute flux between the river and groundwater occurs. The transport model was run with a maximum time-step limit of 30 seconds, which was obtained through trial and error based on model convergence success. A 30-second maximum time step minimizes numerical dispersion as it is well below the advective transport rate that can occur across the smallest element size (5-cm) for the simulated conditions. Three solutes were modeled: (1) dissolved organic carbon - represented by CH_20, (2) dissolved oxygen, which control aerobic respiration, and (3) a non-reactive tracer, which was set to the same concentration as DOC and used to compare the reactive transport results with those of a non-reactive solute. Transport of a conservative solute is typically considered in previous modeling-based investigations [Liang et al., 2018; Liu et al., 2019; McCallum et al., 2010; Welch et al., 2014; Xie et al., 2016]. Here, we use it as a reference and also for determining conservative solute-specific metrics.

The boundary conditions for fluid flow consist of a seepage face along the channel-bank continuum (boundary 1), a constant head, open boundary at the right-hand side is used to define the ambient groundwater gradient and allows fluid to enter and leave the domain (boundary 2), and no flow boundaries at the riparian aquifer base (boundary 3), and a symmetry boundary (river half-width) on the left-hand side of the model (boundary 4). The seepage face along the top boundary is controlled by a conditional statement that, at each time step, evaluates the pressure in each boundary element; the elements along the seepage face are set to zero pressure, elements above are set to zero-flux, and elements below are set to head equal to the river-stage. This approach to modeling a seepage face has been implemented in previous studies by Cardenas et al. (2015), Shuai et al. (2017), and Ferencz et al., (2019) and is outlined in Reeves et al. (2000).

The boundary conditions that control solute transport are similar to those for fluid flow, but with some key differences. As for the flow model, the left and bottom boundaries (3 and 4) are no-flux boundaries for solute species. The right boundary (2) is an open boundary, but unlike the flow model does not have a specified concentration value. Finally, along the top boundary (3), the concentrations of the dissolved species in the river are applied only to model cells that are below the seepage face; the river concentration boundary moves dynamically with the river stage. In our model, the river is the sole source of solutes for the domain. Similar assumptions were made in reactive transport modeling of stage-driven lateral SW-GW exchange by Gu et al. (2012) and Shuai et al. (2017). In both studies, initial concentrations of species in the model domains were set to zero. Notably, Shuai et al. (2017) included a source term representing the generation of DOC from particulate organic carbon (POC), which produced DOC in the model domain during the transient reactive transport modeling. Since our study considered many times more simulations than Shuai et al. (2017), we chose not to include the added complexity of POC dissolution.

Initial flow conditions are established by running a steady state flow model with the river stage at its background level of 1 m depth and a constant head value along the right-hand boundary. The head values assigned to the right boundary ranged from 0.79 m lower or higher than the river level (corresponding to gradients of -0.01 or 0.01). The initial conditions for solute species are homogenous concentrations throughout the model domain of 1×10^{-6} mol/m^3; a very small, non-zero value so that there is not an infinite concentration gradient between the river and the subsurface at time zero.

Flow Parameters	*Value(s)*	*Unit*
Hydraulic conductivity (K)	1, 10, 100	m/d
Porosity	0.3	-
van Genuchten (α)	10	-
van Genuchten (n)	2	1/m
Residual water content ($_r$)	0.1	-
Dam release period	2, 4, 8	h
Amplitude	1	m
Reaction Parameters		
O_2 concentration in the river	9	mg/L
DOC concentration in the river	2, 6, 12	mg/L
Maximum specific uptake rate for AR (V_{AR})	2[a,b]	1/h
Half saturation constant for 0_2 (K_{02})	1[b,c]	mg/L
Half saturation constant for DOC (K_{DOC})	2[b,c]	mg/L
Biomass of respirational group (XAR)	$6.25*10^{-5}$, [b]	kg/m^3
Longitudinal dispersivity (αL)	1	m
Transverse dispersivity (αT)	0.1	m
Molecular diffusion coefficient (D)	$1*10^{-10}$	m^2/s

Notes:

[a] Zarnetske et al. 2012, [b] Shuai et al., 2017, [c] Gu et al. 2012

Table 4.1: Flow and reaction parameters used for the reactive transport model

4.2.3 Variation of Parameters in Virtual Experiments

River DOC, aquifer K, ambient groundwater flow conditions, and flood wavelength were the parameters varied in this study. The three river DOC (C_{DOC}) values considered were 2, 6, and 12 mg/L, which are common ranges observed within the conterminous United States [Hanley et al., 2013]. To limit the number of simulations, river DO (C_{DO}) was 9 mg/L for all scenarios. This concentration represents equilibrium DO saturation between the atmosphere and water at 20 °C. Three K values of 1, 10, and

100 m/d were assessed. Five different ambient groundwater flow conditions were modeled with hydraulic head gradient values of -0.01, -0.005, 0, 0.005, and 0.01 (negative gradient denotes flow away from the river, positive denotes flow towards river). Lastly, three durations of dam release-induced floods (2-hr, 4-hr, and 8-hr) were used as the upstream river stage boundary condition for the river routing model.

4.2.4 Metrics Used for Assessing the Virtual Experiments with Reactive Transport Models

The subsurface flow and reactive transport simulations were run for seven days to examine the control of the model parameters on the rate of DOC reaction in the riparian zone, the growth rate/size of the respiration hot-spot, and the difference between the reactive transport solute species and the conservative river tracer. Initially, models with simulation durations ranging from one day (one flood cycle) to three days (three flood cycles) were considered. However, an assessment of the results from these simulations indicated that important properties of respiration hotspot dynamics would be mischaracterized if comparative metrics from the simulations were made after only 24 or 72 hours. By testing a subset of our parameter space over ten day periods, it was found that a quasi-steady state was achieved by seven days. This quasi-steady state behavior is illustrated in Figure 3, where it can be seen that the rate of increase in DOC mass in the domain initially grows rapidly in the first few days, but then starts to asymptotically level off over days four through seven.

We used the metrics of net 24-hour DOC respiration rate per unit river length, mass return ratio, and the lateral extent of DOC and DO in the riparian zone to assess the effect that the model parameters had on riparian zone respiration hot sports. The net 24-

hour DOC respiration rate is the mass of DOC that is consumed over the entire model domain over a 24-hour flood cycle, per river length (Eq. 5).

$$M_{DOC} = \int_{t1}^{t2} \int_{\Omega} R_{DOC} d\Omega dt \quad (5)$$

where M_{DOC} is the mass of DO consumed by aerobic respiration (R_{DOC}) in the domain area Ω, over a 24-hr period spanning from t1 to t2, which for this study was the 24 hours of the seventh day of the simulation.

The mass return ratio is the mass flux of DOC that returned to the river (outward DOC mass flux) divided by the mass flux that entered the riparian zone (inward DOC mass flux) over a 24-hour period. It describes how much of a sink the riparian zone is for the river-derived DOC under continuously fluctuating conditions. A low mass return ratio indicates that a large percentage of DOC that enters the riparian zone does not return back to the channel, and conversely, a high ratio means that much of the DOC mass that flowed into the riparian zone during the flood returns to the river during the flood recession.

In addition to the net 24-hour aerobic respiration rate and mass return ratio, snapshots of the subsurface distribution of DOC and DO in the riparian zone are presented in order to evaluate how the spatial distribution of DO and DOC was influenced by the model parameters.

4.3 RESULTS:

4.3.1 Snapshots of Riparian Exchange Zone Flow Field Under a Flood Pulse Cycle

The riparian exchange zone flow field response to river stage fluctuations depends a lot on the ambient groundwater flow conditions (Figure 2). Figure 2 shows the flow

fields for gaining, neutral, and losing conditions responding to a 4-hour dam signal for an aquifer K of 100 m/day. In the figure the vectors are scaled proportionally to groundwater flow velocity. For neutral conditions, where no background groundwater flow exists between the riparian zone and the river, there is intense but short lived, inflow and outflow as the stage rises and falls (Figure 2b). For gaining river conditions (groundwater flow towards river), the rising limb of the flood wave temporarily reverses the flow direction (Figure 2a). As the flood wave recedes, flow towards the river resumes. Under losing river conditions, river water is constantly entering the riparian zone even during baseflow river conditions (Figure 2c).

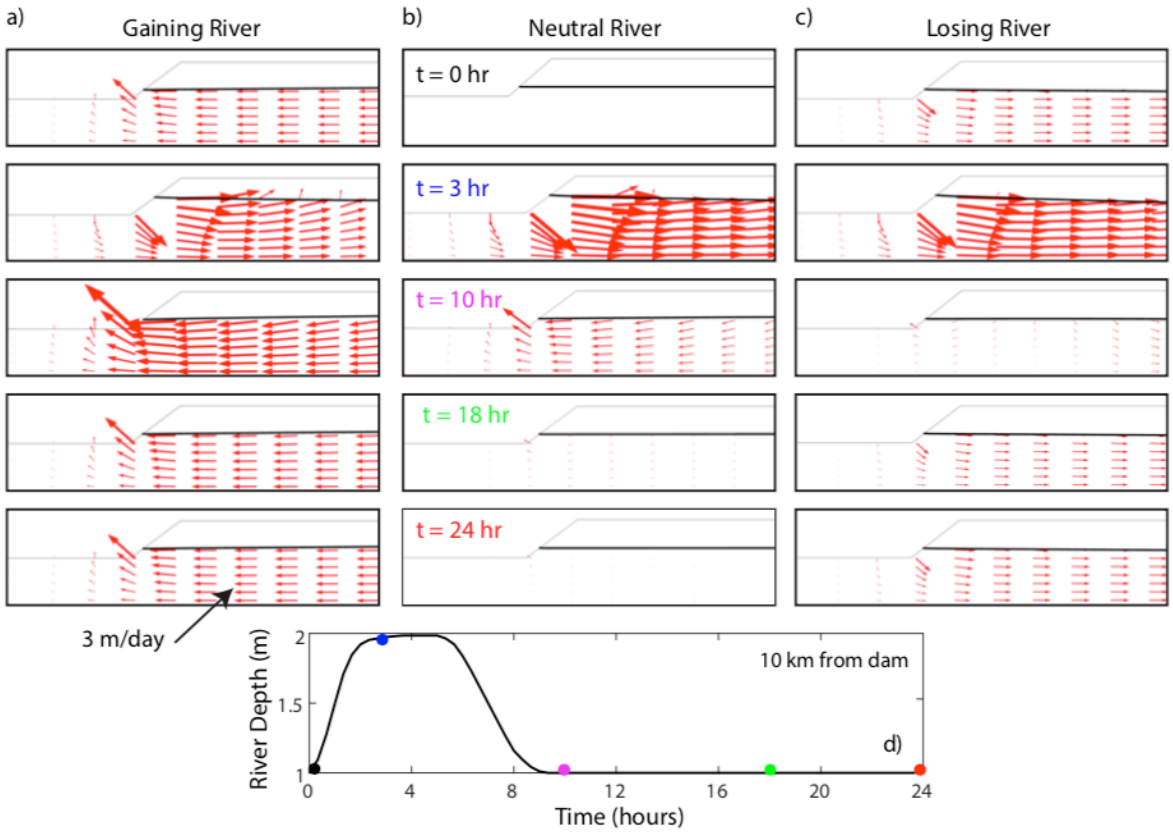

Figure 4.2: Flow field snapshots showing response of gaining (a), neutral (b), and losing(c) groundwater flow conditions to a 4-hr flood at the study distance of 10 km (d). The aquifer has K = 100 m/d and the gaining and losing conditions are for gradients of 0.01 and -0.01. Flow field vectors are scaled proportionally to velocity.

The rising limb of the flood intensifies the inward flow, and during the falling limb there is some return flow to the river, but as with the neutral conditions, the flow reversal is short lived and flow away from the river resumes not long after the flood recedes.4.3.2 **Solute Field Snapshots Illustrating Sensitivity to K and Ambient Groundwater Flow**

The combined effects of sediment K and ambient groundwater flow on the accumulation of DOC in the riparian zone are shown in Figure 3. The snapshots show the evolution of riparian zone DOC concentrations for a seven-day period of repeated 4-hour dam signals, the river stage is the same as shown in Figure 1b (24-hour flow field snapshots). Three ambient groundwater gradients were simulated for each K value: gaining (gradient = 0.01), neutral (gradient = 0), and losing (gradient = -0.01). A river DOC concentration of 6 mg/L was used.

The snapshots illustrate that with larger K, the influence of ambient groundwater flow on the extent of the DOC zone becomes more important, as seen by the increasingly different distributions of DOC as K varies from 1 to 100 m/d (Figure 3). Ambient groundwater flow orientation has little effect on the size of the DOC plume for the K = 1 m/d scenarios; for all three groundwater conditions the DOC extent is less than 5 meters into the riparian zone. The effect of ambient groundwater flow orientation becomes more apparent for the K = 10 m/d scenarios, but there still is not much of a difference between flow towards the river with a head gradient of 0.01 and flow away with a gradient of -0.01 resulting in less than 2-meter difference in the lateral extent of the DOC plume at day 7. In contrast to the results for the K=1 and 10 m/d, the K = 100 m/d scenarios show large differences in the DOC plume extent, with the extent for the losing condition causing DOC to be more than 15 m further into the bank compared to the gaining conditions.

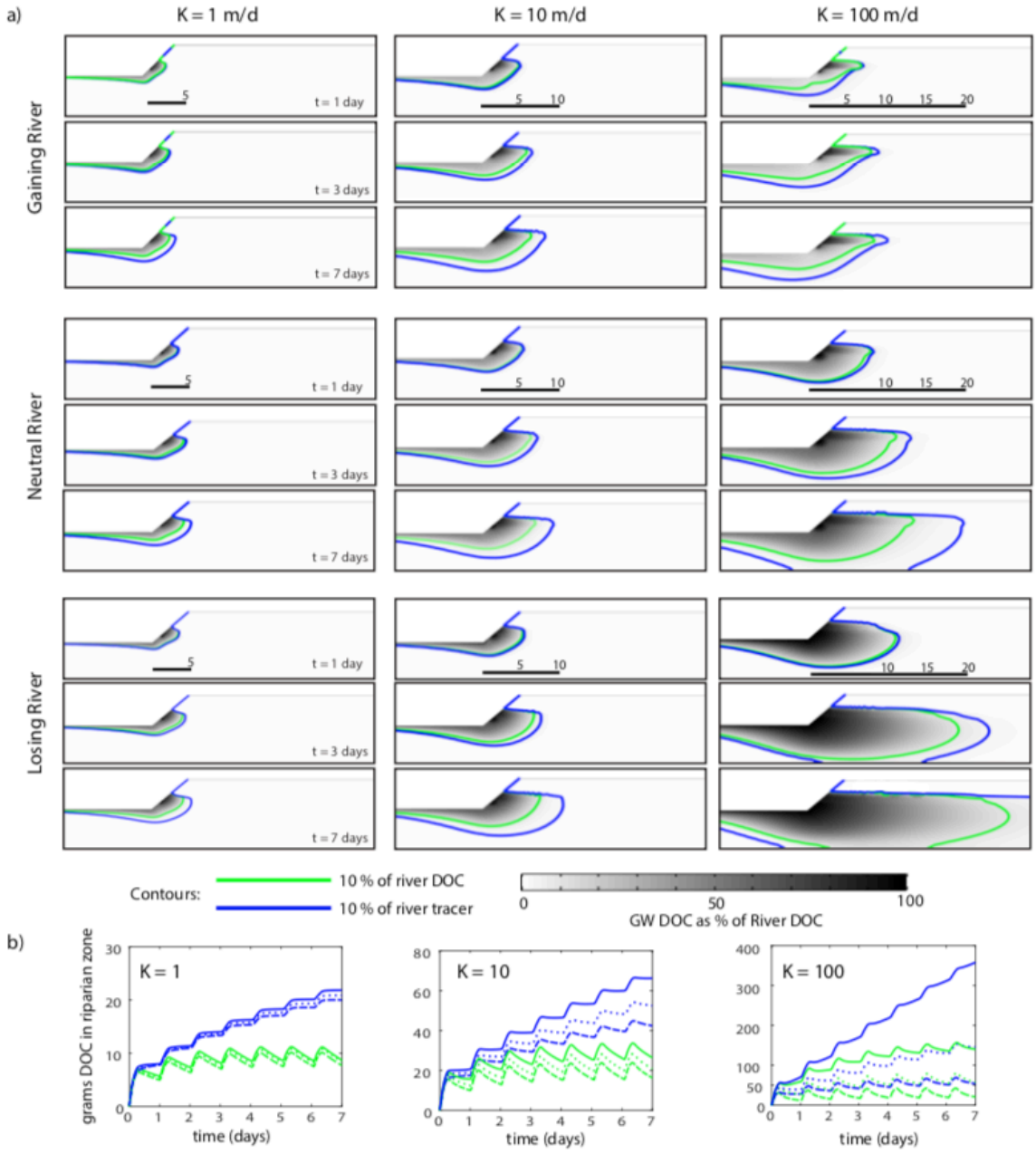

Figure 4.3: Snapshots of DOC distribution and net DOC mass for varied K and groundwater flow conditions

Snapshots of DOC concentration after 1, 3, and 7 days of continuous daily floods (a). Contours show the extent of 10% concentration relative to the river for DOC and non-reactive tracer. Time series of DOC and tracer mass over the seven days in (b). Losing conditions (solid), neutral (dotted), gaining (dashed).

The effect of respiration consuming DOC in the riparian zone can be seen by comparing the green (DOC) and blue (tracer) contours denoting the position of the 10% concentration extent relative to the river. The conservative tracer expectedly propagates further, as it is diluted and transported by dispersive mixing while not being consumed. Similar to how higher K magnified the effect of groundwater flow on the DOC extent, higher K values also cause larger separation differences between the DOC and tracer 10% concentration contours.

In addition to showing the spatial extent of DOC, the effect of K and groundwater flow on DOC mass accumulation in the riparian zone was assessed by evaluating the accumulated solute mass over the seven-day modeling period (Figure 3b). The time series plots show the grams of river-sourced DOC, and for comparative purposes grams of tracer, in the riparian zone. For all three K values and groundwater conditions, the asymptotic behavior of DOC concentrations can be seen in the time series of DOC mass as the accumulated mass still fluctuating daily but no longer increasing. At the end of 7 days, the mass of DOC in the riparian zone for the K = 1 scenarios ranges from 7.7-8.7 g, the K = 10 m/d from 16-26 g, and the K = 100 m/d from 22-140 g. As seen in the snapshots, gaining conditions result in less accumulated DOC, losing with more, and neutral in between. The range separating the different GW orientations becomes larger with increased K, going from 1 g for K = 1m/d to 118 g for K = 100 m/d. The blue curves showing the accumulated tracer mass show the effect of respiration on reducing the accumulation of DOC over repeating stage fluctuations.

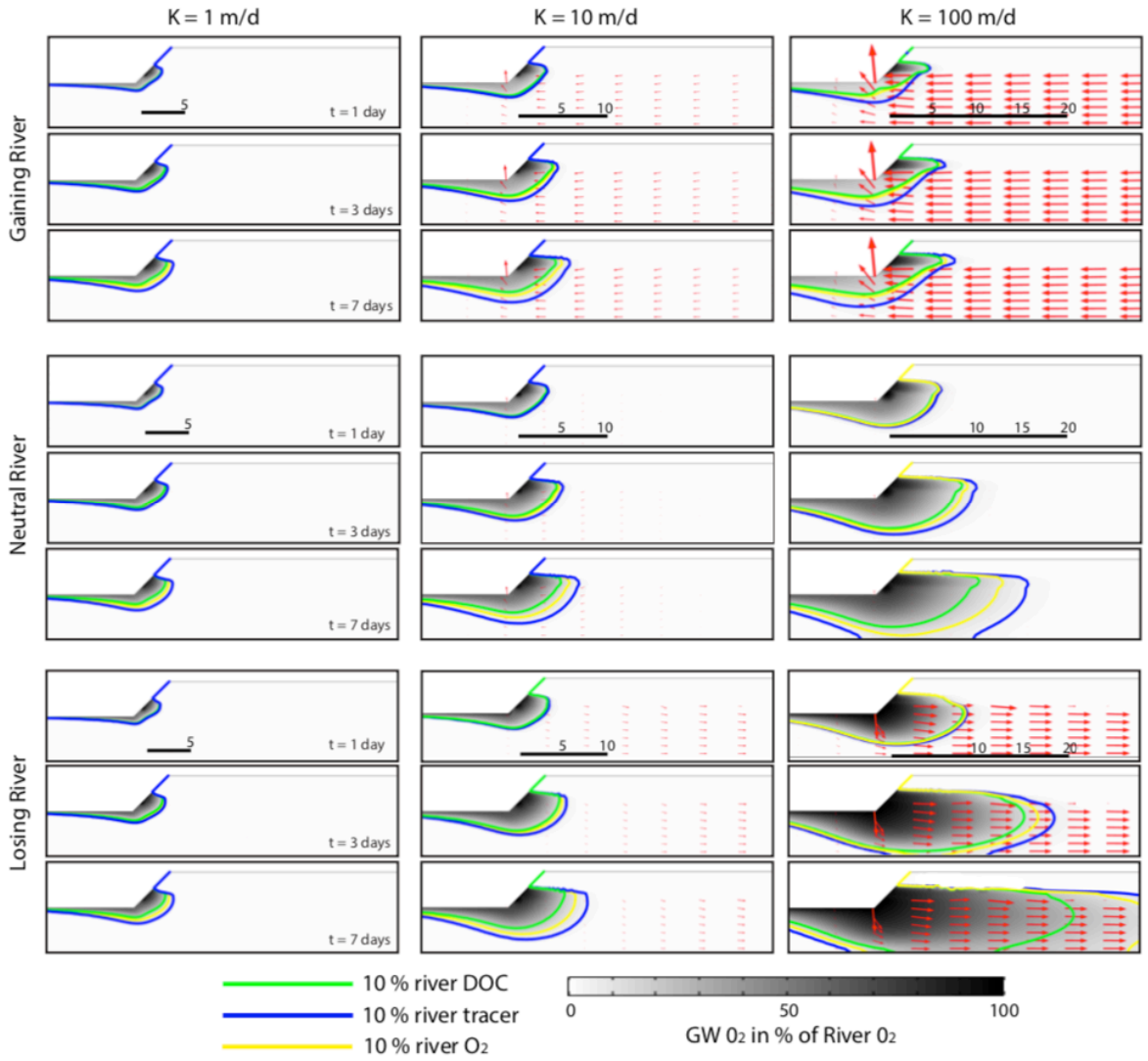

Figure 4.4: Snapshots of DO distribution for varied K and groundwater flow conditions

Snapshots of DO concentration after 1, 3, and 7 days showing the effect of K and groundwater flow conditions. The snapshots correspond to the DOC snapshots in Figure 3. Contours show the extent of 10% concentration relative to the river for DO, DOC, and non-reactive tracer.

Besides controlling where aerobic respiration occurs, where dissolved oxygen is/is not in the riparian zone is suggestive of where denitrification is less/more likely to occur. Snapshots of dissolved oxygen for the snapshots in Figure 3 are shown in Figure 4.

As with the DOC distributions, groundwater flow becomes more of a factor for DO distribution as K increases. The 10% DO contour extends further into the riparian zone in all snapshots because the DO concentration in the river (9 mg/L) is larger than the DOC concentration (6 mg/L) - for these scenarios DOC is the limiting reactant so it gets consumed before all of the DO does. Groundwater flow fields, scaled proportionally to flow velocity, show how the K value controls the magnitude of fluid flow. The flow vectors cannot be seen for the K = 1 m/d scenarios. This helps explain why there is not much difference between the gaining, neutral, and losing groundwater conditions for the K = 1 m/d scenarios.

4.3.3 Snapshots Showing Sensitivity to River DOC and Ambient Groundwater Flow

The effect of differing river DOC concentrations on the accumulation of DOC in the riparian zone are shown in Figure 5. As in the previous set of snapshots, these show the evolution of DOC distribution over a seven-day period at a location 10 km downstream from the dam. As with the first set of snapshots, the three groundwater head gradients were -0.01, 0, and 0.01. The three DOC values considered were 2, 6, and 12 mg/L. For these snapshots, hydraulic conductivity is held at a constant of 100 m/d so the effects of varied DOC and ambient groundwater flow orientation can be examined in isolation. Based on the insight from the first set of snapshots where K was varied, a K = 100 m/d was chosen so the effect of varied DOC and groundwater would be most apparent.

The snapshots reveal that groundwater flow orientation can be an important control on how rapidly DOC accumulates in the riparian zone. For gaining conditions where flow is towards the river, the different river DOC concentrations have little effect on the spatial distribution. For gaining conditions, after seven days the lateral extent of

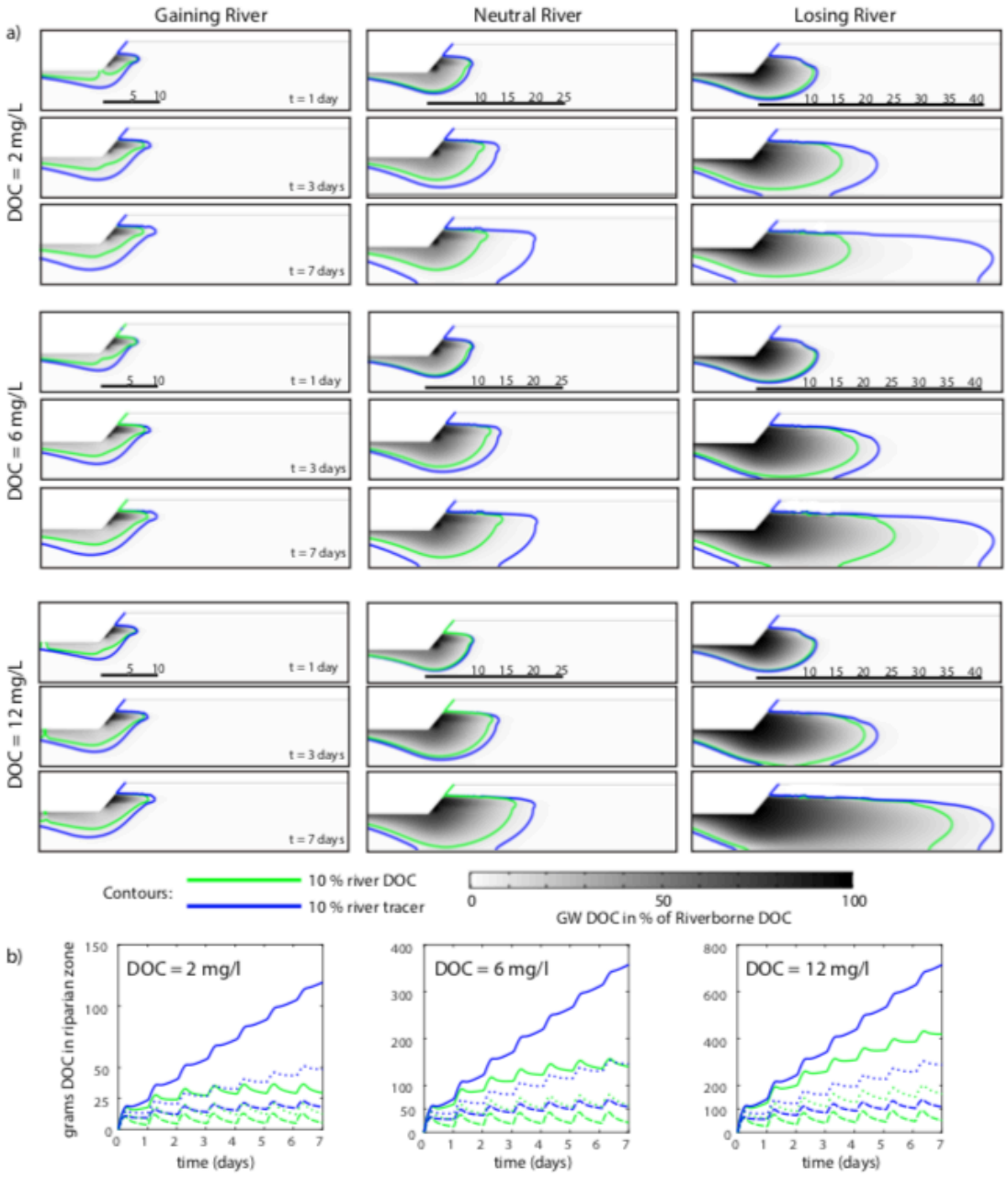

Figure 4.5: Snapshots of DOC distribution and net DOC mass for varied river DOC and groundwater flow conditions

Snapshots of DOC concentration after 1, 3, and 7 days of continuous daily floods (a). Contours show the extent of 10% concentration relative to the river for DOC and non-reactive tracer. Time series of DOC and tracer mass over the seven days in (b). Losing conditions (solid), neutral (dotted), gaining (dashed).

the 10% DOC concentration contour remains within 10 m of the bank for all three DOC values. For neutral conditions, there is no background flow towards the river so the 10% DOC contour is ~5 m further into the riparian zone than for the gaining conditions. The effect of DOC concentration on the distribution of DOC in the riparian zone is also more apparent for the neutral conditions; comparing the C_{DOC}=2 and the 12 mg/L neutral river snapshots, it can be seen that besides having a smaller area, the relative concentrations of the C_{DOC}=2 mg/L are much lower than the 12 mg/L scenarios. The riparian exchange zone under losing conditions exhibited the most sensitivity to river DOC concentration. Under such conditions, at the end of 7 days, the C_{DOC}=12 mg/L scenario showed a plume that is 20 m further into the riparian zone than for C_{DOC}=2 mg/L. In contrast, for gaining conditions the difference between C_{DOC}=2 mg/L and 12 mg/L plume penetration distance is ~ 2 m.

River DOC also controls how quickly and whether a quasi-steady state size for the DOC plume is achieved. The C_{DOC}=2 mg/L scenarios all reach a steady state by the end of day 7 and this can be seen qualitatively by comparing the extent of the 10% DOC contours between day 4 and day 7, and quantitatively it can be seen in the time series plots of DOC mass over time (Figure 5b). The clearest illustration of river DOC controlling the approach to some steady state (or not) is seen when comparing the C_{R-DOC}=2 mg/L and 12 mg/L scenarios under losing river conditions. These cases show that the extent of the 10% DOC contour does not advance any further between day 4 and day 7, remaining at ~15 m into the riparian zone. At dynamic equilibrium conditions, the reaction rate of DOC via respiration is in balance with the supply of DOC from the river.

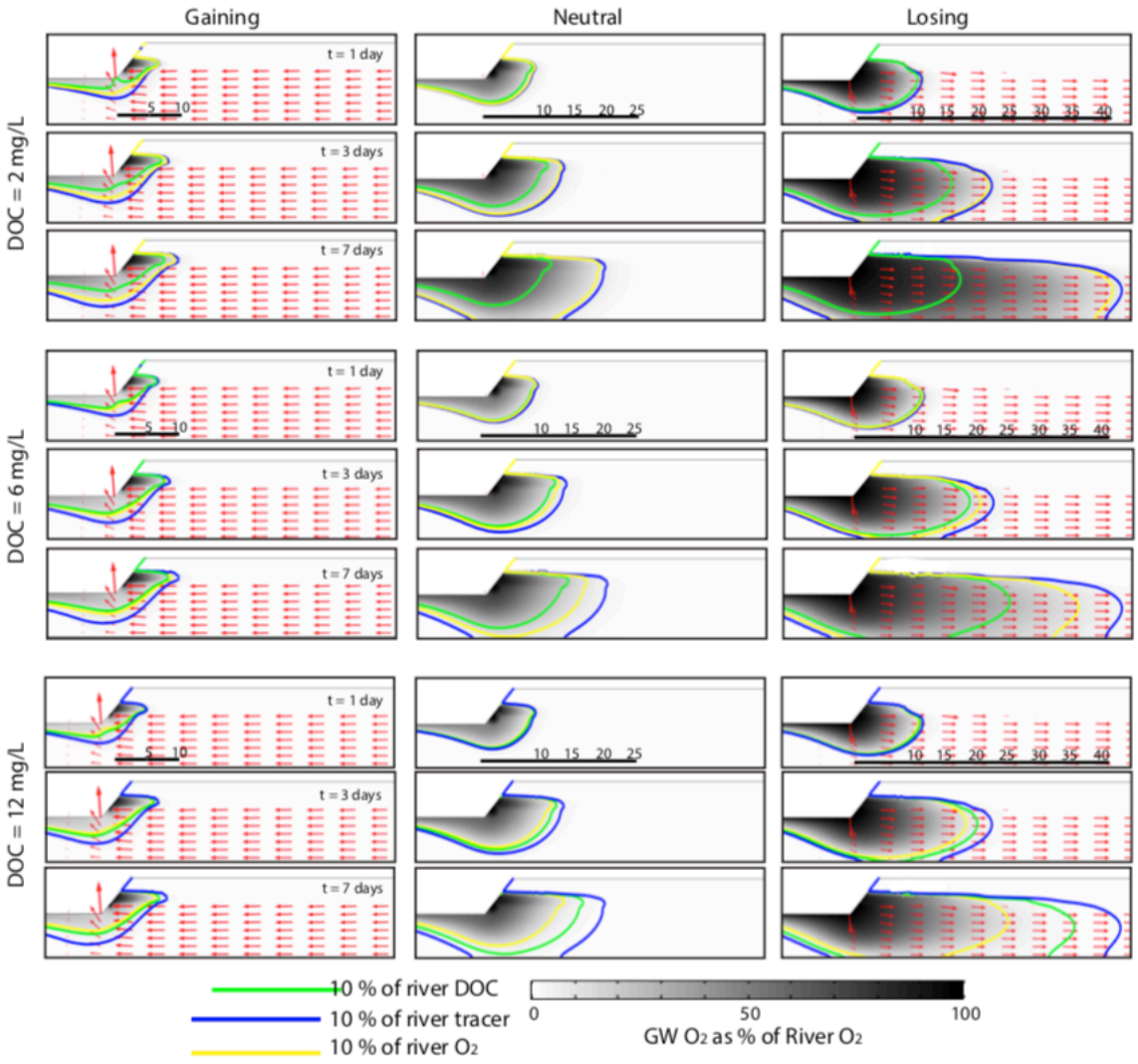

Figure 4.6: Snapshots of DO distribution for varied river DOC and groundwater flow conditions

Snapshots of DO concentration after 1, 3, and 7 days showing the effect of river DOC and groundwater flow condition. These snapshots that correspond to the DOC snapshots in Figure 5. Contours show the extent of 10% concentration relative to the river for DO, DOC, and non-reactive tracer.

When the DOC supply exceeds the respiration rate, the DOC mass (Figure 5b) continues to grow over time as is the case for the losing scenario with C_{DOC}=12 mg/L.

The effect of river DOC concentration on the extent of DO in the riparian zone is shown in Figure 6. When C_{DOC} is less than river DO (9 mg/L or .281 mmol/l), as is the case for the C_{DOC}=2 and 6 mg/L scenarios (0.066 and .2 mmol/L), the oxygenated zone extends beyond the DOC zone because there is DO that remains unused once the DOC is consumed. In the C_{DOC}=2 mg/L scenarios, where the river DOC is much less than DO, the oxygenated area (yellow contour) extends almost as far as the conservative tracer (blue contour). For the C_{DOC}=6 mg/L scenarios, the DO plume still extends beyond the DOC plume but less so than the C_{DOC}=2 mg/L scenarios. The C_{DOC}=12 mg/L (.4 mmol/L) scenarios illustrate that when the DOC concentration exceeds that of the DO (.281 mmol/L), the DOC plume extends beyond the oxygenated zone. When DOC is present but DO has been consumed or is in low concentrations, it would be available to be consumed via anaerobic respiration such as denitrification. Flow fields (red arrows) show the background flow conditions in the intervening time between the daily dam-induced floods. The flow vectors are scaled proportionally to velocity— the losing and gaining conditions are flows of equal magnitudes but opposite directions, while the flow for neutral conditions is comparably non-existent. It can be observed that gaining river conditions push the dissolved species out of the riparian zone, losing conditions continue to bring solutes from the river into the riparian zone, and in the absence of river stage fluctuations, neutral conditions have no ambient flow - most of subsurface flow happens during and shortly following the flood.

4.3.4 Sensitivity of Net 24-Hour Respiration and Mass Return Ratio

4.3.4.1 Varied Dam Release, Ambient Groundwater Flow, and Hydraulic Conductivity

The mass of DOC consumed by aerobic respiration displays clear relationships with all three of the parameters that were tested - dam release duration, ambient groundwater flow conditions, and K (Figure 7a). As the parameter regulating the rate that fluid flows through a porous media under a given gradient, K shows a strong control on the 24-hour mass of DOC respired. For K = 1 m/d, the range across all dam release and groundwater conditions is from 2.6-4.8 g per day, for K = 10 m/d the range increased to 5.7-13 g per day, and for K = 100 m/d the range spans 7.8-59 g per day.

Ambient groundwater flow conditions in the riparian zone also affect the amount of respired DOC. For any given dam release condition and K, there is an increasing trend of DOC mass respired as groundwater gradient goes from positive (gaining) to negative (losing). As K increases, groundwater conditions cause larger ranges in DOC consumption. An example of this effect is the range of DOC consumed for the 8-hr flood scenarios: when K = 1 m/d the range is 3.5-4.8 g, compared to a range from 13.7-60 g for the K = 100 m/d.

The last parameter that was varied was the duration of the dam release. Dam release duration is positively related to DOC respiration; all else being equal (same K and groundwater), longer releases result in more DOC to be consumed.

Besides the DOC mass consumed over a 24-hr period, the ratio of DOC leaving and entering the riparian zone (the ‘mass return ratio’) was assessed (Figure 7b). A ratio closer to 1 indicates that more of the infiltrated DOC returns to the river and is not reacted or sequestered in the riparian zone.

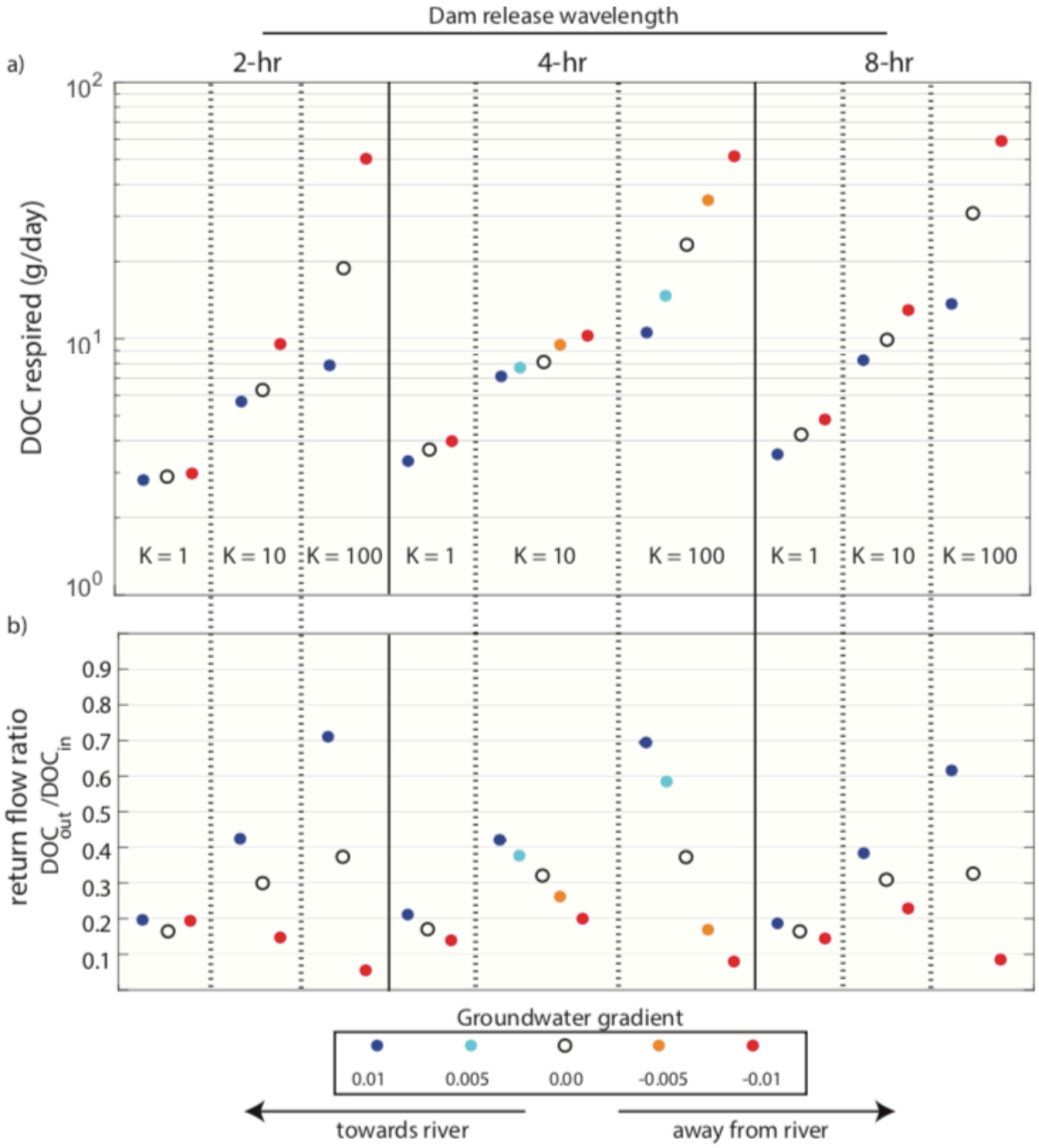

Figure 4.7: Net 24-hour DOC respiration and return flow ratio for varied K, groundwater flow conditions, and dam release durations

Mass of DOC respired per 24-hours, per meter length of channel (a) and the corresponding return flow ratios (b).

The highest ratios occur for gaining conditions and the lowest for losing conditions; neutral conditions resulted in ratios between the high gaining and low losing values. For gaining conditions, the percent DOC returning to the river was as high as 71% (2-hr, K =100 m/d) and as low as 20% for the K = 1 m/day conditions. Gaining conditions showed the largest range of DOC return ratio, with lower K values having smaller proportions of DOC mass returning to the river. Losing conditions had both the lowest return ratio (5.4% for 2-hr and K = 100 m/d) and also the smallest range in return ratios, with the highest percentage return flow being only 22% for 8-hr and K = 100 m/d, making the range from 5-22% for losing conditions. The range for neutral conditions was from 18-37%, with increasing return ratios at higher K values. Unlike K and groundwater conditions, dam release duration did not exhibit much of an influence on the return flow percentage. The three dam release durations caused less than a 7% range in return flow ratio, and support that the more important factors for the return flow ratio are K and the groundwater orientation and flow intensity.

4.3.4.2 Varied River DOC Conditions, Ambient Groundwater Flow, and Hydraulic Conductivity

The effect of different river DOC concentrations on the DOC mass respired was assessed for three DOC values (C_{DOC}=2, 6, and 12 mg/L ; Figure 8a). Three K (1, 10, and 100 m/d) and three ambient groundwater flow conditions (head gradients of -0.01, 0, and 0.01) were considered for each $C_{R\text{-}DOC}$. A 4-hour dam signal (Figure 2b) used for all of the varied DOC scenarios to keep the number of simulations manageable. Not surprisingly, the mass of DOC respired increased with higher C_{DOC}. However, the range in DOC mass respired for the three C_{DOC} values was highly sensitive to K. Across the range of C_{DOC}, the DOC respired for the K = 1 m/d ranges from 1.6-5 g, for K = 10 m/d it

spans 3-18 g, and for K = 100 m/d the range is 6.5-70.8 g. As K becomes larger, the effect of ambient groundwater conditions becomes more significant on the range in respired DOC. For K = 1 m/d, the different groundwater conditions result in a maximum difference between losing and gaining conditions of only 1 gram respired (for the C_{DOC}=12 mg/L scenario), while for the K = 100 m/d, the C_{DOC}=12 mg/L scenario results show a range of ~55 g depending on the groundwater conditions. Finally, the effect of C_{DOC} on the mass respired also becomes more important as K increases. For K = 1 m/d, the mass respired for C_{DOC}=2 mg/L ranges from 1.6-1.65 g and for C_{DOC}=12 mg/L it ranges from 3.1-4.4 g, for K = 10 m/d the range for C_{DOC}=2 mg/L is 3-4.4 g and for C_{DOC}=12 mg/L is 9.8-16 g, and for K = 100, the C_{DOC}=2 mg/L case has mass respired which varies from 5.4-19.6 g and for C_{DOC}=12 mg/L, it ranged 13-70 g.

The effect of C_{DOC} on the DOC mass return ratio was also quantified (Figure 8b). The percentage of DOC returning to the river is larger as C_{DOC} increases. This is indicated by the positive slopes for all groups of ambient groundwater conditions (each color group) within each K range in Figure 8b. The effect of C_{DOC} on the mass return ratio is also more sensitive to the gaining and neutral groundwater conditions than the losing condition. Across all of C_{DOC} simulations the mass return ratio ranges from as low as 7 % to as high as 76%. The lowest values are present for all groundwater conditions at the lowest DOC concentration (2 mg/l) with the lowest K (1 m/d) or, interestingly for the all DOC concentrations for the losing condition and K = 100 m/d). The low ratio for these scenarios indicate that 10% or less of the DOC that enters the riparian zone flows back into the river. The largest ratios are for the gaining conditions and increase with DOC and K. For example, when K = 1 m/d the three DOC values result in ratios for gaining conditions ranging from 12-28%, but when K = 100 m/d the DOC values have ratios of 60-76%.

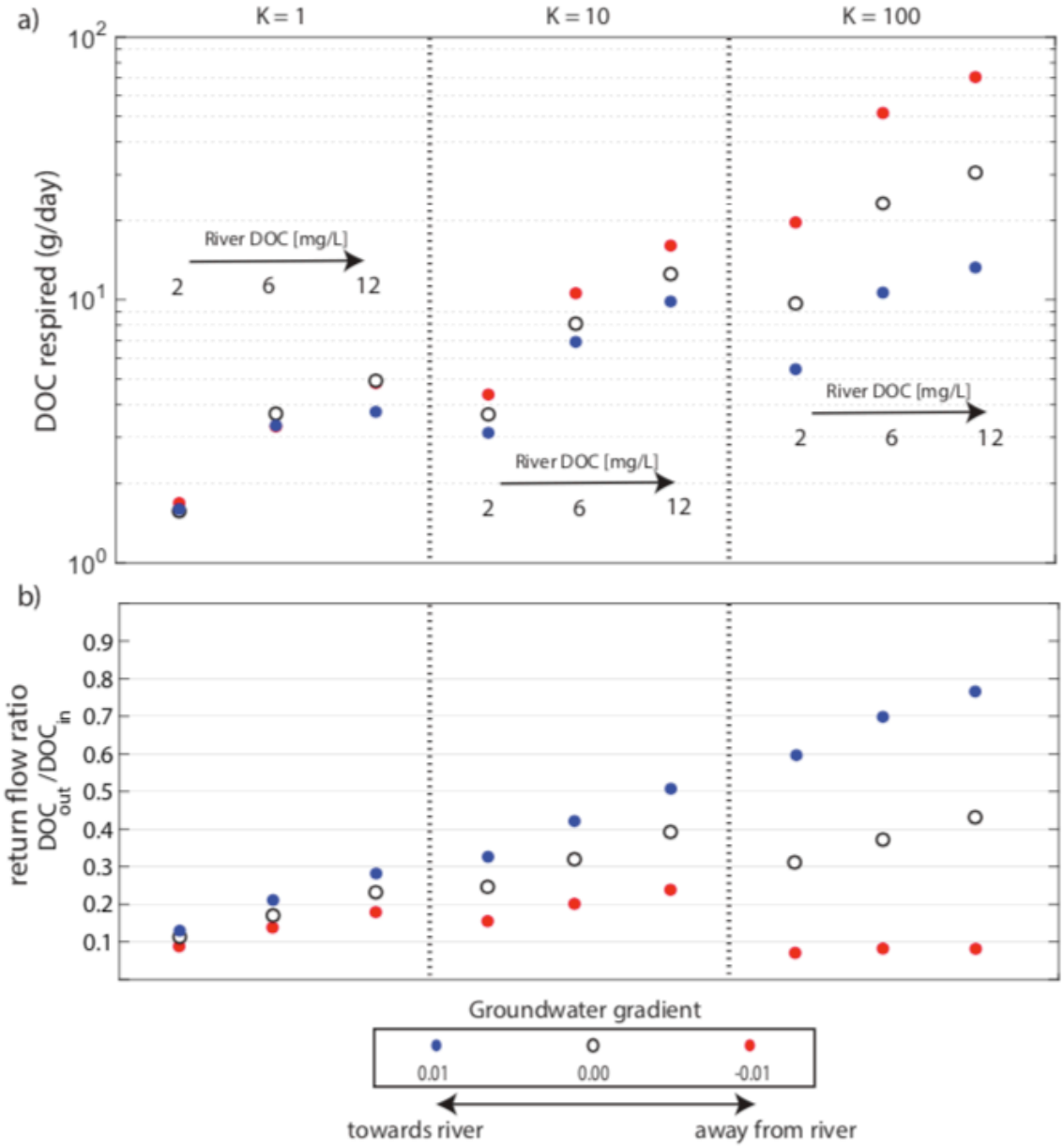

Figure 4.8: Net 24-hour DOC respiration and return flow ratio for varied river DOC, K, and groundwater flow conditions

Mass of DOC respired per 24-hours, per meter length of channel (a) and the corresponding return flow ratios (b).

These results show that C_{DOC} can significantly change the ratio of DOC returning to the river, that the effect of C_{DOC} on the mass return ratio is greater for gaining and neutral conditions than for losing, and that the ratios are more tightly clustered at lower K values.

4.4 DISCUSSION

4.4.1 Insights from Reactive Transport Model Results

The snapshots demonstrate how properties of the riparian zone (K, ambient groundwater flow) and of the river (DOC concentration) influence the spatiotemporal evolution of DOC and DO in the riparian zone. They show that the size of the DOC plume and total mass of DOC accumulated in the riparian zone is controlled by both hydraulic properties and the reaction rate. These results are complemented by the 24-hr DOC uptake rate and also the DOC mass return ratio.

The snapshots illustrate that K plays the dual role of influencing the size of the respiration zone and also modulating the effect ambient groundwater flow directionality has (Figure 3). The reason that K is an influential metric for all components of this study is that it is the master variable controlling the velocity that water (and solutes) moves through the subsurface. Thus, K controls the mass of DOC and other solutes enter the riparian zone and also how quickly those constituents move in the subsurface. The balance between the rate that DOC travels ('mass-transport') and the reaction kinetics, dictates the distance the DOC can travel in the riparian zone before being consumed. It explains why the spatial extent of DOC is strongly controlled by K. When the K of the riparian zone is low, little DOC and other solutes enter the sediment, and once in the subsurface, move at slow rates and can be fully reacted before traveling much distance

into the riparian zone. The DOC distribution is more extensive at higher K's because the DOC transits through the riparian sediments faster relative to the reaction rate.

The influence of ambient groundwater flow creates increasingly different outcomes as K becomes larger (Figures 3, 7, 8). This can be understood by the linear relationship between hydraulic gradient, K, and flow velocity described by Darcy's law. For the same gradient, a K of 100 m/d results in 100 times higher flow velocities than a K of 1 m/d. This relationship also explains why at higher Ks different ambient groundwater flow conditions result in much larger differences in the DOC distribution (Figure 3) and also total consumed DOC (Figures 7,8). Take the end-member ambient groundwater conditions of flow towards (gaining) and flow away from the river (losing). For a K of 1 m/d and head gradients of 0.01 and -0.01, the seepage velocity at background conditions is just 3.3 cm/day, either away or towards the river. For K = 100 m/d, the same losing and gaining conditions result in a flow rate of 3.3 m per day in either direction whether towards or away from the river. This explains why the results from the snapshots for K = 1 m/d are all quite similar, while the ones for K = 100 m/d are vastly different. An interesting conclusion from this is that the ambient groundwater condition becomes increasingly important for controlling the aerobic respiration extent in riparian zones as K increases. Thus, the seasonality of ambient groundwater conditions in riparian zones [Burt et al., 2002; Duval and Hill, 2006] becomes increasingly important as K increases, and by contrast is comparably less important for riparian zones composed of finer grained, low K, sediments.

Besides the properties of the riparian zone (K and GW flow), the extent that river-sourced DOC and DO travel into the riparian zone is also controlled by the concentration of DOC and DO in the river. In this study the effect of different C_{DOC} values ranging from 2 to 12 mg/L was explored, while DO was held constant at 9 mg/L (saturation at 20

°C). Aerobic respiration requires both DOC and DO, and thus if they are not present in equal amounts, the reaction is limited by whichever species is lower in concentration. This is an important consideration when interpreting the results from the snapshots (Figure 3 - Figure 6) as well as the summary plots (Figures 7 and 8). For the snapshots showing the effect of K and ambient groundwater flow (Figure 3), DOC was the limiting reactant (C_{DOC}= 6 mg/L and DO = 9 mg/L), and therefore there was always enough oxygen to allow for the consumption of the DOC, and this is why the mass in the riparian zone achieved a steady state by seven days. The excess of oxygen can be seen in the DO snapshots (Figure 4), where the DO extends beyond the DOC contour. The larger the difference between the two species, such as in the case of DOC = 2 mg/L and DO = 9 mg/L, the further the oxygenated zone extends beyond the DOC as a large portion of the DO is not consumed in the aerobic respiration of DOC. The opposite occurs when the DOC is in greater abundance than DO such as the C_{DOC}= 12 mg/L and DO = 9 mg/L. Under these conditions DOC remains after DO has been depleted. This would enable the remaining river-sourced DOC to be used for anaerobic respiration such as denitrification. Because the DO and DOC travel in the subsurface, as discussed above, the spatiotemporal evolution of their distribution is controlled by K and GW conditions. When their concentrations are not equal, there will be larger differences in their position relative to one another when the riparian zone is composed of higher K sediments and if it has neutral or losing flow conditions.

4.4.2 Limitations and Future Directions

The simulations presented in this study simplify the complex environments of natural rivers and their riparian zones. They were designed to provide examples of how K, ambient groundwater flow, and river DOC concentration influence respiration. A host

of important processes and factors exist that were omitted to constrain the scope of the study and to be able to focus on specific controls. Such excluded factors include (but are not limited to): more sophisticated and realistic microbial processes, sorption of DOC onto riparian zone sediment, the effect of variable temperature on DO concentration and microbial respiration rates, and the presence of background DOC and particulate organic carbon in the riparian zone. Each of these factors would influence the spatial distribution and DOC and DO and the rate of DOC consumption.

Microbial processes can introduce numerous effects relevant to subsurface DOC transport and metabolization. One example is the feedback between nutrient supply (DOC transport) and microbial biofilm growth, which commonly occurs in riverbed sediments [Battin et al., 2016]. Over time, microbial growth can result in bioclogging of the pore spaces, causing decreases in sediment K of multiple orders of magnitude [Aubeneau et al., 2016; Thullner et al., 2002; Xian et al., 2019]. Incorporating the effect of biofilm growth on K would influence the results of this study, and is an effect that could be incorporated into future studies. Another example of microbial processes is the effect that DOC quality has on reaction rates. In this model, all of the DOC was considered to be reactive or 'labile' and the Monod framework had one set of parameters for DOC. In reality, there are thousands of types of DOC present in river and riparian waters, and these different DOC types have a wide range of reactivity [Maurice et al., 2002]. State of the art models under development seek to incorporate organic matter thermodynamics into organic matter specific reaction kinetics that represent the actual chemical composition of organic matter in waters - thermodynamically favorable OM having higher respiration rates [Song et al., 2020].

Other factors that could influence DOC dynamics are sorption, sources of DOC in the riparian zone other than from the river, and temperature of river water and riparian

sediments. Sorption of DOC on sediment surfaces could play a significant role in attenuating the movement of DOC from the river into the riparian zone [Fiebig and Marxsen, 1992; McDowell, 1985; McKnight et al., 1992]. Another complexity that we did not include was particulate organic carbon (POC) in the riparian zone as a source of DOC. POC is often present in riparian sediments and its distribution can exhibit spatial variability [Hill et al., 2004; Gurwick et al., 2008; Sobczak et al., 1998]. Interestingly, Sobczak et al., 1998 found that POC in riparian sediment was a predictor of both bacterial productivity and biomass. Temperature is an important parameter as it influences both microbial activity (and in turn DOC consumption) and also the DO saturation of the river water. Besides water temperature, other factors that influence the amount of DO in rivers include light, sediment load, biogeochemical reactions, and biomass. [Bernhardt et al., 2018]. The effect of temperature on reaction rates was incorporated into reactive transport models by Sharma et al. (2012) and Song et al. (2018) who investigated carbon and nitrogen reactivity in riparian zones. Sharma et al. (2012) found that incorporating seasonal temperature changes was key for modeled oxygen and nitrogen concentrations in the riparian zone to match field observations.

4.5 CONCLUSIONS

The goal of this study was to provide insight into controls on exchange flow-driven aerobic respiration in the riparian zones in dynamic rivers (i.e. dammed or tidal). This study used reactive transport modeling to conduct virtual experiments designed to assess the effect of daily river fluctuations on aerobic respiration of river-sourced DOC and DO in the riparian zone. A suite of 50 simulations was undertaken to test how riparian zone properties (hydraulic conductivity and ambient groundwater flow conditions) and river properties (DOC concentration and dam release duration) influence

the spatiotemporal evolution of DOC and DO in the riparian zone. K was found to be a strong control on the lateral extent that river-sourced DOC and DO can travel into the bank, and on the total amount of DOC respired. It was found that at low K, groundwater flow conditions had little influence on the overall size of the DOC hot-spot or on the amount of DOC consumed via aerobic respiration. As K increases, gaining versus losing conditions create increasingly different outcomes in the lateral extent of the river-sourced DOC and DO in the riparian zone and also in the amount of DOC mass respired. The concentration of DOC in the river had a positive relationship both the amount of DOC respired and the return flow ratio, with higher DOC concentrations resulting in more mass of DOC consumed, but in more DOC returning to the river. Longer flood durations resulted in more DOC respired and less DOC returning to the river (lower return ratio). Flood duration had a larger effect on the total DOC mass consumed than on than the return ratio. Our results illustrate that the role of riparian zones as filters for daily exchange flows is heavily dependent on K, GW orientation, and the chemistry of the river (DOC and DO conditions). These results support that the function of the riparian zone for controlling nutrient fluxes in dynamic rivers is expected to vary substantially based on sediment composition (control on K), groundwater flow directionality and intensity, and the chemistry of the river.

Finally, a promising research direction would be to assess the response of respiration hotspots over a longitudinal distance either with a fully coupled framework (Zhou et al., 2018; Shuai et al., 2019) or the one-way coupled approach of Ferencz et al. (2019). The advancements from such a study would be twofold. First, it would reveal how the function of riparian zones as respiration hotspots changes with proximity from a dam. The second, and arguably higher-impact, finding from such an analysis would to integrate the amount of DOC respiration over a distance of tens or hundreds of

kilometers. This would provide river-scale estimates for the potential scale of DOC respiration in dynamic rivers, such as dammed or tidal environments. Such an estimate would help contextualize the contribution of high-frequency flow variations in dammed rivers to eco-system carbon fluxes.

Chapter 5: Diel Stream Temperature Regimes in the Conterminous United States [1,2]

ABSTRACT

Stream temperature, which varies over daily to seasonal timescales is a primary control on myriad ecological, biogeochemical and physical processes. Yet geographic patterns of its diurnal variations have not been fully characterized. Using daily temperature records spanning 15 years (2000-2014), monthly-averaged mean daily temperature and diurnal temperature range were calculated for streams distributed across six Bukovsky eco-regions of the conterminous US. Across all six eco-regions, diurnal temperature fluctuations were lowest during the winter, around 1-2 °C. During the summer there was wide distribution in diurnal temperatures (2°C–12°C). The eco-regions revealed distinct differences in diurnal patterns for small (< 100 cfs) and medium streams (>100 & <1,000 cfs), but not for large streams (>1,000 cfs). Small and medium streams exhibited notable hysteresis in their annual progression of diurnal temperature ranges, with larger diurnal temperature fluctuations in the spring than in the fall.

[1]Ferencz, S. B., and Cardenas, M. B. (2017), Diel stream temperature regimes of Bukovsky regions of the conterminous United States, *Geophys. Res. Lett.*, 44, 2264–2271, doi:10.1002/2017GL072641.

[2] Stephen Ferencz was the main contributor who performed the research, analyzed the data, and wrote the manuscript

5.1 INTRODUCTION

Stream temperature follows both annual and diurnal cycles of warming and cooling. The observed temperatures reflect the dynamic balance between the inputs and outputs of energy to and from the stream system. The key inputs of energy to rivers come from shortwave solar radiation, longwave radiation, evaporative cooling (latent heat), and groundwater inflows [*Poole and Berman*, 2001]. Annual cycles of mean daily temperature (MDT) result from the long-term energy balance (net warming versus net cooling), while annual cycles of diurnal temperature range (DTR) occur due to changes in the conditions that control the short-term (24-hour) energy balance. MDT and DTR vary annually in response to changes in solar radiation, climate, and vegetation [*Caissie*, 2006].

Changes in mean stream temperature mirror the changes in mean air temperature over seasonal time scales [*Sinokrot and Stefan*, 1993]. Like air temperature, stream temperatures are at a minimum in the winter and at a maximum in the summer. There has not yet been a convenient relationship like air temperature identified to estimate the spatial and temporal behavior of DTR. DTR is dependent on many factors, including: diurnal air temperature fluctuations, solar radiation, cloud cover, shading from vegetation, humidity, stream flow, groundwater inputs, and channel morphology [*Webb et al*., 2008]. In addition to the many natural environmental variables to consider, human-influences such as dams and water inputs from sources such as power plants and wastewater outflows also can influence the DTR and mean temperature conditions in

streams [*Caissie*, 2006]. It is thus challenging to accurately predict the annual diurnal behavior for a stream because it is necessary to quantify these parameters along a reach and understand their variation over time. While the existence of spatial and seasonal variation in diurnal temperatures of streams was recognized over 50 years ago, there have been few studies on the topic since these initial observations [*Yakuwa* 1960; *Edington* 1965]. The studies that have looked into the spatial and temporal variation in diurnal temperatures have only been done at the local scale at well-instrumented field sites [*Ward*, 1985; *Sinokrot and Stefan*, 1993; *Webb and Walling*, 1993; *Webb and Zhang*, 1997; *Caissie et al.*, 2001].

Many physical, chemical, and biological properties and processes depend on water temperature [*Poole and Berman*, 2001], such as dissolved oxygen and solubility of other gases [*Ducharne*, 2008], metabolic activity [*Caissie*, 2006], and nutrient [*Nimick et al*., 2011; *Zheng et al*., 2016] and metal distribution and cycling [*Gammons et al.*, 2014]. Both annual and diurnal variations of water temperatures have been found to be important determinants for the distribution of aquatic species [*Caissie*, 2006], and also influence growth rate and development [*Elliott and Hurley*, 1997]. The diurnal behavior of a stream may influence biodiversity and create windows of metabolic activity for different aquatic organisms. Streams that experience large diurnal temperature fluctuations have favorable temperature ranges for a wider variety of organisms than for streams that have little variance [*Vannote et al*., 1980]. As temperature fluctuates around a mean daily value, populations of organisms may decrease or increase their metabolism depending on their preferred thermal regime [*Vannote et al*., 1980].

Because of the significant role temperature plays in ecosystem function, extensive research has been done to understand and quantify the mechanisms that control stream temperature. However, studies that have sought to characterize and predict stream

temperature at the regional scale [*Mohseni and Stefan*, 1999; *Caldwell et al*., 2012; *Hill and Hawkins*, 2013; *DeWeber and Wagner*, 2014; *Segura et al., 2015*; *Isaak et al., 2016*] have typically ignored diurnal variation. Thus, the objectives of this study are to: (1) document the spatial distribution and temporal behavior of stream DTR across the conterminous United States (CONUS) using long-term daily stream temperature records, (2) compare the annual progression of stream DTR and stream MDT between Bukovsky eco-regions [*Bukovsky*, 2012], and (3) to determine how DTR varies across different ranges of stream discharge.

5.2 Data and Methodology

Temperature records were obtained from the U.S. Geological Survey National Water Information System website. Daily temperature data was gathered from all available gauging stations in the conterminous United States (CONUS) from 2000-2014. The mean stream temperature data is based on averaged measurements that were recorded from 15-min to hourly intervals and the daily DTR was calculated by differencing the observed daily maximum and minimum. The data was filtered to only include measurements validated by the USGS and to remove sparse, unrepresentative datasets. To ensure that the monthly averages reflected representative conditions at each site, monthly temperature records were filtered to include only those that had data for at least 75% of the days in a given month. This cutoff is more conservative than that used for mean temperature studies of streams across the CONUS (66% cutoff) by *Hill and Hawkins* [2012] and in the Pacific Northwest by *Arismendi et al.* [2012] (no minimum requirement). Unlike discharge data, temperature data for USGS gauging stations can be sparse. Many stations only report data for certain months of the year and there can be gaps in the data for the months that are available. To provide confidence that the

observations presented in this study are representative of longer-term characteristic behavior, only gauging stations that had at least five years of representative monthly records were used.

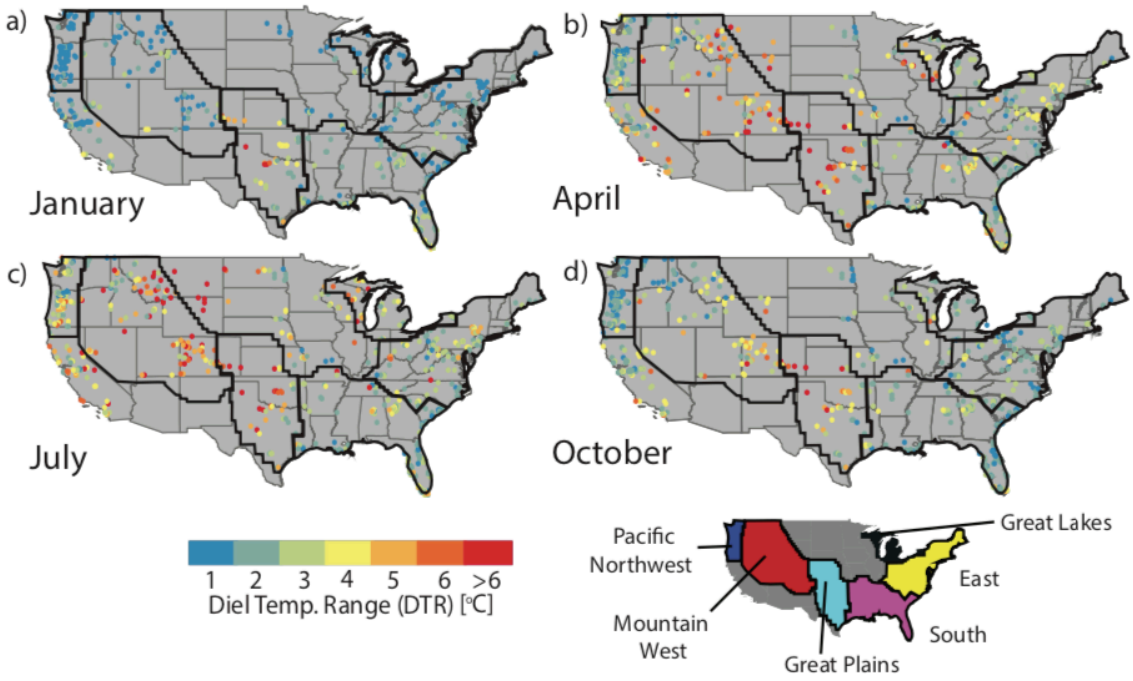

Figure 5.1: Seasonal diel temperature range maps

Maps of monthly DTR for months representing each season. Eco-region boundaries are outlined in black. Stations used for these maps had at least 5 years of representative (>75% days/month) data. Histograms summarizing the data for the DTR maps are provided in Figure S1.

In addition to temperature data, average daily discharge was obtained for the gauging stations as well. Discharge was used to categorize the streams by average annual flow rate expressed in cubic feet per second (cfs). Streams were grouped into three categories: less than 100 cfs (small), 100 to 1,000 cfs (medium), and greater than 1,000

cfs (large). Stream discharge was also used to provide a comparison between seasonal changes in discharge and changes in DTR within the six Bukovsky eco-regions. Of particular interest was whether seasonal low flows, or conversely periods of high flows, within ecoregions coincided with changes in DTR. Low flows have the potential to make streams more susceptible to larger temperature changes [*Poole and Berman,* 2001*; Caisse et al*., 2006]. During periods of low flow there is less thermal mass and, depending on the channel morphology, there can be a higher surface area to volume ratio for energy exchange across the air-water interface [*Poole and Berman*, 2001]. Monthly flow values for each site were calculated by averaging daily flow data using a trimmed mean, removing the largest 15% of the flow data. This approach was chosen to prevent transient flow events such as floods from skewing calculated mean discharge rates.

To reduce the potential effect of upstream dam releases and inputs (power plant & wastewater effluent), sites that were less than 15 km downstream from these sources were excluded. *Webb and Walling* [1996] found that dam releases can reduce diurnal fluctuations, shrink the annual mean temperature range, and shift the timing of peak mean temperature. While the influence of inputs from power plants and wastewater treatment plants is likely less than that of dam releases, they are regarded as sources of thermal pollution can locally alter the thermal regime of a stream [*Caisse*, 2006]. The identification of upstream sources and distances between sources and gauging stations was performed in ArcGIS. Figure S-3 and S-4 are plots of the annual ranges of MDT and summer (July) DTR plotted against downstream distance from sources. These plots show that the cutoff distance of 15 km was a reasonable and conservative cutoff distance for excluding sites.

A regionalized approach was used to compare annual changes in MDT, DTR, and discharge between different eco-regions within the CONUS. Based on the available

coverage of gauging stations, the following regions were chosen for analysis: Pacific Northwest, Mountain West, Central Plains, Great Lakes, South, and Northeast (Figure 2d). These regions are a simplification of the terrestrial eco-regions assigned in *Ricketts et al*. [1999], and were developed for NARCCAP models by *Bukovsky* [2012]. Eco-regions, by definition, delineate zones of similar climate; at the coarse scale used for this study, these boundaries are based on seasonal temperature and precipitation patterns. Additionally, *Berghuijs* et al., [2014] found that annual streamflow patterns and water budgets for 321 catchments across the CONUS could be grouped by similar seasonal patterns in aridity index, timing of precipitation, runoff ratio, and fraction of precipitation as snowmelt that closely mirror the eco-region boundaries developed by *Bukovsky* [2012]. Because vegetation patterns are influenced by climate, eco-regions also represent areas with different vegetation types and capture seasonal changes in vegetation. In Table S2 we provide a statistical analysis of the standard deviation of both DTR and MDT data relative to means within each region. Our analysis shows that the average annual standard deviation for both MDT and DTR compared to regional mean values for these two parameters are smallest within ecoregions, which support ecoregions grouping areas of similar temperature behavior. Our approach for this analysis is outlined in detail in the Supplementary Materials.

5.3 Results and Discussion

Diurnal stream temperature maps for January (winter), April (spring), July (summer) and September (fall) are shown in Figure 5.1. Mid-season months were chosen rather than seasonal averages to provide the largest contrasts in DTR and to accentuate regional differences. DTR is at a minimum in the winter (Figure 5.1a) with most sites having a DTR of 1-2 °C, the Central Plains being the exception where large DTRs are

present even during the winter months. In summer (Figure 5.1c), the DTR is largest in the Mountain West and Plains regions with many of the locations having a DTR of at least 5 °C, while the DTR in the Eastern US shows much less change from the April (spring) values.

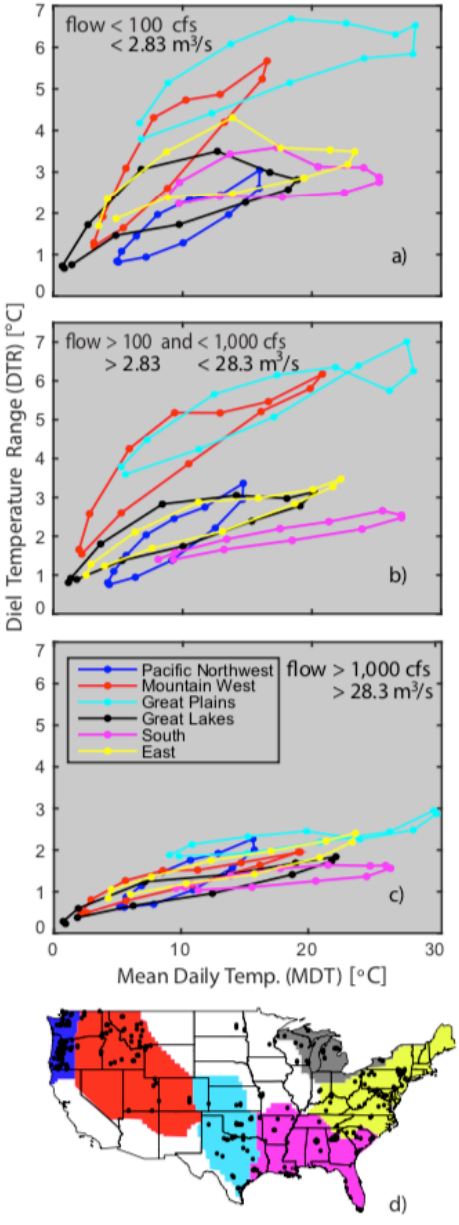

Figure 5.2: Regionally averaged diurnal temperature range (DTR)-mean daily temperature (MDT) cycles

Diurnal temperature range (DTR)-mean daily temperature (MDT) cycles. Average monthly DTR and MDT represent the annual cycles of mean temperature and diurnal range within the six regions for streams with average annual discharges of < 100 cfs (a), 100-1,000 cfs (b), and > 1,000 cfs (c). The temperature cycles are read from the lower left in a clockwise fashion. The seasons can be generalized by winter months in the far left of each plot, summer months in the far right, and spring and fall months forming the tops and bottoms of each of the loops. Monthly values are shown by circles and are connected to form the annual cycles.

Comparing the maps for April (Figure 5.1b) and October (Figure 5.1d), it can be seen across the CONUS that DTR's are generally lower in the fall than in the spring. These observations are supported by histograms of the seasonal data included in Figure S1 that show the distribution of DTR's for each season and for each of the three discharge ranges.

Figures 5.2a-c show the monthly progression of DTR plotted against MDT for streams of the three different discharge classifications in each of the six eco-regions. To maintain comparability of the annual changes in DTR and MDT across the six eco-regions, the sites whose data was used for Figure 5.2 had at least five years of coinciding monthly DTR and MDT temperature records for all 12 months of the year. Due to this more stringent requirement, sites used for the DTR-MDT temperature cycle plots (Figure 5.2d) are a subset of those presented in the DTR maps shown in Figure 5.1. The monthly DTR and MDT data for each of the locations used for Figures 5.2 is plotted in scatter form in Figure S2. The scatter plots show that small and medium streams sites within each eco-region tend to reside in discrete MDT-DTR regimes. The clustering is quite distinct for winter, spring, and fall. During summer, some overlapping between eco-regions is present. However, the regional differences that are apparent for small and medium streams start to break down for large streams (> 1,000 cfs). Unlike small and medium streams, which show significant differences throughout much of the year in both

DTR and MDT, the only statistically significant difference in thermal regime for large streams is their MDTs (Table S1).

The DTR-MDT plots in Figure 5.2 illustrate the average annual behavior of both the long-term (MDT) and short-term (DTR) temperature conditions within each eco-region. The DTR-MDT loops are based on composited averages in both time and space and do not represent the thermal conditions at all sites. Instead, they are meant to illustrate tendencies of the annual changes in the DTR-MDT thermal regimes across the six eco-regions. The hysteretic behavior of DTR can be seen more clearly in the DTR-MDT plots (Figure 5.2) than in the DTR maps in Figure 5.1. The hysteresis is most pronounced in the small flow streams (Figure 5.2a) and diminishes with increasing flow (Figure 5.2b and 5.2c). *Webb and Walling* [1993] used similar DTR-MDT plots to show the annual temperature behavior of a small stream in the UK over a 14-year period, and also observed the same seasonal hysteresis. Monthly discharge data for each site show that across all regions discharge is typically lower in the fall than in the spring (Figure 5.3). The trend in discharge suggests that seasonal differences in flow conditions may not be a primary control on the observed hysteresis because low flows should increase susceptibility to diurnal warming and cooling [*Poole and Berman,* 2001].

Monthly DTR and discharge data for the sites used for the DTR-MDT plots in Figure 5.2 are presented in Figure 5.3. To allow for comparisons to be made for how proportional changes in DTR relate to proportional changes in discharge, monthly DTR and discharge values for each site were normalized using the average annual values for each site (Figures 5.3a-c). In the Northeast, Great Lakes, South, and Pacific Northwest, the timing of peak discharge occurs in the spring which results from the combined effect of snow melt and precipitation. These four regions show marked increases in discharge during the transition from winter to spring (February – April) which decline throughout

the summer, reaching their lowest annual flows in the late summer and early fall (August – September). The discharge patterns for Mountain West streams show a clear signature of seasonal snow melt, with much higher discharges during April-July than during the rest of the year, and have the largest annual variability. The discharge patterns in the Central Plains are similar to that of the Mountain West but with smaller annual variability.

In general, the normalized DTR data presented in Figure 5.3a-c show that DTR patterns within eco-regions exhibit remarkable coherency, in both timing and magnitude, for how large of areas the ecoregions encompass. Non-normalized versions of monthly DTR plots are included in Figure S6. Comparing annual changes in DTR and annual changes in discharge, the seasonal DTR patterns across stream size and regions appears relatively insensitive to changes in discharge; that is, the large seasonal asymmetry in discharge is not apparent in the DTR data. Interestingly, the timing of peak DTR for small streams in the spring for the Northeast, Great Lakes, and South regions coincides with the period of highest discharge. The two regions where periods of high flow coincide with reduction is DTR are the Mountain West and Central Plains. In these two regions large increases in discharge during the late spring and summer coincide with noticeable, yet subtle, depressions in DTR. However, these comparatively large changes in discharge only result in small changes DTR – suggesting that while discharge may influence DTR, local conditions (shading, land cover type, channel morphology, local climate etc.) may influence DTR behavior more than flow conditions.

Both the DTR-MDT temperature cycles (Figure 5.2) and normalized monthly DTR data for all sites (Figure 5.3) show that DTR is at a minimum during the winter months, and, with the exception of small (<100 cfs) streams in the Central Plains and Eastern US (Great Lakes, Northeast, South), typically increases throughout the spring and

into the summer. After reaching a peak in July and August, which is also when peak MDTs tend to occur, DTR declines during the fall and into the winter across all of the regions.

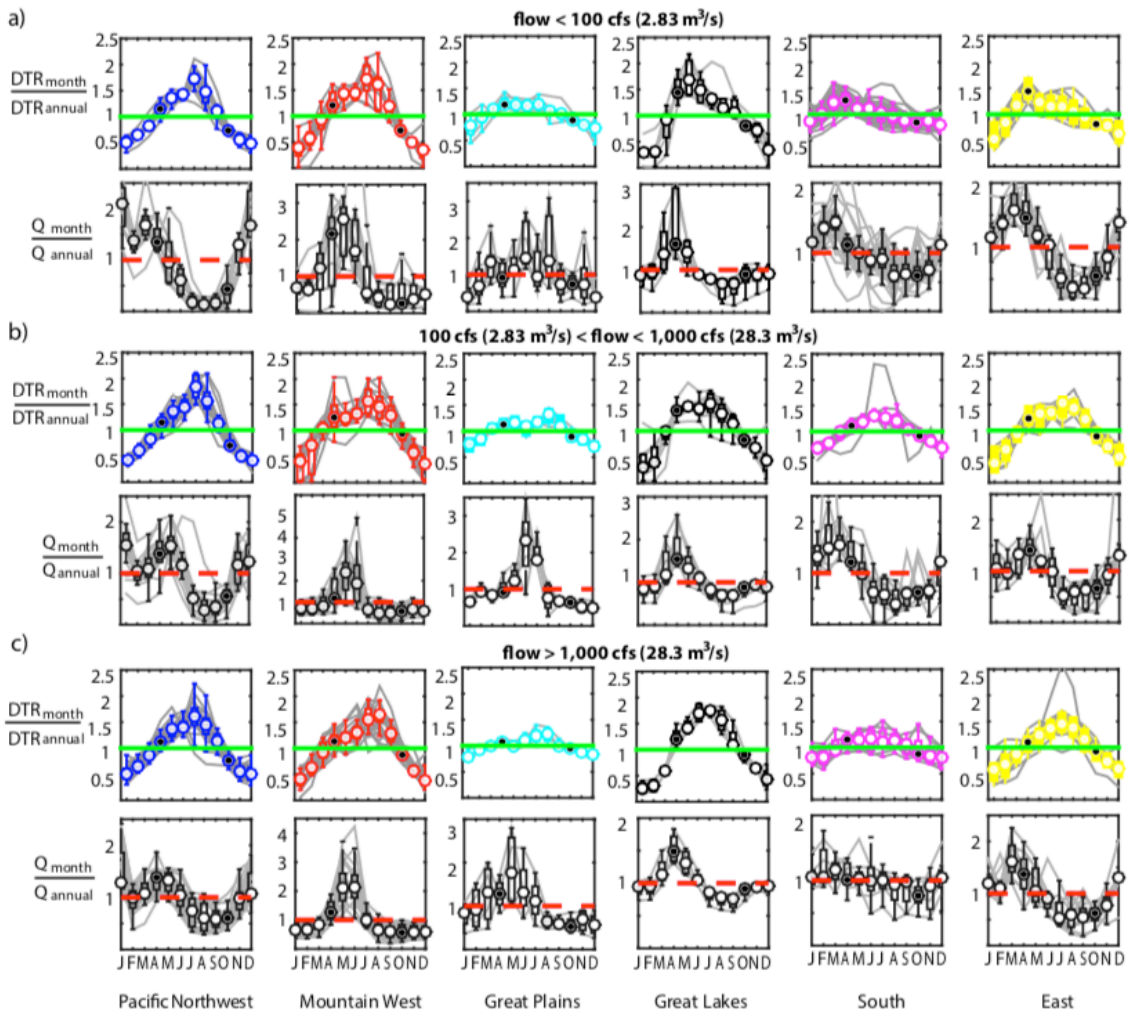

Figure 5.3: Summary plots of month discharge and diel temperature range data

Normalized monthly diurnal temperature range (DTR) and discharge for the three stream size groups: <100 cfs (a), 100-1,000 cfs (b), and > 1,000 cfs (c). DTR data is plotted in color and discharge in plotted in black. Monthly DTR and discharge for each gauging station plotted in light gray. Box plots superimposed on top of time series plots to show the distribution of DTR and discharge data. The top and bottom of the boxes represent the 25th and 75th percentile range and the circles indicate the median value. The green and dashed red lines are provided as a reference for when DTR and discharge are above and below the annual average

values. To highlight the hysteretic nature of the DTR patterns the months of April and October are filled with black circles. One can see the October DTR values are typically lower than the April DTR values. Because the DTR and discharge data is normalized the axes scale indicates the value relative to the annual mean; a value of 3 means the parameter is three times larger than the annual average, while a value of .5 means half the annual average.

The annual trend in DTR (lowest in the winter, highest in the summer) makes sense given that the largest component of energy input to streams typically comes from solar radiation [*Morin and Couillard,* 1990], which follows this same annual pattern (see maps produced by the National Renewable Energy Laboratory) and is the driver for the annual MDT patterns.

Annual DTR patterns in the Pacific Northwest and Mountain West follow the behavior described by *Caissie et al.* [2001], with little diurnal variation in the winter months and the largest variations in DTR during the summer months. Summer maximums in DTR are attributed to a number of factors (e.g., water depth, cloud cover, solar radiation, and low flows). However, not all of the annual DTR patterns in the other four regions follow the expected annual trend for DTR. The departures fall into two groups. The first group being small (<100 cfs) streams in the Eastern US (Great Lakes, Northeast, and South), which tend to have their diurnal maximum during the spring instead of the summer (Figure 5.3a). Two potential reasons for this observed pattern could be the absence of deciduous vegetation during the spring that is present in the summer and also differences in air temperature DTR between these two seasons. Deciduous vegetation, in particular trees that provide canopy cover, increases riparian shading for these small streams. *Sun et al.* [2006] found that in the Eastern US diurnal air temperature fluctuation is much lower in the summer than in either the spring or fall. An implication of small daily air temperature variation is that nighttime lows may be relatively close in temperature to stream water temperatures, reducing the amount of

nighttime cooling that can occur. The second group is all stream sizes in the Central Plains, whose DTR patterns show little annual variation. This is surprising because there are still large annual changes to incident solar radiation (NREL maps). A contributing factor may be air temperature DTR, which remains high in the Central Plains throughout the year [*Sun et al*., 2006]. Compared to the other regions, the Mountain West and the Plains experience larger daily air temperature fluctuations [*Sun et al., 2006*], receive more solar radiation (NREL maps), and may have less riparian shading because these regions have much lower vegetation indices [*Sun et al., 2006*] – all of which would favor larger DTRs.

5.4 CONCLUSIONS

Our findings show that streams not only experience large but systematic seasonal changes in mean temperature, but can also have large systematic changes in diurnal temperature conditions. The differences in the timing and magnitude of DTR across the six eco-regions suggest that some of the key factors influencing diurnal behavior are solar radiation, diurnal air temperature fluctuation, and riparian shading. In general, as stream discharge increases the seasonal temperature cycles show less hysteresis. The hysteresis in DTR means that there is more diurnal fluctuation when streams are warming in the spring than when they are cooling in the fall, the underlying mechanisms for this observed phenomenon are still an open question. It has been previously hypothesized that DTR is low for small streams [*Vannote* et al., 1980; *Caissie* 2006]. In contrast to this idea, the lowest discharge (<100 cfs) streams in this study actually showed the largest average DTR; but few of the < 100 cfs streams had average annual discharges below 10 cfs.

Regional differences in the annual diurnal temperature behavior of streams may influence patterns of biodiversity, phenology, ecosystem metabolism, and rates of nutrient consumption and metal cycling. Thus, an interesting avenue for further research is to compare differences in timing and nutrient consumption capacity for streams that share similar MDTs but have a range of DTRs. Another potential research direction would be to incorporate land cover data, channel morphology, and local air temperature data to see if the inclusion of these additional factors can parse out differences in DTR behavior within eco-regions. Our approach and results provide a foundation for such studies.

Appendices

APPENDIX I: SUPPLEMENTAL PLOTS FOR CHAPTER 2

The four figures included as supporting information are the BSE-zone area-concentration plots for the other three quartiles (.5, .75, and .95) of solute concentrations that weren't included in the main text. As a reminder, the river was given a constant concentration of C = 1 mol/m^3, while the groundwater had an initial concentration of C = 0 mol/m^3. Thus, the concentration of C in a given area of the subsurface defines the percentage of the river water present. During our transient surface water-groundwater exchange models we integrated the area of the subsurface that was greater than four specified concentrations of C (0.25, 0.5, 0.75, and 0.95) to measure the area of the subsurface that were greater than these four quartiles of river concentration – ranging from greater than 25% river water, presented in the main text and used as the metric for the size of the BSE-zone, up to greater than 95% river water meaning the area in the subsurface that is almost entirely river water. Time series of how the areas of these different compositional ratios of river water and groundwater change under different dam release types and groundwater conditions is useful for interpreting the amount of surface water-groundwater interaction that occurs under different scenarios and also longitudinally at different distances downstream. Beyond the size of the compositional ratios, the high-resolution temporal resolution (1,000 seconds) that we present gives a detailed how the areas change over time, which can be informative for interpreting differences in residence times between different scenarios. For example, under a neutral groundwater head gradient the solute areas for C > 0.5 (Figure S1) grow rapidly during the rising limb of the dam release and then decreases very slowly, meaning that for

extended periods of time there are areas in the subsurface where the pore fluid is at least 50% river water. In contrast, for strongly gaining groundwater head gradients (dh/dl = 0.015) the size of the C > 0.5 area shrinks very rapidly once the dam release begins to recede, indicating that infiltrated river water spends much less time in the subsurface when there is a gaining ambient head gradient. These types of comparisons can be made between different dam release types (peak vs. square), sizes (0.5, 1.0, and 1.5 m), longitudinal distance (0 to 100 km from dam), ambient groundwater conditions, and percentage of river water that area is being measured for. The following four SI figures are provided for completeness and as a reference for the interested reader to explore if they have additional interest in comparing dam release properties and groundwater conditions on the size of surface water-groundwater mixing zones for different percentages of surface water and groundwater in the hyporheic zone.

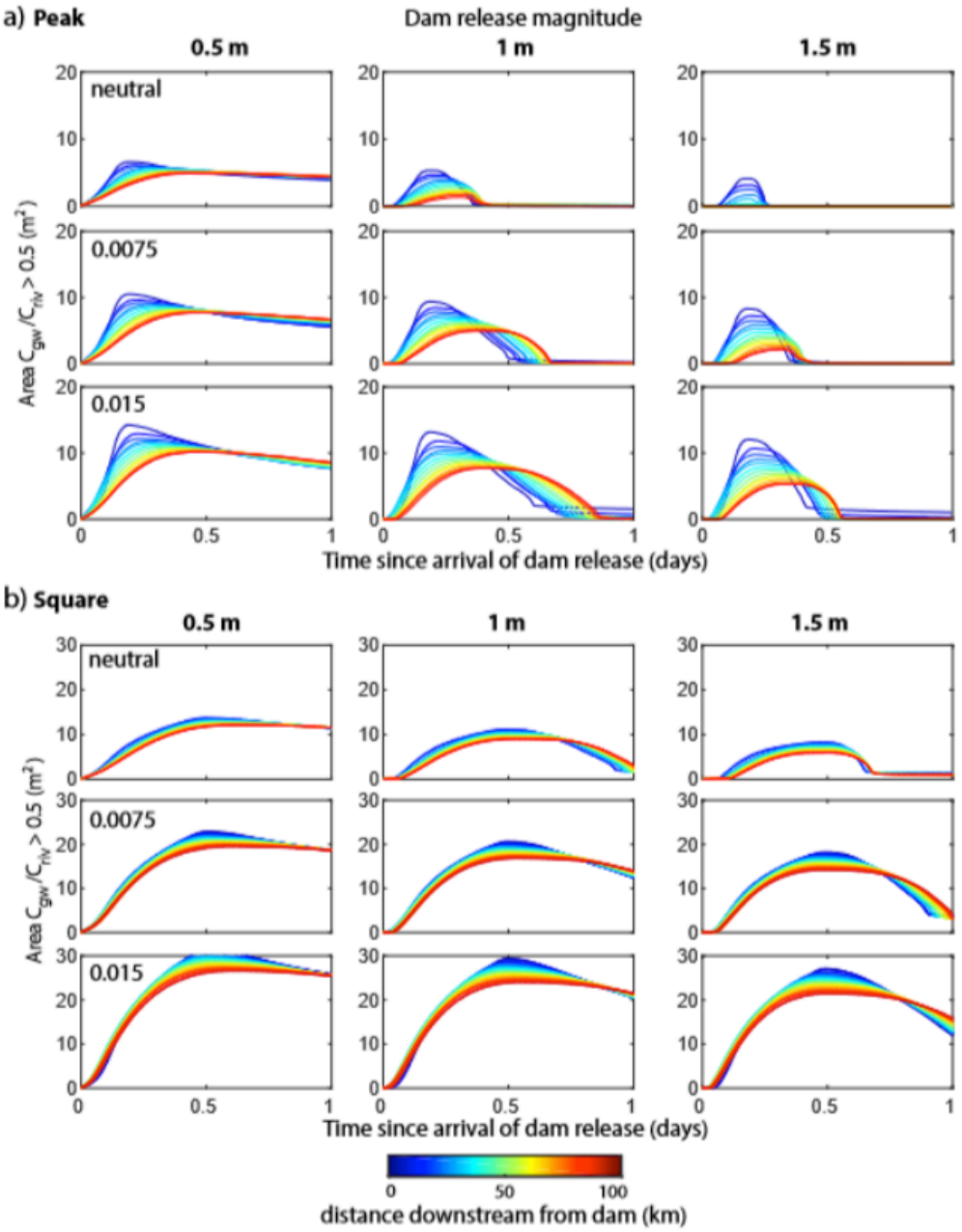

Appendix Figure 1.1: Solute area plots for C > 0.5 under neutral and gaining conditions

Time series plots for the size of subsurface area where $C > 0.5$ (at least 50% river water). Three ambient groundwater head gradients are presented: neutral = 0, moderately gaining = 0.0075, and strongly gaining = 0.015. Colorbar indicates distance downstream from dam going from cool (blue) to warm (red) with increasing distance.

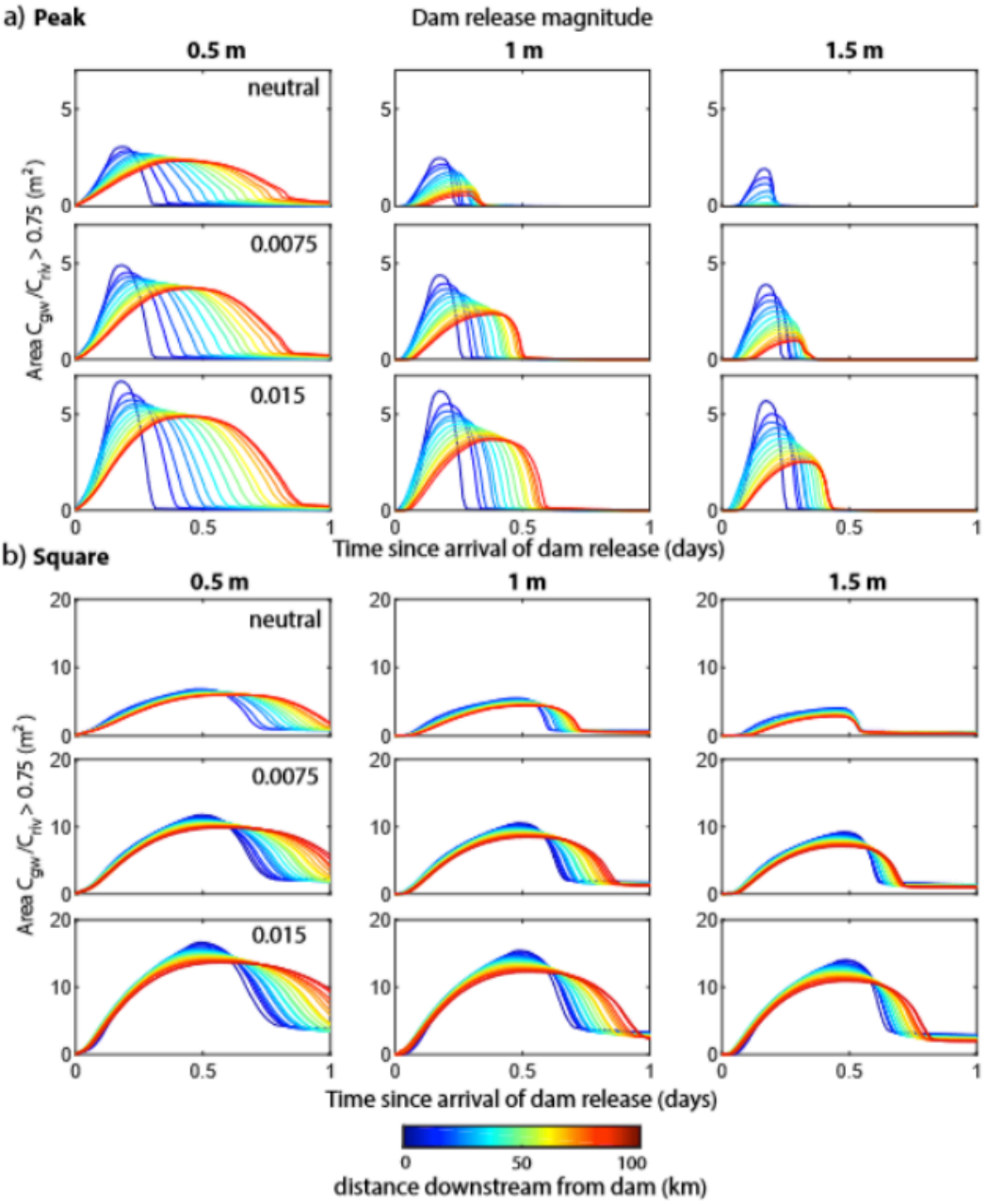

Appendix Figure 1.2: Solute area plots for C > 0.75 under neutral and gaining conditions

Time series plots for the size of subsurface area where C > 0.75 (at least 75% river water). Three ambient groundwater head gradients are presented: neutral = 0, moderately gaining = 0.0075, and strongly gaining = 0.015. Colorbar indicates distance downstream from dam going from cool (blue) to warm (red) with increasing distance.

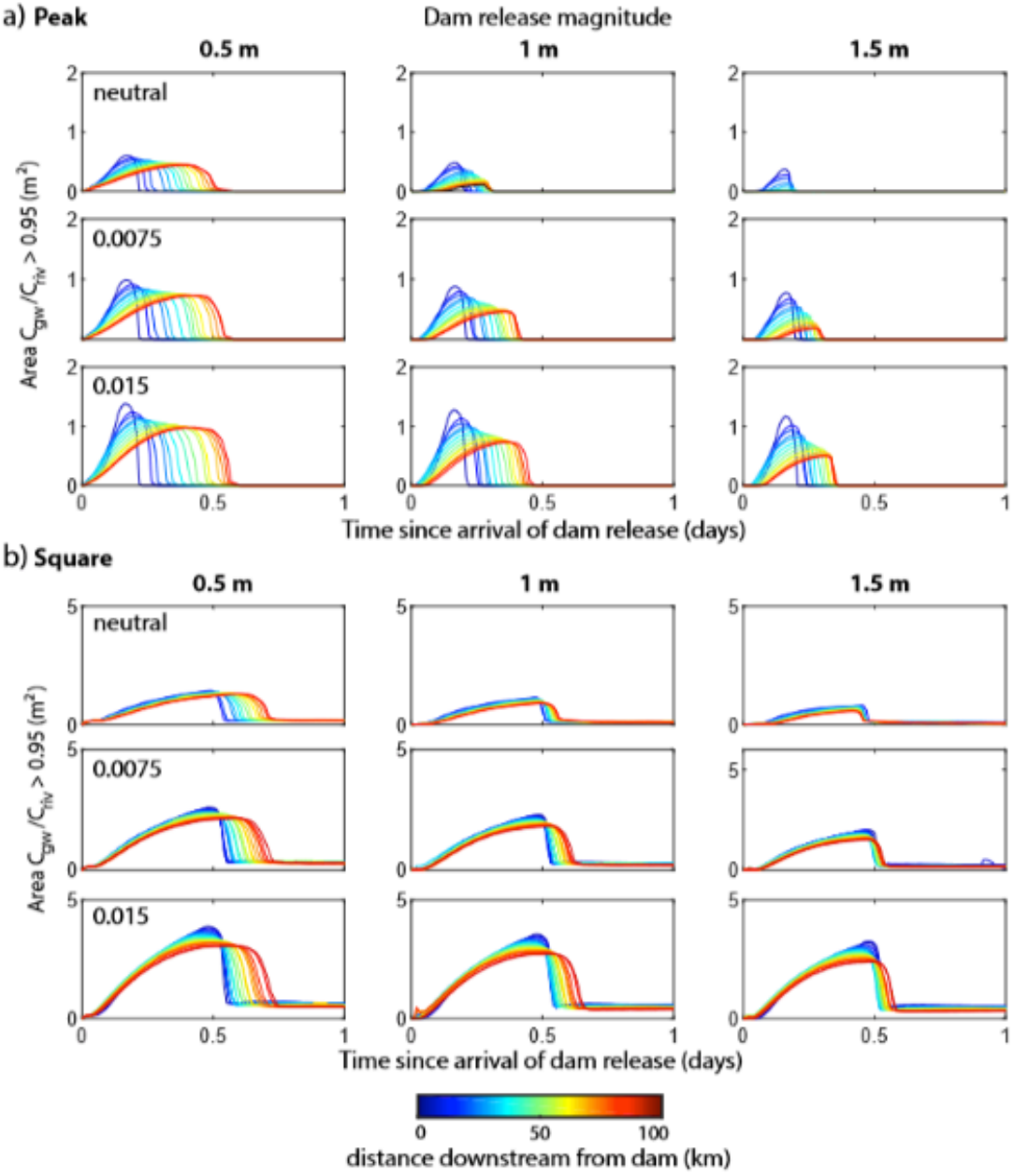

Appendix Figure 1.3: Solute area plots for C > 0.95 under neutral and gaining conditions

Time series plots for the size of subsurface area where C > 0.95 (at least 95% river water). Three ambient groundwater head gradients are presented: neutral = 0, moderately gaining = 0.0075, and strongly gaining = 0.015. Colorbar indicates distance downstream from dam going from cool (blue) to warm (red) with increasing distance.

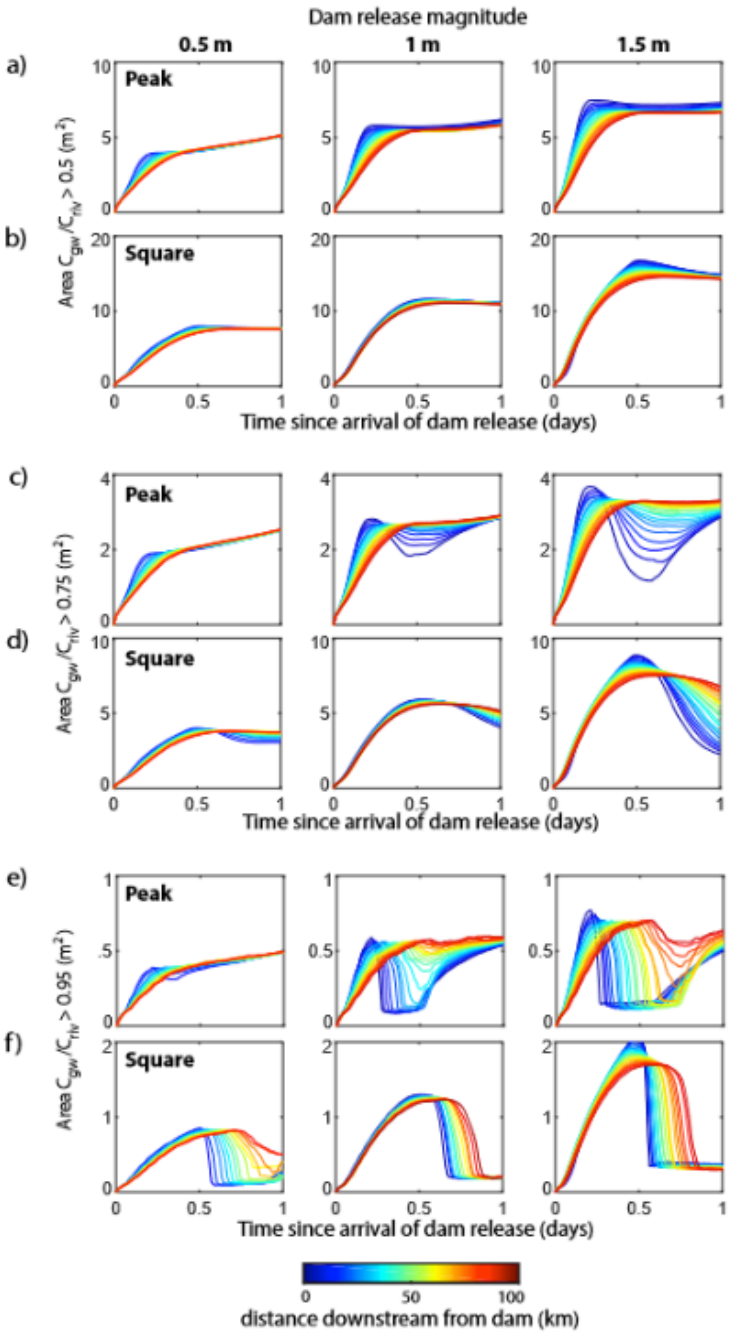

Appendix Figure 1.4: Additional solute area plots for losing conditions

Time series plots for the size of subsurface area under a losing groundwater head gradient of -0.0075 for solute areas of > 0.5 (a-b), > 0.75 (c-d), and > 0.95 (e-f). Colorbar indicates distance downstream from dam going from cool (blue) to warm (red) with increasing distance.

APPENDIX II: SUPPLEMENTAL PLOTS FOR CHAPTER 5:

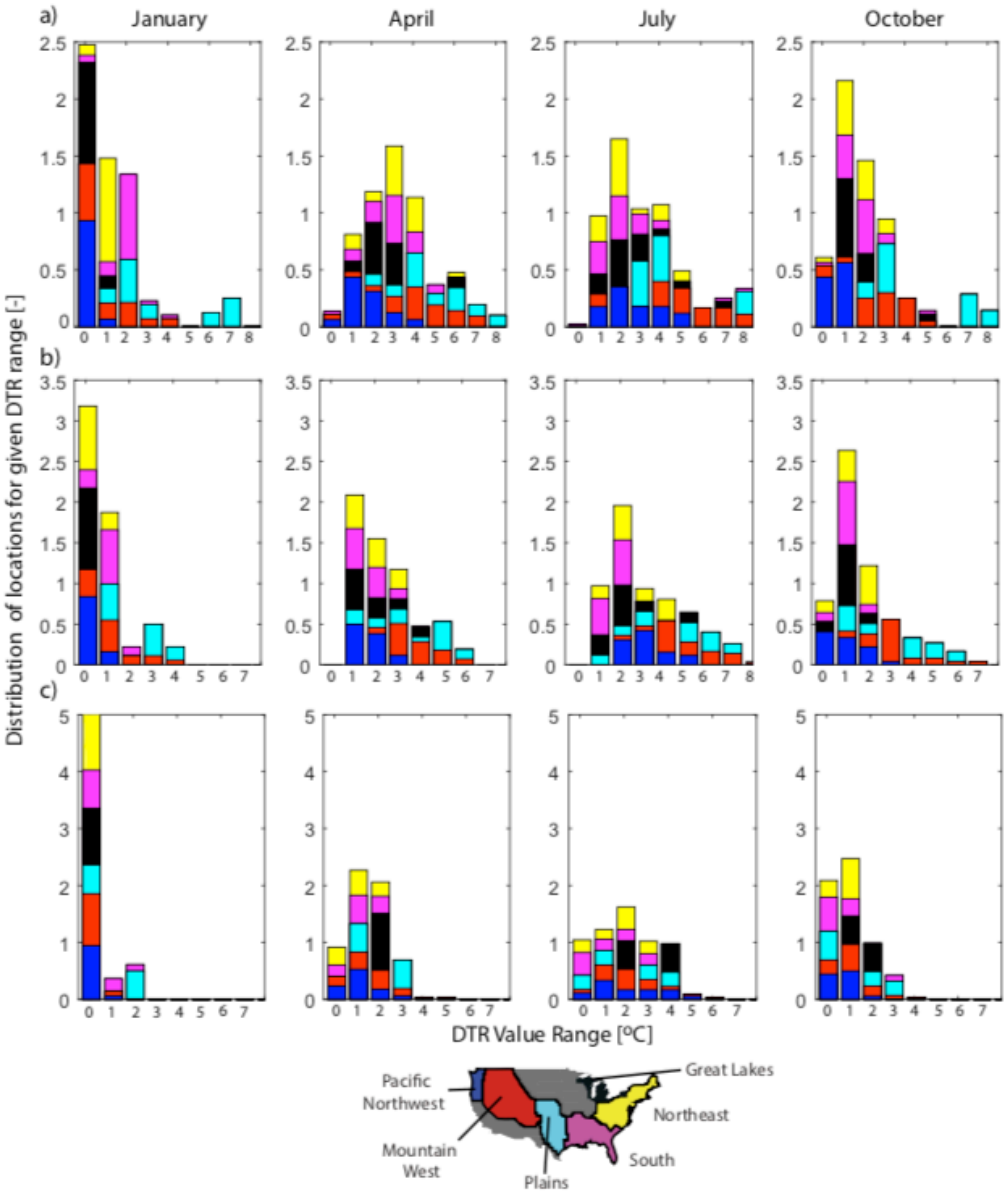

Appendix Figure 2.1: Histograms of seasonal temperature data

Seasonal temperature data presented in Figure 1 is summarized by histograms showing the DTR distributions for small (a), medium (b), and large (c) streams. Because there were large differences in the number of stations within each of the six-ecoregions, the DTR distributions within each region were normalized. The normalization makes the distribution of DTR values total to 1 for each region.

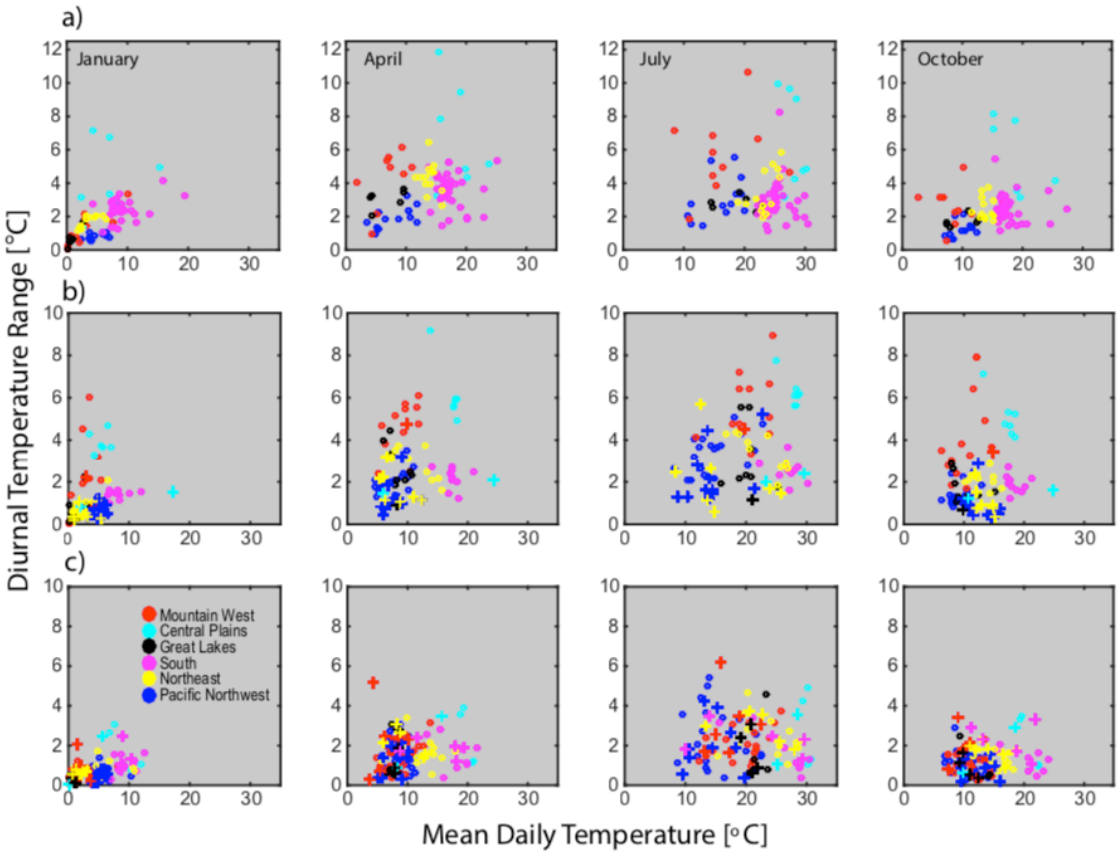

Appendix Figure 2.2: Scatter plots of monthly MDT-DTR data for each mid-season month

Scatter plots showing the monthly DTR-MDT data for the four mid-season months. The scatter plots show the data that was used for Figures 2 and 3 and is presented separately for small (a), medium (b), and large (c) streams. Circles represent sites that were used for Figures 2 and 3, while crosses represent sites that were excluded due to their proximity to potential upstream sources (dams, power plants, water treatment plants).

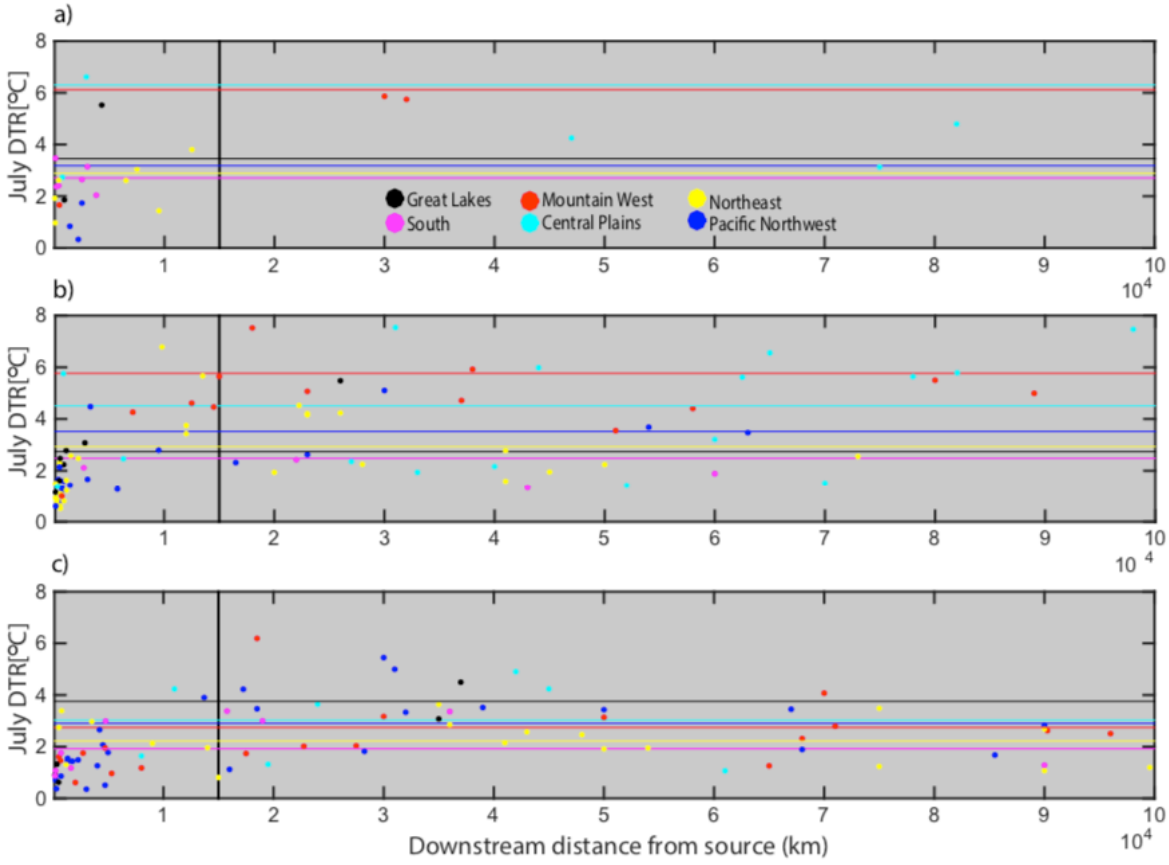

Appendix Figure 2.3:

July DTR for stations downstream of potential sources is plotted versus downstream distance for small (a), medium (b), and large (c) streams. Horizontal lines show mean July DTR for each region using sites that were not downstream of potential sources. The vertical black line shows the cutoff distance of 15 km that was used to exclude sites whose DTR was possibly affected by proximity to sources.

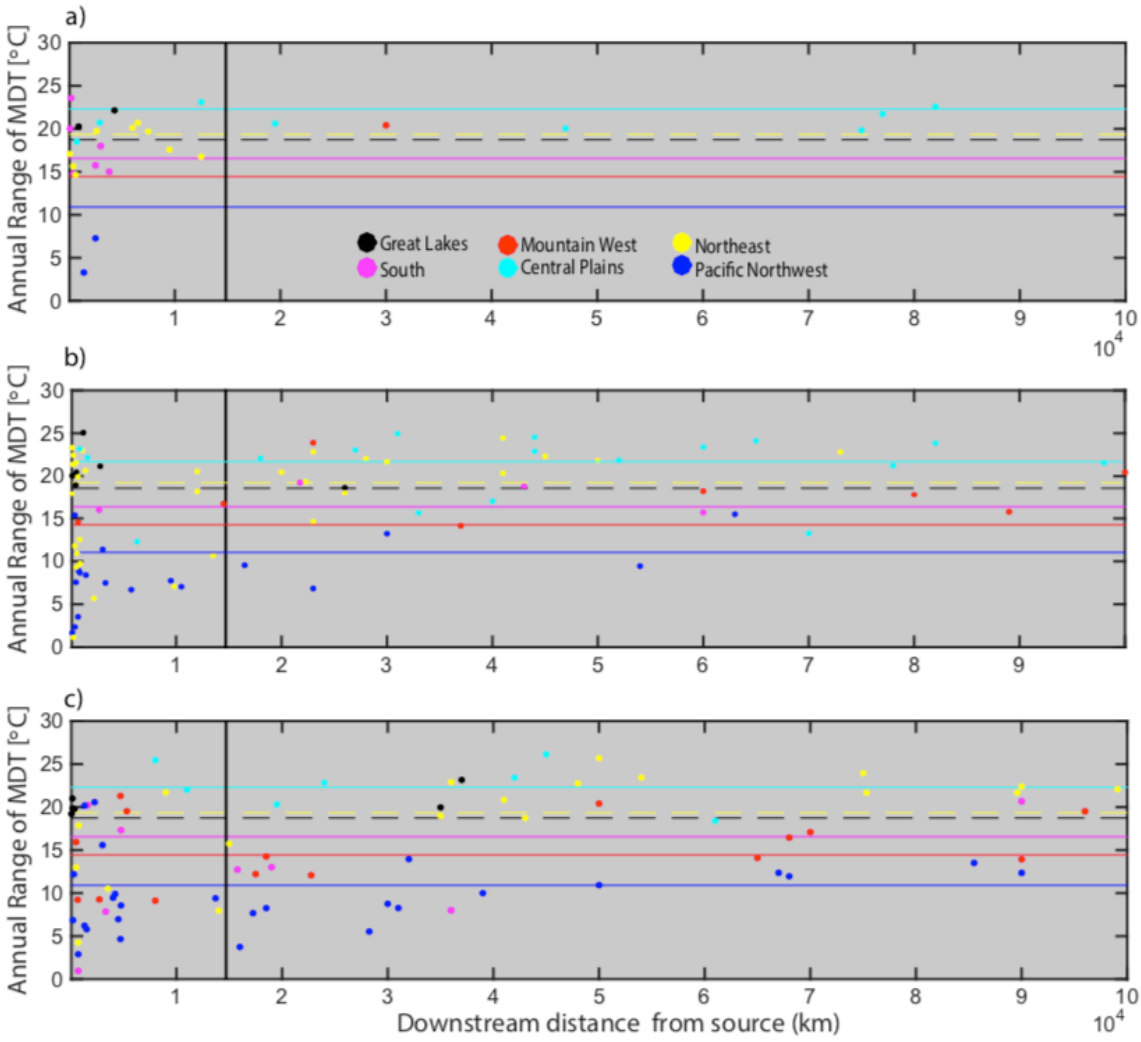

Appendix Figure 2.4:

Annual range in mean temperature for stations downstream of potential sources is plotted versus downstream distance for small (a), medium (b), and large (c) streams. The horizontal lines show the mean annual MDT range for each region using sites that were not downstream from potential sources. The vertical black line shows the cutoff distance of 15km that was used to exclude sites.

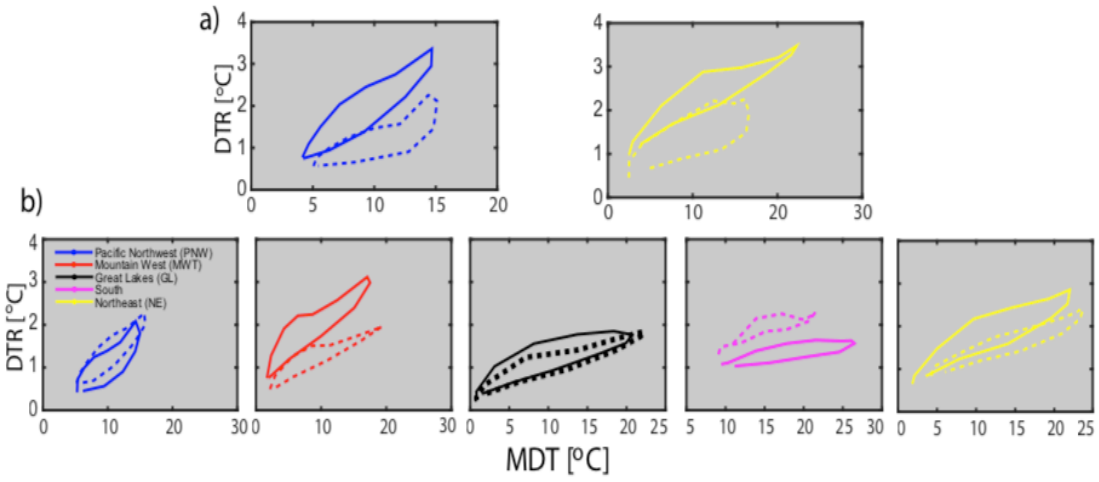

Appendix Figure 2.5:

DTR-MDT loops for medium (a) and large (b) streams showing the temperature loops for sites that are beyond the 15km cutoff and/or are not downstream from sources (solid line) and streams that are within the15 km cutoff (dotted). The DTR-MDT loops show that DTR amplitude throughout the year can be reduced for sites that are downstream of water inputs – PNW and NE in (a) and MTW and NE sites in (b). Also, the range of MDT can be reduced as seen in the NE in (a) and the South in (b). Interestingly, some of the regions do not show much of a difference in DTR or MDT behavior – PNW and GL (b).

While the ecoregions appeared to effectively distinguish differences in DTR behavior – visually from the seasonal spatial distributions of DTRs (Figure 1), as well as the apparent differences in DTR-MDT cycles (Figure 2) and monthly magnitudes of DTR (Figure 3), we wanted to quantitatively test whether eco-regions group streams by similar DTR behavior. To do this we calculated the average annual standard deviation (ASD) of stream DTRs compared to the mean within and between regions. This method is modified from *Berghuijs et al*. [2012], who used a similar approach to test whether regional groupings of sites based on certain hydrologic characteristics (aridity, timing of seasonal precipitation, steam flow, amount of precipitation as snowmelt, runoff ratio) effectively grouped sites with similar tendencies. The metric of comparison calculated by *Berghuijs et al*. [2012] is the RMSE-observation standard deviation ratio (RSR) developed by *Moriasi et al*. [2007]. For our analysis, we modified the equation used by *Berghuijs et al*. [2012] to calculate the average ASD for sites in one region compared to the mean of a different region or the region itself, given by:

$$\text{Annual ASD} = \frac{1}{N} \cdot \sum_{N=1}^{N} \sqrt{\sum_{i=1}^{12} (T^{i}_{A,N} - u^{i}_{B})^2}$$

The average ASD is the average standard deviation between the monthly DTR values of sites in Region A relative to the monthly mean DTR values for Region B. If eco-regions group similar DTR tendencies the average ASD should be the lowest when sites in a region are compared to the mean monthly values in the region itself. The results of this analysis for both DTR and MDT are summarized in Table S2. In all cases, the diagonal values (intraregional) are always lower than the off-diagonal values (interregional). Generally, the magnitudes of the annual ASD values confirm similarities

and differences between regions that are apparent from looking at the seasonal DTR maps (Figure 1), the DTR-MDT temperature cycles (Figure 2), and the monthly DTR plots (Figure 3 & Figure S6). For example, the annual ASD values for small and medium streams are largest when any of the other regions are compared to the Central Plains region. The tendency for sites in the Central Plains to have high DTR values throughout the year and generally higher DTR values then the other regions (except the Mountain West) results in large differences in the annual ASD. Another example is the similarity of the Eastern US regions to one another, seen by the low interregional values between the South, Northeast, and Great Lakes that are often close to the interregional values. The average ASD for MDTs is provided in the second column in Table S2 to demonstrate that while DTR behavior for ecoregions can sometimes be similar (as in the previous example), the differences in MDT in these regions results in different DTR-MDT thermal regimes. Referring again to the regions in the Eastern US, looking at the average ASD for the MDTs one can see that these regions have larger differences in their MDT regimes.

a) DTR

Small

Region B (region that A is compared to)	Region A: PNW	MTW	CP	GL	S	NE
PNW	2.07	7.51	13.54	2.52	4.86	5.08
MTW	6.57	4.59	9.77	5.72	5.85	4.59
CP	13.41	9.12	7.66	12.35	9.95	9.31
GL	2.96	6.86	12.61	1.55	4.53	4.31
S	4.87	6.75	10.40	3.91	2.39	2.90
NE	5.02	5.85	9.91	3.73	2.98	2.74

Medium

Region B (region that A is compared to)	Region A: PNW	MTW	CP	GL	S	NE
PNW	1.75	9.74	12.52	3.16	2.16	2.60
MTW	9.19	6.61	4.99	8.63	9.13	7.60
CP	12.47	8.33	2.79	11.92	11.98	10.78
GL	2.23	9.16	11.81	3.04	2.07	2.24
S	2.52	9.91	12.06	3.18	1.20	2.54
NE	2.60	8.47	10.82	3.39	2.17	1.96

Large

Region B (region that A is compared to)	Region A: PNW	MTW	CP	GL	S	NE
PNW	2.42	1.97	4.77	3.58	2.66	1.96
MTW	2.44	1.86	4.75	3.48	2.59	2.04
CP	4.32	4.02	4.38	5.73	3.82	3.24
GL	2.56	2.08	5.22	3.08	2.87	2.56
S	2.66	2.21	4.41	3.70	2.25	2.06
NE	2.68	2.18	4.58	4.03	2.68	1.78

b) MDT

Region B (region that A is compared to)	Region A: PNW	MTW	CP	GL	S	NE
PNW	7.97	12.63	32.47	13.06	27.81	18.21
MTW	8.89	11.59	33.64	11.14	29.72	18.87
CP	31.73	33.84	9.30	31.40	9.43	15.72
GL	13.11	14.25	31.53	8.06	29.09	16.54
S	27.66	30.47	12.11	29.31	6.24	14.13
NE	18.27	21.68	16.22	16.65	14.05	4.82

Region B (region that A is compared to)	Region A: PNW	MTW	CP	GL	S	NE
PNW	7.60	13.83	32.71	13.52	33.81	18.33
MTW	13.06	8.70	24.15	7.33	26.84	10.95
CP	32.86	24.64	3.94	25.27	7.32	17.59
GL	14.32	9.49	25.05	5.80	28.04	10.73
S	33.85	27.05	6.98	27.98	5.04	20.32
NE	18.01	10.68	17.26	10.13	20.20	9.12

Region B (region that A is compared to)	Region A: PNW	MTW	CP	GL	S	NE
PNW	8.21	11.80	37.45	15.75	31.46	20.81
MTW	11.48	8.48	35.59	9.16	31.11	17.61
CP	37.67	35.95	4.65	33.43	10.87	22.73
GL	17.00	11.64	33.33	3.97	30.27	15.35
S	31.51	30.82	8.91	29.10	9.76	18.94
NE	19.04	16.33	21.45	13.07	19.18	11.08

Appendix Table 2.1: Average annual standard deviation results within and between eco-regions

Summary of comparisons of annual ASD within and between regions for the three stream size categories shown for DTR (a) and MDT (b). The diagonals are highlighted to show intraregional comparisons. These values are all lower than the off-diagonal interregional comparisons. The comparison matrix should be read down each column, not across rows. The column header is the region whose annual ASD is calculated relative to the means of the regions in the rows.

References

Aubeneau, A. F., B. Hanrahan, D. Bolster, and J. Tank (2016), Biofilm growth in gravel bed streams controls solute residence time distributions, *Journal of Geophysical Research-Biogeosciences*, *121*(7), 1840-1850.

Arismendi, I., S. L. Johnson, J. B. Dunham, R. Haggerty, and D. Hockman-Wert (2012), The paradox of cooling streams in a warming world: Regional climate trends do not parallel variable local trends in stream temperature in the Pacific continental United States, Geophys. Res. Lett., 39, L10401.

Arntzen, E. V., D. R. Geist, and P. E. Dresel (2006), Effects of fluctuating river flow on groundwater/surface water mixing in the hyporheic zone of a regulated, large cobble bed river, *River Research and Applications*, *22*(8), 937-946.

Allan, J.D., and Castillo, M.M., 2007, Stream Ecology: Structure and function of running waters: Springer Netherlands, //www.springer.com/us/book/9781402055829.

Bevelhimer, M. S., R. A. McManamay, and B. O'Connor (2015), Characterizing Sub-Daily Flow Regimes: Implications of Hydrologic Resolution on Ecohydrology Studies, *River Research and Applications*, *31*(7), 867-879.

Baker, M. A., H. M. Valett, and C. N. Dahm (2000), Organic carbon supply and metabolism in a shallow groundwater ecosystem, *Ecology*, *81*(11), 3133-3148.

Bao J, Zhou T, Huang M, et al. Modulating Factors of Hydrologic Exchanges in a Large-Scale River Reach: Insights from Three-Dimensional Computational Fluid Dynamics Simulations. Hydrological Processes. 2018.

Barnes, R. T., A. H. Sawyer, D. M. Tight, C. D. Wallace, and M. G. Hastings (2019), Hydrogeologic Controls of Surface Water-Groundwater Nitrogen Dynamics Within a Tidal Freshwater Zone, *Journal of Geophysical Research-Biogeosciences*, *124*(11), 3343-3355.

Battin, T. J., K. Besemer, M. M. Bengtsson, A. M. Romani, and A. I. Packmann (2016), The ecology and biogeochemistry of stream biofilms, *Nature Reviews Microbiology*, *14*(4), 251-263.

Berghuijs, W. R., M. Sivapalan, R. A. Woods, and H. H. G. Savenije (2014), Patterns of similarity of seasonal water balances: A window into streamflow variability over a range of time scales, *Water Resources Research*, *50*(7), 5638-5661.

Bernhardt, E. S., et al. (2018), The metabolic regimes of flowing waters, *Limnology and Oceanography*, *63*, S99-S118.

Bevelhimer, M. S., R. A. McManamay, and B. O'Connor (2015), Characterizing Sub-Daily Flow Regimes: Implications of Hydrologic Resolution on Ecohydrology Studies, *River Research and Applications*, *31*(7), 867-879. https://doi.org/10.1002/rra.2781

Bhaskar, A. S., J. W. Harvey, and E. J. Henry (2012), Resolving hyporheic and groundwater components of streambed water flux using heat as a tracer, *Water Resources Research*, *48*.

Boano, F., A. Demaria, R. Revelli, and L. Ridolfi (2010), Biogeochemical zonation due to intrameander hyporheic flow, *Water Resources Research*, *46*.

Boano, F., J. W. Harvey, A. Marion, A. I. Packman, R. Revelli, L. Ridolfi, and A. Worman (2014), Hyporheic flow and transport processes: Mechanisms, models, and biogeochemical implications, *Reviews of Geophysics*, *52*(4), 603-679.

Boulton, A. J., S. Findlay, P. Marmonier, E. H. Stanley, and H. M. Valett (1998), The functional significance of the hyporheic zone in streams and rivers, *Annual Review of Ecology and Systematics*, *29*, 59-81.

Boulton, A. J., T. Datry, T. Kasahara, M. Mutz, and J. A. Stanford (2010), Ecology and management of the hyporheic zone: stream-groundwater interactions of running waters and their floodplains, *Journal of the North American Benthological Society*, *29*(1), 26-40.

Bourg, A. C. M., and C. Bertin (1993), Biogeochemical processes during the infiltration of river water into an alluvial aquifer, *Environmental Science & Technology*, *27*(4), 661-666.

Boutt, D. F., and B. J. Fleming (2009), Implications of anthropogenic river stage fluctuations on mass transport in a valley fill aquifer, *Water Resources Research*, *45*.

Bouwman, A. F., M. F. P. Bierkens, J. Griffioen, M. M. Hefting, J. J. Middelburg, H. Middelkoop, and C. P. Slomp (2013), Nutrient dynamics, transfer and retention along the aquatic continuum from land to ocean: towards integration of ecological and biogeochemical models, *Biogeosciences*, *10*(1), 1-22.

Briggs, M. A., E. B. Voytek, F. D. Day-Lewis, D. O. Rosenberry, and J. W. Lane (2013), Understanding Water Column and Streambed Thermal Refugia for Endangered Mussels in the Delaware River, *Environmental Science & Technology*, *47*(20), 11423-11431.

Briody, A. C., M. B. Cardenas, P. Shuai, P. S. K. Knappett, and P. C. Bennett (2016), Groundwater flow, nutrient, and stable isotope dynamics in the parafluvial-hyporheic zone of the regulated Lower Colorado River (Texas, USA) over the course of a small flood, *Hydrogeology Journal*, *24*(4), 923-935.

Brugger, A., B. Wett, I. Kolar, B. Reitner, and G. J. Herndl (2001), Immobilization and bacterial utilization of dissolved organic carbon entering the riparian zone of the alpine Enns River, Austria, *Aquatic Microbial Ecology*, *24*(2), 129-142.

Brunke, M., and T. Gonser (1997), The ecological significance of exchange processes between rivers and groundwater, *Freshwater Biology*, *37*(1), 1-33.

Bukovsky, M. (2012), Masks for the Bukovsky regionalization of North America, Regional Integrated Sciences Collective, Tech. Rep., Natl. Cent. for Atmos. Res., Boulder, Colo.

Burkholder, B. K., G. E. Grant, R. Haggerty, T. Khangaonkar, and P. J. Wampler (2008), Influence of hyporheic flow and geomorphology on temperature of a large, gravel-bed river, Clackamas River, Oregon, USA, *Hydrological Processes*, *22*(7), 941-953.

Burt, T. P., et al. (2002), Water table fluctuations in the riparian zone: comparative results from a pan-European experiment, *Journal of Hydrology*, *265*(1-4), 129-148.

Caissie, D. (2006), The thermal regime of rivers: a review, *Freshwater Biology*, *51*(8), 1389-1406.

Caissie, D., N. El-Jabi, and M. G. Satish (2001), Modelling of maximum daily water temperatures in a small stream using air temperatures, *Journal of Hydrology*, *251*(1-2), 14-28.

Caldwell, P., C. Segura, S. G. Laird, G. Sun, S. G. McNulty, M. Sandercock, J. Boggs, and J. M. Vose (2015), Short-term stream water temperature observations permit rapid assessment of potential climate change impacts, *Hydrological Processes*, *29*(9), 2196-2211.

Cardenas, M. B., and J. L. Wilson (2007a), Thermal regime of dune-covered sediments under gaining and losing water bodies, *Journal of Geophysical Research-Biogeosciences*, *112*(G4). https://doi.org/10.1029/2007JG000485

Cardenas, M. B., and J. L. Wilson (2007b), Exchange across a sediment-water interface with ambient groundwater discharge, *Journal of Hydrology*, *346*(3-4), 69-80.

Cardenas, M. B., P. C. Bennett, P. B. Zamora, K. M. Befus, R. S. Rodolfo, H. B. Cabria, and M. R. Lapus (2015), Devastation of aquifers from tsunami-like storm surge by Supertyphoon Haiyan, *Geophysical Research Letters*, *42*(8), 2844-2851

Cardenas, M. B., and M. S. Markowski (2011), Geoelectrical Imaging of Hyporheic Exchange and Mixing of River Water and Groundwater in a Large Regulated River, *Environmental Science & Technology*, *45*(4), 1407-1411. DOI: 10.1021/es103438a

Cardenas, M. B., J. L. Wilson, and V. A. Zlotnik (2004), Impact of heterogeneity, bed forms, and stream curvature on subchannel hyporheic exchange, *Water Resources Research*, *40*(8).

Carron, J. C., and H. Rajaram (2001), Impact of variable reservoir releases on management of downstream water temperatures, *Water Resources Research*, *37*(6), 1733-1743.

Carveth, C. J., A. M. Widmer, S. A. Bonar, and J. R. Simms (2007), An examination of the effects of chronic static and fluctuating temperature on the growth and survival of spikedace, Meda fulgida, with implications for management, *Journal of Thermal Biology*, *32*(2), 102-108.

Casas-Mulet, R., K. Alfredsen, B. Hamududu, and N. P. Timalsina (2015), The effects of hydropeaking on hyporheic interactions based on field experiments, *Hydrological Processes*, *29*(6), 1370-1384.

Chen, X., and X. H. Chen (2003), Stream water infiltration, bank storage, and storage zone changes due to stream-stage fluctuations, *Journal of Hydrology*, *280*(1-4), 246-264.

Clarke, A. (2006), Temperature and the metabolic theory of ecology, *Functional Ecology*, *20*(2), 405-412.

Comer-Warner, S. A., P. Romeijn, D. C. Gooddy, S. Ullah, N. Kettridge, B. Marchant, D. M. Hannah, and S. Krause (2018), Thermal sensitivity of CO2 and CH4 emissions varies with streambed sediment properties, *Nature Communications*, *9*.

Cooper, H. H. and Rorabaugh, M. I. (1963), Ground-water movements and bank storage due to flood stages in surface streams, USGS Water Supply Paper 1536-J, US Government Printing Office, 1963.

Constantz, J. (2003), Dams and downstream ground water, *Hydrological Processes*, *17*(17), 3533-3535.

Constantz, J., and H. Essaid (2007), Influence of groundwater pumping on streamflow restoration following upstream dam removals, *Hydrological Processes*, *21*(21), 2823-2834.

Covich, A. P., M. A. Palmer, and T. A. Crowl (1999), The role of benthic invertebrate species in freshwater ecosystems - Zoobenthic species influence energy flows and nutrient cycling, *Bioscience*, *49*(2), 119-127.

Covino, T. (2017), Hydrologic connectivity as a framework for understanding biogeochemical flux through watersheds and along fluvial networks, *Geomorphology*, *277*, 133-144.

Dahm, C. N., N. B. Grimm, P. Marmonier, H. M. Valett, and P. Vervier (1998), Nutrient dynamics at the interface between surface waters and groundwaters, *Freshwater Biology*, *40*(3), 427-451.

Dent, C. L., N. B. Grimm, and S. G. Fisher (2001), Multiscale effects of surface-subsurface exchange on stream water nutrient concentrations, *Journal of the North American Benthological Society*, *20*(2), 162-181.

Devito, K. J., D. Fitzgerald, A. R. Hill, and R. Aravena (2000), Nitrate dynamics in relation to lithology and hydrologic flow path in a river riparian zone, *Journal of Environmental Quality*, *29*(4), 1075-1084.

DeWeber, J. T., and T. Wagner (2014), A regional neural network ensemble for predicting mean daily river water temperature, *Journal of Hydrology*, *517*, 187-200.

Doble, R. C., R. S. Crosbie, B. D. Smerdon, L. Peeters, and F. J. Cook (2012), Groundwater recharge from overbank floods, *Water Resources Research*, *48*.

Doble, R., P. Brunner, J. McCallum, and P. G. Cook (2012), An Analysis of River Bank Slope and Unsaturated Flow Effects on Bank Storage, *Ground Water*, *50*(1), 77-86.

Ducharne, A. (2008), Importance of stream temperature to climate change impact on water quality, *Hydrology and Earth System Sciences*, *12*(3), 797-810.

Duval, T. P., and A. R. Hill (2006), Influence of stream bank seepage during low-flow conditions on riparian zone hydrology, *Water Resources Research*, *42*(10).

Ebersole, J. L., W. J. Liss, and C. A. Frissell (2003), Thermal heterogeneity, stream channel morphology, and salmonid abundance in northeastern Oregon streams, *Canadian Journal of Fisheries and Aquatic Sciences*, *60*(10), 1266-1280.

Edington, J. M. 1965, 'Some observations on stream temperature', Oikos, 15(II), 265-273.

Elliott, J. M., and M. A. Hurley (1997), A functional model for maximum growth of Atlantic Salmon parr, Salmo salar, from two populations in northwest England, *Functional Ecology*, *11*(5), 592-603.

Ferencz, S.B.**,** M.B. Cardenas., B.T. Neilson (2019) Analysis of the effects of dam release properties and ambient groundwater flow on surface water-groundwater exchange over a 100-km long reach, Water Resources Research.

Fiebig, D. & J. Marxsen, 1992. Immobilization and mineralization of dissolved free amino acids by stream-bed biofilms. Freshwat. Biol. 28: 129–140.

Findlay, S. (1995), Importance of surface-subsurface exchange in stream ecosystems- the hyporheic zone, *Limnology and Oceanography*, *40*(1), 159-164.

Fread, D.L., Lewis, J.M. (1993). Selection of Dx and Dt Computational Steps for Four-Point Implicit Nonlinear Dynamic Routing Models", ASCE National Hydraulic Engineering Conference Proceedings, San Francisco, CA.

Gammons, C. H., D. A. Nimick, and S. R. Parker (2015), Diel cycling of trace elements in streams draining mineralized areas-A review, *Applied Geochemistry*, *57*, 35-44.

Gardner, L. R., and A. M. Wilson (2006), Comparison of four numerical models for simulating seepage from salt marsh sediments, *Estuarine Coastal and Shelf Science*, *69*(3-4), 427-437.

Gerecht, K. E., M. B. Cardenas, A. J. Guswa, A. H. Sawyer, J. D. Nowinski, and T. E. Swanson (2011), Dynamics of hyporheic flow and heat transport across a bed-to-bank continuum in a large regulated river, *Water Resources Research*, *47*.

Giller, P.D. and B. Malmqvist, 1998. The Biology of Streams and Rivers. Oxford University Press, Oxford, United Kingdom.

Graham, E. B., A. R. Crump, C. T. Resch, S. Fansler, E. Arntzen, D. W. Kennedy, J. K. Fredrickson, and J. C. Stegen (2017), Deterministic influences exceed dispersal effects on hydrologically-connected microbiomes, *Environmental Microbiology*, *19*(4), 1552-1567.

Gomez-Velez, J. D., J. L. Wilson, M. B. Cardenas, and J. W. Harvey (2017), Flow and Residence Times of Dynamic River Bank Storage and Sinuosity-Driven Hyporheic Exchange, *Water Resources Research*, *53*(10), 8572-8595.

Graham, E. B., J. C. Stegen, M. Y. Huang, X. Y. Chen, and T. D. Scheibe (2019), Subsurface biogeochemistry is a missing link between ecology and hydrology in dam-impacted river corridors, *Science of the Total Environment*, *657*, 435-445.

Gu, C. H., W. Anderson, and F. Maggi (2012), Riparian biogeochemical hot moments induced by stream fluctuations, *Water Resources Research*, *48*.

Gu, C. H., G. M. Hornberger, A. L. Mills, J. S. Herman, and S. A. Flewelling (2007), Nitrate reduction in streambed sediments: Effects of flow and biogeochemical kinetics, *Water Resources Research*, *43*(12).

Gu, C. H., G. M. Hornberger, J. S. Herman, and A. L. Mills (2008), Influence of stream-groundwater interactions in the streambed sediments on NO3- flux to a low-relief coastal stream, *Water Resources Research*, *44*(11).

Harvey, J., and M. Gooseff (2015), River corridor science: Hydrologic exchange and ecological consequences from bedforms to basins, *Water Resources Research*, *51*(9), 6893-6922.

Harvey, J., et al. (2019), How Hydrologic Connectivity Regulates Water Quality in River Corridors, *Journal of the American Water Resources Association*, *55*(2), 369-381.

Hawkins, C. P., J. N. Hogue, L. M. Decker, and J. W. Feminella (1997), Channel morphology, water temperature, and assemblage structure of stream insects, *Journal of the North American Benthological Society*, *16*(4), 728-749.

Hedin, L. O., J. C. von Fischer, N. E. Ostrom, B. P. Kennedy, M. G. Brown, and G. P. Robertson (1998), Thermodynamic constraints on nitrogen transformations and other biogeochemical processes at soil-stream interfaces, *Ecology*, *79*(2), 684-703.

Helton, A. M., G. C. Poole, R. A. Payn, C. Izurieta, and J. A. Stanford (2012), Scaling flow path processes to fluvial landscapes: An integrated field and model assessment of temperature and dissolved oxygen dynamics in a river-floodplain-aquifer system, *Journal of Geophysical Research-Biogeosciences*, *117*.

Hester, E. T., and M. W. Doyle (2011), Human Impacts to River Temperature and Their Effects on Biological Processes: A Quantitative Synthesis, *Journal of the American Water Resources Association*, *47*(3), 571-587. https://doi.org/10.1111/j.1752-1688.2011.00525.x

Hester, E. T., M. B. Cardenas, R. Haggerty, and S. V. Apte (2017), The importance and challenge of hyporheic mixing, *Water Resources Research*, *53*(5), 3565-3575.

Hill, A. R. (1996), Nitrate removal in stream riparian zones, *Journal of Environmental Quality*, *25*(4), 743-755.

Hill, A. R., P. G. F. Vidon, and J. Langat (2004), Denitrification potential in relation to lithology in five headwater riparian zones, *Journal of Environmental Quality*, *33*(3), 911-919.

Hill, R. A., C. P. Hawkins, and D. M. Carlisle (2013), Predicting thermal reference conditions for USA streams and rivers, *Freshwater Science*, *32*(1), 39-55.

Hoppe-Jones, C., G. Oldham, and J. E. Drewes (2010), Attenuation of total organic carbon and unregulated trace organic chemicals in US riverbank filtration systems, *Water Research*, *44*(15), 4643-4659.

Hunt, B. (1990), An approximation for the bank storage effect, *Water Resources Research*, *26*(11), 2769-2775.

In-Situ. Operators Manual: Aqua TROLL® 100 & 200 Sonde. PDF. In-Situ, August 2016.https://in-situ.com/wp-content/uploads/2014/11/Aqua-TROLL-100-200_Manual.pdf

Isaak, D. J., and W. A. Hubert (2001), A hypothesis about factors that affect maximum summer stream temperatures across montane landscapes, *Journal of the American Water Resources Association*, *37*(2), 351-366.

Johnson, B. M., L. Saito, M. A. Anderson, P. Weiss, M. Andre, and D. G. Fontane (2004), Effects of climate and dam operations on reservoir thermal structure, *Journal of Water Resources Planning and Management-Asce*, *130*(2), 112-122.

Jones, N. E. (2014), The dual nature of hydropeaking rivers: is ecopeaking possible?, *River Research and Applications*, *30*(4), 521-526.

Kelleher, C., T. Wagener, M. Gooseff, B. McGlynn, K. McGuire, and L. Marshall (2012), Investigating controls on the thermal sensitivity of Pennsylvania streams, *Hydrological Processes*, *26*(5), 771-785.

Kennedy, T. A., J. D. Muehlbauer, C. B. Yackulic, D. A. Lytle, S. W. Miller, K. L. Dibble, E. W. Kortenhoeven, A. N. Metcalfe, and C. V. Baxter (2016), Flow Management for Hydropower Extirpates Aquatic Insects, Undermining River Food Webs, *Bioscience*, *66*(7), 561-575.

Kondolf, G. M., L. M. Maloney, and J. G. Williams (1987), Effects of bank storage and well pumping on base flow, Carmel River, Monterey County, California, *Journal of Hydrology*, *91*(3-4), 351-369.

Koussis, A. D., E. Akylas, and K. Mazi (2007), Response of sloping unconfined aquifer to stage changes in adjacent stream - II. Applications, *Journal of Hydrology*, *338*(1-2), 73-84.

Larkin, R. G., and J. M. Sharp (1992), On the relationship between river basin geomorphology, aquifer hydraulics, and groundwater flow direction in alluvial aquifers, *Geological Society of America Bulletin*, *104*(12), 1608-1620

LCRA Website, https://www.lcra.org/water/dams-and-lakes/Pages/default.aspx (accessed

March 2018).
Liang, X. Y., H. B. Zhan, and K. Schilling (2018), Spatiotemporal Responses of Groundwater Flow and Aquifer-River Exchanges to Flood Events, *Water Resources Research*, *54*(3), 1513-1532.
Ling, F., G. M. Foody, H. Du, X. Ban, X. D. Li, Y. H. Zhang, and Y. Du (2017), Monitoring Thermal Pollution in Rivers Downstream of Dams with Landsat ETM plus Thermal Infrared Images, *Remote Sensing*, *9*(11).
Liu, D. S., J. Zhao, X. B. Chen, Y. Y. Li, S. P. Weiyan, and M. M. Feng (2018), Dynamic processes of hyporheic exchange and temperature distribution in the riparian zone in response to dam-induced water fluctuations, *Geosciences Journal*, *22*(3), 465-475.
Liu, D. S., J. Zhao, W. H. Jeon, and J. Y. Lee (2019), Solute dynamics across the stream-to-riparian continuum under different flood waves, *Hydrological Processes*, *33*(20), 2627-2641.
Lowney, C. L. (2000), Stream temperature variation in regulated rivers: Evidence for a spatial pattern in daily minimum and maximum magnitudes, Water Resour. Res., 36(10), 2947–2955.
LTC Levelogger Edge Datasheet, https://www.solinst.com/products/dataloggers-and-telemetry/3001-levelogger-series/ltc-levelogger/datasheet.php (accessed February 2018).
Maurice, P. A., M. J. Pullin, S. E. Cabaniss, Q. H. Zhou, K. Namjesnik-Dejanovic, and G. R. Aiken (2002), A comparison of surface water natural organic matter in raw filtered water samples, XAD, and reverse osmosis isolates, *Water Research*, *36*(9), 2357-2371.
McCallum, J. L., P. G. Cook, P. Brunner, and D. Berhane (2010), Solute dynamics during bank storage flows and implications for chemical base flow separation, *Water Resources Research*, *46*.
McCallum, J. L., and M. Shanafield (2016), Residence times of stream-groundwater exchanges due to transient stream stage fluctuations, *Water Resources Research*, *52*(3), 2059-2073.
McClain, M. E., et al. (2003), Biogeochemical hot spots and hot moments at the interface of terrestrial and aquatic ecosystems, *Ecosystems*, *6*(4), 301-312.
McDowell, W. H., 1985. Kinetics and mechanisms of dissolved organic carbon retention in a headwater stream. Biogeochemistry 1: 329–352.
McKnight, D. M., K. E. Bencala, G. W. Zellweger, G. R. Aiken, G. L. Feder & K. A.Thorn, 1992. Sorption of dissolved organic carbon by hydrous aluminum andiron oxides occurring at the confluence of deer creek with the Snake River, Summit County, Colorado. Envir. Sci. Technol. 26: 1388–139

McManamay, R. A., C. O. Oigbokie, S. C. Kao, and M. S. Bevelhimer (2016), Classification of US Hydropower Dams by their Modes of Operation, *River Research and Applications*, *32*(7), 1450-1468.

Moench, A. F., V. B. Sauer, and M. E. Jennings (1974), Modification of routed streamflow by channel loss and base flow, *Water Resources Research*, *10*(5), 963-968.

Mohseni, O., H. G. Stefan, and T. R. Erickson (1998), A nonlinear regression model for weekly stream temperatures, *Water Resources Research*, *34*(10), 2685-2692.

Moriasi, D., Arnold, J., Van Liew, M., Bingner, R., Harmel, R., Veith, T. 2007. Model Evaluation Guidelines for Systematic Quantification of Accuracy in Watershed Simulations: Transactions of the American Society of Agricultural and Biological Engineers. American Society of Agricultural and Biological Engineers, St. Joseph, MI. Volume 50, Number 3. Pages 885-900.

Morin, G. and Couillard, D. (1990) Predicting River Temperatures with a Hydrological Model. In: Cheremisinoff, N.P., Ed., Encyclopedia of Fluid Mechanic, Surface and Groundwater Flow Phenomena, Gulf Publishing Company, Houston, Vol. 10, 171-209.

Morrill, J. C., R. C. Bales, and M. H. Conklin (2005), Estimating stream temperature from air temperature: Implications for future water quality, *Journal of Environmental Engineering-Asce*, *131*(1), 139-146.

Moser, D. P., J. K. Fredrickson, D. R. Geist, E. V. Arntzen, A. D. Peacock, S. M. W. Li, T. Spadoni, and J. P. McKinley (2003), Biogeochemical processes and microbial characteristics across groundwater-surface water boundaries of the Hanford Reach of the Columbia River, *Environmental Science & Technology*, *37*(22), 5127-5134.

Musial, C. T., A. H. Sawyer, R. T. Barnes, S. Bray, and D. Knights (2016), Surface water-groundwater exchange dynamics in a tidal freshwater zone, *Hydrological Processes*, *30*(5), 739-750.

Naiman, R. J., and H. Decamps (1997), The ecology of interfaces: Riparian zones, *Annual Review of Ecology and Systematics*, *28*, 621-658.

Neilson, B. T., S. C. Chapra, D. K. Stevens, and C. Bandaragoda (2010), Two-zone transient storage modeling using temperature and solute data with multiobjective calibration: 1. Temperature, *Water Resources Research*, *46*.

Newcomb, R. C, and S. G. Brown (1961), Evaluation of Bank Storage Along the Columbia River Between Richland and China Bar, Washington, USGS Water Supply Paper 1539-I, US Government Printing Office, 1961.

Nimick, D. A., C. H. Gammons, and S. R. Parker (2011), Diel biogeochemical processes and their effect on the aqueous chemistry of streams: A review, *Chemical Geology*, *283*(1-2), 3-17.

Norman, F. A., and M. B. Cardenas (2014), Heat transport in hyporheic zones due to bedforms: An experimental study, *Water Resources Research*, *50*(4), 3568-3582.

NREL Solar Radiation Resource Maps, *NREL*, 1 Jan. 2017 http://rredc.nrel.gov/solar/old_data/nsrdb/1961- 1990/redbook/atlas/

Olden, J. D., and R. J. Naiman (2010), Incorporating thermal regimes into environmental flows assessments: modifying dam operations to restore freshwater ecosystem integrity, *Freshwater Biology*, *55*(1), 86-107.

Onset. TMC6-HD Sensor. PDF. Bourne, MA: Onset. https://www.onsetcomp.com/datasheet/TMC6-HD

Onset. U12-008 Data Logger. PDF. Bourne, MA: Onset. https://www.onsetcomp.com/datasheet/U12-008

Onset. U22-001 Data Logger. PDF. Bourne, MA: Onset. https://www.onsetcomp.com/datasheet/U22-001

Parkinson, E. A., E. V. Lea, M. A. Nelitz, J. M. Knudson, and R. D. Moore (2016), Identifying Temperature Thresholds Associated with Fish Community Changes in British Columbia, Canada, to Support Identification of Temperature Sensitive Streams, *River Research and Applications*, *32*(3), 330-347.

Pinder, G. F., and S. P. Sauer (1971), Numerical simulation of flood wave modification due to bank storage effects, *Water Resources Research*, *7*(1), 63-70, 1971.

Pfannkuch, H. O., and T. C. Winter (1984), Effect of Anisotropy and Groundwater System Geometry on Seepage Through Lakebeds. 1. Analog and Dimensional Analysis, *Journal of Hydrology*, *75*(1-4), 213-237.

Poff, N. L., J. D. Olden, D. M. Merritt, and D. M. Pepin (2007), Homogenization of regional river dynamics by dams and global biodiversity implications, *Proceedings of the National Academy of Sciences of the United States of America*, *104*(14), 5732-5737.

Poole, G. C., and C. H. Berman (2001), An ecological perspective on in-stream temperature: Natural heat dynamics and mechanisms of human-caused thermal degradation, *Environmental Management*, *27*(6), 787-802.

Pusch, M., D. Fiebig, I. Brettar, H. Eisenmann, B. K. Ellis, L. A. Kaplan, M. A. Lock, M. W. Naegeli, and W. Traunspurger (1998), The role of micro-organisms in the ecological connectivity of running waters, *Freshwater Biology*, *40*(3), 453-495.

Reeves, H. W., P. M. Thibodeau, R. G. Underwood, and L. R. Gardner (2000), Incorporation of total stress changes into the ground water model SUTRA, *Ground Water*, *38*(1), 89-98.

Rhodes, K. A., T. Proffitt, T. Rowley, P. S. K. Knappett, D. Montiel, N. Dimova, D. Tebo, and G. R. Miller (2017), The Importance of Bank Storage in Supplying

Baseflow to Rivers Flowing Through Compartmentalized, Alluvial Aquifers, Water Resources Research, 53(12), 10539-10557.
Ricketts, T.H., and coauthors, 1999. Terrestrial ecoregions of North America: A conservation assessment. Island Press, Washington, DC, 485p.
Risley, J. C., J. Constantz, H. Essaid, and S. Rounds (2010), Effects of upstream dams versus groundwater pumping on stream temperature under varying climate conditions, *Water Resources Research*, *46*.
Robinson, C., L. Li, and D. A. Barry (2007), Effect of tidal forcing on a subterranean estuary, *Advances in Water Resources*, *30*(4), 851-865.
Roley, S. S., J. L. Tank, and M. A. Williams (2012), Hydrologic connectivity increases denitrification in the hyporheic zone and restored floodplains of an agricultural stream, *Journal of Geophysical Research-Biogeosciences*, *117*.
Rorabaugh, M.I. (1963), Estimating changes in bank storage and ground-water contribution to streamflow: International Association of Scientific Hydrology, Publication 63, p. 432-441.
Rosenberg, D. M., P. McCully, and C. M. Pringle (2000), Global-scale environmental effects of hydrological alterations: Introduction, *Bioscience*, *50*(9), 746-751.
Sawyer, A. H., M. B. Cardenas, A. Bomar, and M. Mackey (2009), Impact of dam operations on hyporheic exchange in the riparian zone of a regulated river, *Hydrological Processes*, *23*(15), 2129-2137.
Secor, D. H., and E. D. Houde (1995), Temperature effects on the timing of striped bass egg-production, larval viability, and recruitment potential in the Patuxent River (Chesapeake Bay), *Estuaries*, *18*(3), 527-544.
Segura, C., P. Caldwell, G. Sun, S. McNulty, and Y. Zhang (2015), A model to predict stream water temperature across the conterminous USA, *Hydrological Processes*, *29*(9), 2178-2195.
Shanafield, M., P. G. Cook, P. Brunner, J. McCallum, and C. T. Simmons (2012), Aquifer response to surface water transience in disconnected streams, *Water Resources Research*, *48*.
Sharma, L., J. Greskowiak, C. Ray, P. Eckert, and H. Prommer (2012), Elucidating temperature effects on seasonal variations of biogeochemical turnover rates during riverbank filtration, *Journal of Hydrology*, *428*, 104-115.
Shuai, P., M. B. Cardenas, P. S. K. Knappett, P. C. Bennett, and B. T. Neilson (2017), Denitrification in the banks of fluctuating rivers: The effects of river stage amplitude, sediment hydraulic conductivity and dispersivity, and ambient groundwater flow, *Water Resources Research*, *53*(9), 7951-7967.
Shuai, P., X. Y. Chen, X. H. Song, G. E. Hammond, J. Zachara, P. Royer, H. Y. Ren, W. A. Perkins, M. C. Richmond, and M. Y. Huang (2019), Dam Operations and

Subsurface Hydrogeology Control Dynamics of Hydrologic Exchange Flows in a Regulated River Reach, *Water Resources Research*, *55*(4), 2593-2612.

Siergieiev, D., A. Widerlund, J. Ingri, A. Lundberg, and B. Ohlander (2014), Flow regulation effects on the hydrogeochemistry of the hyporheic zone in boreal rivers, *Science of the Total Environment*, *499*, 424-436.

Siergieiev, D., L. Ehlert, T. Reimann, A. Lundberg, and R. Liedl (2015), Modelling hyporheic processes for regulated rivers under transient hydrological and hydrogeological conditions, *Hydrology and Earth System Sciences*, *19*(1), 329-340.

Sinokrot, B. A., and H. G. Stefan (1993), Stream Temperature Dynamics - Measurements and Modeling, *Water Resources Research*, *29*(7), 2299-2312.

SOKKIA Series 10 Operator's Manual, 2001, 260-63 HASE, ATSUGI, KANAGAWA, 243-0036 JAPAN, SOKKIA CO, LTD, 144 p., https://cn.sokkia.com/sites/default/files/sc_files/downloads/set_10_series_operators_manual_-_4th_ed_0.pdf (accessed February 2018).

Song, X. H., X. Y. Chen, J. Stegen, G. Hammond, H. S. Song, H. Dai, E. Graham, and J. M. Zachara (2018), Drought Conditions Maximize the Impact of High-Frequency Flow Variations on Thermal Regimes and Biogeochemical Function in the Hyporheic Zone, *Water Resources Research*, *54*(10), 7361-7382.

Song, Hyun-Seob,James C. Stegen, Emily B. Graham, Joon-Yong Lee, Vanessa A. Garayburu-Caruso, William C. Nelson, Xingyuan Chen, J. David Moulton, Timothy D. Scheibe. Representing Organic Matter Thermodynamics in Biogeochemical Reactions via Substrate-Explicit Modeling. bioRxiv 2020.02.27.968669; doi: https://doi.org/10.1101/2020.02.27.968669

Squillace, P. J. (1996), Observed and simulated movement of bank-storage water, *Ground Water*, *34*(1), 121-134.

Steel, E. A., and I. A. Lange (2007), Using wavelet analysis to detect changes in water temperature regimes at multiple scales: Effects of multi-purpose dams in the Willamette River basin, *River Research and Applications*, *23*(4), 351-359.

Stegen, J. C., et al. (2016), Groundwater-surface water mixing shifts ecological assembly processes and stimulates organic carbon turnover, *Nature Communications*, *7*.

Stegen, J. C., et al. (2018), Influences of organic carbon speciation on hyporheic corridor biogeochemistry and microbial ecology, *Nature Communications*, *9*.

Sun, D. L., R. T. Pinker, and M. Kafatos (2006), Diurnal temperature range over the United States: A satellite view, *Geophysical Research Letters*, *33*(5).

Thullner, M., J. Zeyer, and W. Kinzelbach (2002), Influence of microbial growth on hydraulic properties of pore networks, *Transport in Porous Media*, *49*(1), 99-122.

Triska, F. J., V. C. Kennedy, R. J. Avanzino, G. W. Zellweger, and K. E. Bencala (1989),

Retention and transport of nutrients in a 3rd-order stream in northwestern California: Hyporheic processes, *Ecology*, *70*(6), 1877-1892.

US Army Corps of Engineers, HEC-RAS River Analysis System User Manual (2016), vol. 5.0, 2016, pp. 1–960.

Vannote, R. L., G. W. Minshall, K. W. Cummins, J. R. Sedell, and C. E. Cushing (1980), River Continuum Concept, *Canadian Journal of Fisheries and Aquatic Sciences*, *37*(1), 130-137.

Vervier, P., S. Bonvallet-Garay, S. Sauvage, H. M. Valett, and J. M. Sanchez-Perez (2009), Influence of the hyporheic zone on the phosphorus dynamics of a large gravel-bed river, Garonne River, France, *Hydrological Processes*, *23*(12), 1801-1812.

Vidon, P., C. Allan, D. Burns, T. P. Duval, N. Gurwick, S. Inamdar, R. Lowrance, J. Okay, D. Scott, and S. Sebestyen (2010), Hot Spots and Hot Moments in Riparian Zones: Potential for Improved Water Quality Management1, *Journal of the American Water Resources Association*, *46*(2), 278-298.

Wallace, C. D., A. H. Sawyer, and R. T. Barnes (2019), Spectral analysis of continuous redox data reveals geochemical dynamics near the stream-aquifer interface, *Hydrological Processes*, *33*(3), 405-413.

Ward, J. V. (1985), Thermal Characteristics of Running Waters, *Hydrobiologia*, *125*(JUN), 31-46.

Ward, J. V., G. Bretschko, M. Brunke, D. Danielopol, J. Gibert, T. Gonser, and A. G. Hildrew (1998), The boundaries of river systems: the metazoan perspective, *Freshwater Biology*, *40*(3), 531-569.

Watson, J. A., M. B. Cardenas, S. B. Ferencz, P. S. K. Knappett, and B. T. Neilson (2018), The effects of floods on the temperature of riparian groundwater, *Hydrological Processes*, *32*(9), 1267-1281.

Webb, B. W., and D. E. Walling (1993), Long-Term Water Temperature Behavior in an Upland Stream, *Hydrological Processes*, *7*(1), 19-32.

Webb, B. W. (1996), Trends in stream and river temperature. Hydrol. Process., 10: 205–226.

Webb, B. W., and Y. Zhang (1997), Spatial and seasonal variability in the components of the river heat budget, *Hydrological Processes*, *11*(1), 79-101.

Webb, B. W., D. M. Hannah, R. D. Moore, L. E. Brown, and F. Nobilis (2008), Recent advances in stream and river temperature research, *Hydrological Processes*, *22*(7), 902-918.

Welch, C., P. G. Cook, G. A. Harrington, and N. I. Robinson (2013), Propagation of solutes and pressure into aquifers following river stage rise, *Water Resources Research*, *49*(9), 5246-5259.

Welch, C., G. A. Harrington, M. Leblanc, J. Batlle-Aguilar, and P. G. Cook (2014), Relative rates of solute and pressure propagation into heterogeneous alluvial

aquifers following river flow events, *Journal of Hydrology*, *511*, 891-903.
Welch, C., G. A. Harrington, and P. G. Cook (2015), Influence of Groundwater Hydraulic Gradient on Bank Storage Metrics, *Groundwater*, *53*(5), 782-793.
Whiting, P. J., and M. Pomeranets (1997), A numerical study of bank storage and its contribution to streamflow, *Journal of Hydrology*, *202*(1-4), 121-136.
Wilson, A. M., and L. R. Gardner (2006), Tidally driven groundwater flow and solute exchange in a marsh: Numerical simulations, *Water Resources Research*, *42*(1).
Winter, T. C., and H. O. Pfannkuch (1984), Effect of Anisotropy and Groundwater System Geometry on Seepage Through Lakebeds. 2. Numerical Simulation Analysis, *Journal of Hydrology*, *75*(1-4), 239-253.
Wohl, E. (2019). Forgotten legacies: Understanding and mitigating historical human alterations of river corridors. *Water Resources Research*, 55, 5181– 5201.
Worman, A., A. I. Packman, L. Marklund, J. W. Harvey, and S. H. Stone (2006), Exact three-dimensional spectral solution to surface-groundwater interactions with arbitrary surface topography, *Geophysical Research Letters*, *33*(7).
Wright, S. A., C. R. Anderson, and N. Voichick (2009), A Simplified Water Temperature Model for the Colorado River Below Glen Canyon Dam, *River Research and Applications*, *25*(6), 675-686.
Wroblicky, G. J., M. E. Campana, H. M. Valett, and C. N. Dahm (1998), Seasonal variation in surface-subsurface water exchange and lateral hyporheic area of two stream-aquifer systems, *Water Resources Research*, *34*(3), 317-328.
Xian, Y., M. G. Jin, H. B. Zhan, and Y. F. Liu (2019), Reactive Transport of Nutrients and Bioclogging During Dynamic Disconnection Process of Stream and Groundwater, *Water Resources Research*, *55*(5), 3882-3903.
Xie, Y. Q., P. G. Cook, M. Shanafield, C. T. Simmons, and C. M. Zheng (2016), Uncertainty of natural tracer methods for quantifying river-aquifer interaction in a large river, *Journal of Hydrology*, *535*, 135-147.
Yakuwa, I., 1960. Phase of the diurnal variation of water temperature of a river. Mem. Eng. Hokkaido 11: 1-10.
Yarrow, M. M., and V. H. Marin (2007), Toward conceptual cohesiveness: A historical analysis of the theory and utility of ecological boundaries and transition zones, *Ecosystems*, *10*(3), 462-476.
Yellen, B., and D. F. Boutt (2015), Hydropeaking induces losses from a river reach: observations at multiple spatial scales, *Hydrological Processes*, *29*(15), 3261-3275.
Yim, C. S., and M. F. N. Mohsen (1992), Simulation of tidal effects on contaminant transport in porous-media, *Ground Water*, *30*(1), 78-86.
Young, R. G., C. D. Matthaei, and C. R. Townsend (2008), Organic matter breakdown

and ecosystem metabolism: functional indicators for assessing river ecosystem health, *Journal of the North American Benthological Society*, *27*(3), 605-625.]

Zachara, J. M., Chen, X., Song, X., Shuai, P., Murray, C., & Resch, C. T. (2020). Kilometer-scale hydrologic exchange flows in a gravel bed river corridor and their implications to solute migration. Water Resources Research, 56.

Zarnetske, J. P., R. Haggerty, S. M. Wondzell, and M. A. Baker (2011), Labile dissolved organic carbon supply limits hyporheic denitrification, *Journal of Geophysical Research-Biogeosciences*, *116*.

Zarnetske, J. P., R. Haggerty, S. M. Wondzell, V. A. Bokil, and R. Gonzalez-Pinzon (2012), Coupled transport and reaction kinetics control the nitrate source-sink function of hyporheic zones, *Water Resources Research*, *48*.

Zhou, T., et al. (2018), Riverbed Hydrologic Exchange Dynamics in a Large Regulated River Reach, *Water Resources Research*, *54*(4), 2715-2730.

Zheng, L. Z., M. B. Cardenas, and L. C. Wang (2016), Temperature effects on nitrogen cycling and nitrate removal-production efficiency in bed form-induced hyporheic zones, *Journal of Geophysical Research-Biogeosciences*, *121*(4), 1086-1103.

Zheng, L.Z., M. B. Cardenas (2018), Diel Stream Temperature Effects on nitrogen cycling in hyporheic zones, *Journal of Geophysical Research-Biogeosciences,* 123.

Zeglin, L. H. (2015), Stream microbial diversity in response to environmental changes: review and synthesis of existing research, *Frontiers in Microbiology*, *6*, 15.